




ST. JOHN'S
COLLEGE, ANCHAL

Affiliated to the University of Kerala
Re-accredited with A Grade by NAAC
Recognised for STAR College by DBT, Govt. of India

LET YOUR
LIGHT
SHINE BEFORE
MEN

BSc PHYSICS

 P.B. No.3,
Mar Gregorios Nagar,
Anchal P.O., Kollam,
Kerala - 691 306

Off: 0475-2966973 | Fax: 0475-2275326 
info@stjohns.ac.in | principal@stjohns.ac.in 
www.stjohns.ac.in 



DEPARTMENT OF PHYSICS

A SHORT REVIEW ON GOLD NANOCCLUSERS FOR THE TREATMENT OF PARKINSON'S DISEASE

*PROJECT REPORT SUBMITTED TO UNIVERSITY OF KERALA, IN PARTIAL
FULFILMENT FOR THE REQUIREMENT OF THE AWARD OF THE DEGREE OF
BACHELOR OF SCIENCE IN PHYSICS*

BY

1. SREEHARI S D {Reg .No: 23021138014}
2. DHANANJAYAN M S {Reg .No: 23021138019}
3. PRESTHILA J RAJESH {Reg .No: 23021138020}

Supervisor:

Dr. PRAVEEN S.G.

UNIVERSITY OF KERALA

MAY -2024



DEPARTMENT OF PHYSICS

A SHORT REVIEW ON GOLD NANOCCLUSERS FOR THE TREATMENT OF PARKINSON'S DISEASE

PROJECT REPORT SUBMITTED TO UNIVERSITY OF KERALA, IN PARTIAL
FULFILMENT FOR THE REQUIREMENT OF THE AWARD OF THE DEGREE
OF BACHELOR OF SCIENCE IN PHYSICS

BY

S.NO	NAME	REG.NO	SIGNATURE
1	SREEHARI S D	23021138014	
2	DHANANJAYAN M S	23021138019	
3	PRESTHILA J RAJESH	23021138020	

UNIVERSITY OF KERALA
MAY 2024



DEPARTMENT OF PHYSICS

CERTIFICATE

This is to certify that the project entitled “**A SHORT REVIEW ON GOLD NANOCCLUSERS FOR THE TREATMENT OF PARKINSON’S DISEASE**” is a work done by **SREEHARI S D (Reg. No. 23021138014)** , **DHANANJAYAN M S (Reg. No 23021138019)** and **PRESTHILA J RAJESH (Reg. No. 23021138020)** who are final year students (6th semester) of BSc PHYSICS, ST. JOHN’S COLLEGE, ANCHAL and that no part of this project has been submitted earlier or elsewhere for similar purpose.

Dr. PRAVEEN S.G.

Assistant professor and Research supervisor

Department of Physics

St John’s College, Anchal

Signature



Dr. PRAVEEN S G PhD, AMRSC(UK)
Assistant Professor
Department of Physics
St. John’s College, Anchal
Kollam-691 306, Kerala, India

Dr. BENZON K B

The Head, Department of Physics

St John’s College, Anchal

Signature

Submitted to BSC Physics Degree University Examination May 2024

Signature of Examiner

1:

2:

DECLARATION

We hereby declare that the project entitled “**A SHORT REVIEW ON GOLD NANOCCLUSERS FOR THE TREATMENT OF PARKINSON’S DISEASE**” is a work done by **SREEHARI S D** , **DHANANJAYAN M S** and **PRESTHILA J RAJESH** who are final year students(6th semester) of BSc PHYSICS, ST.JOHNS COLLEGE ,ANCHAL and that no part of this project has been submitted earlier or elsewhere for similar purpose

S.NO	NAME	REG.NO	SIGNATURE
1	SREEHARI S D	23021138014	
2	DHANANJAYAN M S	23021138019	
3	PRESTHILA J RAJESH	23021138020	

PLACE : ANCHAL

DATE :

ACKNOWLEDGEMENT

We express our sincere gratitude with great pleasure towards Dr.Praveen.S.G, Assistant Professor, Department of Physics for his support and guidance for the completion of this project.

We also express our sincere thanks to Dr Benzon K B, Head of the Department of Physics for his support and guidance.

We also extend our thanks to all faculty members, laboratory staffs and my fellow students for valuable assistance to me during the entire period of this project.

Above all I blend my head in humble gratitude to The God who permitted us to finish this project work done timely.

TABLE OF CONTENT

SL NO	CONTENT	PAGE NO:
1	INTRODUCTION	8
2	CHARACTERIZATION OF AuNCs	10
3	AuNCs INHIBIT α -Syn AGGREGATION AND FIBRILLATION	12
4	PREPARATION OF AuNCs	13
5	CELL AND ANIMAL MODELS FOR STUDIES OF PD	13
6	ANIMALS	13
7	EFFECT OF AuNCs TREATMENT IN PD MODEL MICE	14
8	ANIMAL EXPERIMENT	14
9	OPEN FIELD TEST	15
10	AuNCs TREATMENT SIGNIFICANTLY INCREASED TRAVELED DISTANCE AND SPEED IN THE OPEN FIELD TEST OF PD MODEL MICE	16
11	SWIMMING TEST	16
12	AuNCs TREATMENT REVERSED THE DECREASE OF SWIMMING DISTANCE AND SWIMMING DURATION IN THE SWIMMING TEST OF PD MODEL MICE	17

13	ROTARDO TEST	18
14	AuNCs TREATMENT REVERSED THE DECREASED FALL LATENCY AND INCREASED DROP RATE IN THE ROTAROD TEST OF PD MODEL MICE	18
15	HISTOLOGY AND TH IMMUNOHISTOCHEMISTRY	19

16	IMMUNOHISTOCHEMICAL AND WB ANALYSES SHOWED AuNCs TREATMENT REVERSED THE LOSS OF DA NEURONS AND THE DECREASE OF TH EXPRESSION IN PD MODEL MICE	19
17	BLOOD CIRCULATION AND BIODISTRIBUTION STUDIES	20
18	THE BLOOD CIRCULATION BEHAVIOR AND THE TISSUEDISTRIBUTION OF AuNCs IN MICE	21
19	STATISTICS	22
20	TOXICITY STUDIES	22
21	CONCLUSION	24
22	ABBREVIATIONS	25
23	FIGURE DESCRIPTION	26
24	REFERENCE	27



DEPARTMENT OF PHYSICS

A SHORT REVIEW ON GOLD NANOCCLUSERS FOR THE TREATMENT OF PARKINSON'S DISEASE

*PROJECT REPORT SUBMITTED TO UNIVERSITY OF KERALA, IN PARTIAL
FULFILMENT FOR THE REQUIREMENT OF THE AWARD OF THE DEGREE OF
BACHELOR OF SCIENCE IN PHYSICS*

BY

1. SREEHARI S D {Reg .No: 23021138014}
2. DHANANJAYAN M S {Reg .No: 23021138019}
3. PRESTHILA J RAJESH {Reg .No: 23021138020}

Supervisor:

Dr. PRAVEEN S.G.

UNIVERSITY OF KERALA

MAY -2024



DEPARTMENT OF PHYSICS

A SHORT REVIEW ON GOLD NANOCCLUSERS FOR THE TREATMENT OF PARKINSON'S DISEASE

PROJECT REPORT SUBMITTED TO UNIVERSITY OF KERALA, IN PARTIAL
FULFILMENT FOR THE REQUIREMENT OF THE AWARD OF THE DEGREE
OF BACHELOR OF SCIENCE IN PHYSICS

BY

S.NO	NAME	REG.NO	SIGNATURE
1	SREEHARI S D	23021138014	
2	DHANANJAYAN M S	23021138019	
3	PRESTHILA J RAJESH	23021138020	

UNIVERSITY OF KERALA
MAY 2024



DEPARTMENT OF PHYSICS

CERTIFICATE

This is to certify that the project entitled “**A SHORT REVIEW ON GOLD NANOCCLUSERS FOR THE TREATMENT OF PARKINSON’S DISEASE**” is a work done by **SREEHARI S D (Reg. No. 23021138014)** , **DHANANJAYAN M S (Reg. No 23021138019)** and **PRESTHILA J RAJESH (Reg. No. 23021138020)** who are final year students (6th semester) of BSc PHYSICS, ST. JOHN’S COLLEGE, ANCHAL and that no part of this project has been submitted earlier or elsewhere for similar purpose.

Dr. PRAVEEN S.G.

Assistant professor and Research supervisor

Department of Physics

St John’s College, Anchal

Signature

Dr. PRAVEEN S G PhD, AMRSC(UK)
Assistant Professor
Department of Physics
St. John’s College, Anchal
Kollam-691 306, Kerala, India

Dr. BENZON K B

The Head, Department of Physics

St John’s College, Anchal

Signature

Submitted to BSC Physics Degree University Examination May 2024

Signature of Examiner

1:

2:

DECLARATION

We hereby declare that the project entitled “**A SHORT REVIEW ON GOLD NANOCCLUSERS FOR THE TREATMENT OF PARKINSON’S DISEASE**” is a work done by **SREEHARI S D** , **DHANANJAYAN M S** and **PRESTHILA J RAJESH** who are final year students(6th semester) of BSc PHYSICS, ST.JOHNS COLLEGE ,ANCHAL and that no part of this project has been submitted earlier or elsewhere for similar purpose

S.NO	NAME	REG.NO	SIGNATURE
1	SREEHARI S D	23021138014	
2	DHANANJAYAN M S	23021138019	
3	PRESTHILA J RAJESH	23021138020	

PLACE : ANCHAL

DATE :

ACKNOWLEDGEMENT

We express our sincere gratitude with great pleasure towards Dr.Praveen.S.G, Assistant Professor, Department of Physics for his support and guidance for the completion of this project.

We also express our sincere thanks to Dr Benzon K B, Head of the Department of Physics for his support and guidance.

We also extend our thanks to all faculty members, laboratory staffs and my fellow students for valuable assistance to me during the entire period of this project.

Above all I blend my head in humble gratitude to The God who permitted us to finish this project work done timely.

TABLE OF CONTENT

SL NO	CONTENT	PAGE NO:
1	INTRODUCTION	8
2	CHARACTERIZATION OF AuNCs	10
3	AuNCs INHIBIT α -Syn AGGREGATION AND FIBRILLATION	12
4	PREPARATION OF AuNCs	13
5	CELL AND ANIMAL MODELS FOR STUDIES OF PD	13
6	ANIMALS	13
7	EFFECT OF AuNCs TREATMENT IN PD MODEL MICE	14
8	ANIMAL EXPERIMENT	14
9	OPEN FIELD TEST	15
10	AuNCs TREATMENT SIGNIFICANTLY INCREASED TRAVELED DISTANCE AND SPEED IN THE OPEN FIELD TEST OF PD MODEL MICE	16
11	SWIMMING TEST	16
12	AuNCs TREATMENT REVERSED THE DECREASE OF SWIMMING DISTANCE AND SWIMMING DURATION IN THE SWIMMING TEST OF PD MODEL MICE	17

13	ROTARDO TEST	18
14	AuNCs TREATMENT REVERSED THE DECREASED FALL LATENCY AND INCREASED DROP RATE IN THE ROTAROD TEST OF PD MODEL MICE	18
15	HISTOLOGY AND TH IMMUNOHISTOCHEMISTRY	19

16	IMMUNOHISTOCHEMICAL AND WB ANALYSES SHOWED AuNCs TREATMENT REVERSED THE LOSS OF DA NEURONS AND THE DECREASE OF TH EXPRESSION IN PD MODEL MICE	19
17	BLOOD CIRCULATION AND BIODISTRIBUTION STUDIES	20
18	THE BLOOD CIRCULATION BEHAVIOR AND THE TISSUEDISTRIBUTION OF AuNCs IN MICE	21
19	STATISTICS	22
20	TOXICITY STUDIES	22
21	CONCLUSION	24
22	ABBREVIATIONS	25
23	FIGURE DESCRIPTION	26
24	REFERENCE	27

1. INTRODUCTION

NANOCLUSTER are atomically precise crystalline material, which have atleast one dimension between 1 and 10nm and a narrow size distribution. Nanoclusters are composed of upto 100 atoms. But higher ones containing 1000 or more are called nanoparticles. Every atom in the cluster contributes to its size and composition, which affects the size and property of the nanocluster. Properties vary dramatically according to the number of constituent atoms, type of elements and the charge of the cluster. These exhibit variety of unique chemical, physical, magnetic and electronic properties. They have most of the atoms on their surface which leads to high surface to mass ratio. And their high surface area creates more active sites which enhance their catalytic activity.

Nanocluster have wide application in so many field such as drug delivery, renewable energy, electronics, biomedical, environment, textiles, magnetic storage, microelectronics, optical data storage telecommunication, sensors, transducers, biological markers, switches, electroluminescent displays, chemical reactors, catalysts and other area.

GOLD NANOCLUSTERS (AuNCs) are nanoclusters of size less than 2nm consist of several to hundred of gold atoms . AuNCs are protected by templates or ligands. AuNCs have high chemical stability, high catalytic activity, high biocompatibility and strong luminescence. And for the past two decades AuNCs have emerged as a promising agent in the biomedical field. Because of their small size, significant quantization occurs in their conduction band, which leads to its emergent photonic properties. And the properties of gold nanocluster can be utilized for the treatment of Parkinson's diseases.

PARKINSON'S DISEASE (PD) is a common neuro degenerative disease that affect 10 million people world wide. It is characterised by motor symptoms such as tremor, rigidity, slowness of movement and problems with gait, which are often accompanied with fatigue, depression, pain and cognitive impairment. The disorder develops mainly because of the presence of Lewy bodies, which is composed mainly of misfolded and accumulated α -synuclein (α -syn) in neuron and cell death of dopaminergic neurons (DA neurons) in brain

basal ganglia (mainly in substantia nigra (SN) and striatum).

The properties of AuNCs can be utilized for the treatment of Parkinson's disease. On one hand, AuNCs showed excellent capacity to prevent aggregation and fibrillation of α -syn. On the other hand, in cell experiments, they exhibited superb neuroprotection effects against 1-Methyl-4-Phenyl pyridine (MPP⁺) include neurotoxicity. More importantly in animal experiments using mouse PD model induced by 1-Methyl-4-Phenyl-1,2,3,6-tetrahydropyridine (MPTP), we found that AuNCs could effectively reverse the behavioral disorder of sick mice, as determined by open field test, swimming test and rotarod test. And remarkably, immunohistochemical and western blot (WB) showed significant reduction of DA neuron loss in the SN and striatum of the brain, which proved the neuroprotection effect of AuNCs in animal level. These results provides a proof of principle for the promising prospect of AuNCs in new drug discovery against Parkinson's disease (PD).

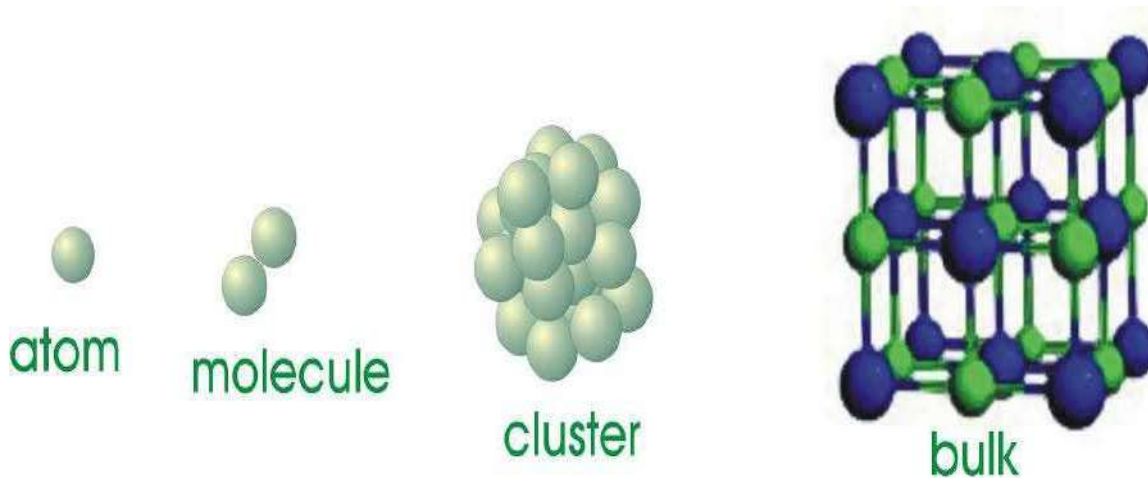


(Fig 1: Showing the transition from single atom to bulk material through nanocluster)

2. CHARACTERIZATION OF AuNCs

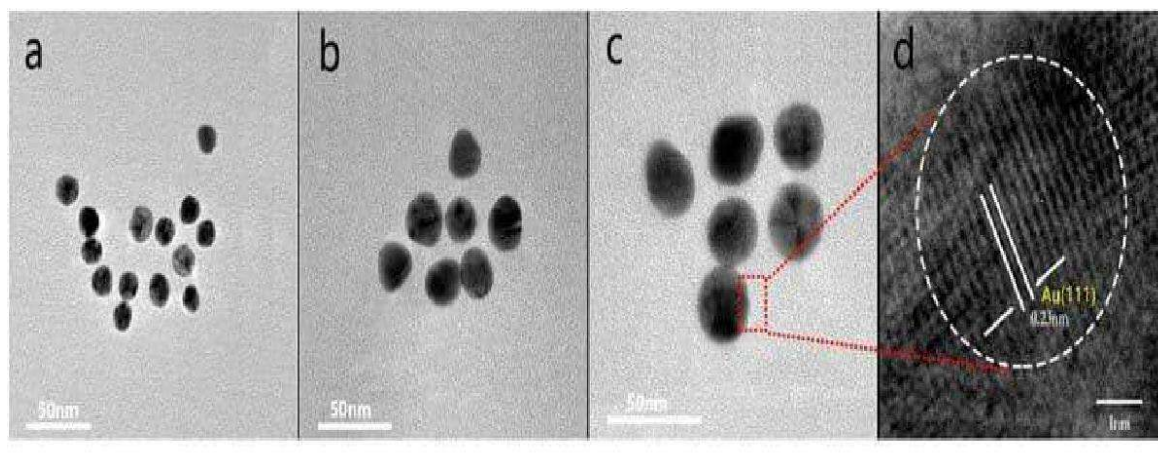


(Fig 2: Transmission electron microscopic (TEM) image of L-NIBC coated AuNCs (L-NIBC-AuNCs))

We used the transmission electron microscopic (TEM) images of L-NIBC coated AuNCs. The statistical data indicated that their average diameter was 1.5 ± 0.5 nm (mean 1SD). The hydrodynamic distribution of L-NIBC-AuNCs measured by the Dynamic light scattering (DLS) was 2.5 ± 10 nm, which was larger than statistical diameter of TEM. The chemical valance of L- NIBC-AuNCs measured by the x-ray photoelectron spectroscopy (XPS) lied between 0 and +1 that accorded with typical characteristics of AuNCs. The typical spectroscopic absorption features of L-NIBC-AuNCs appeared at 580 nm and 680 nm

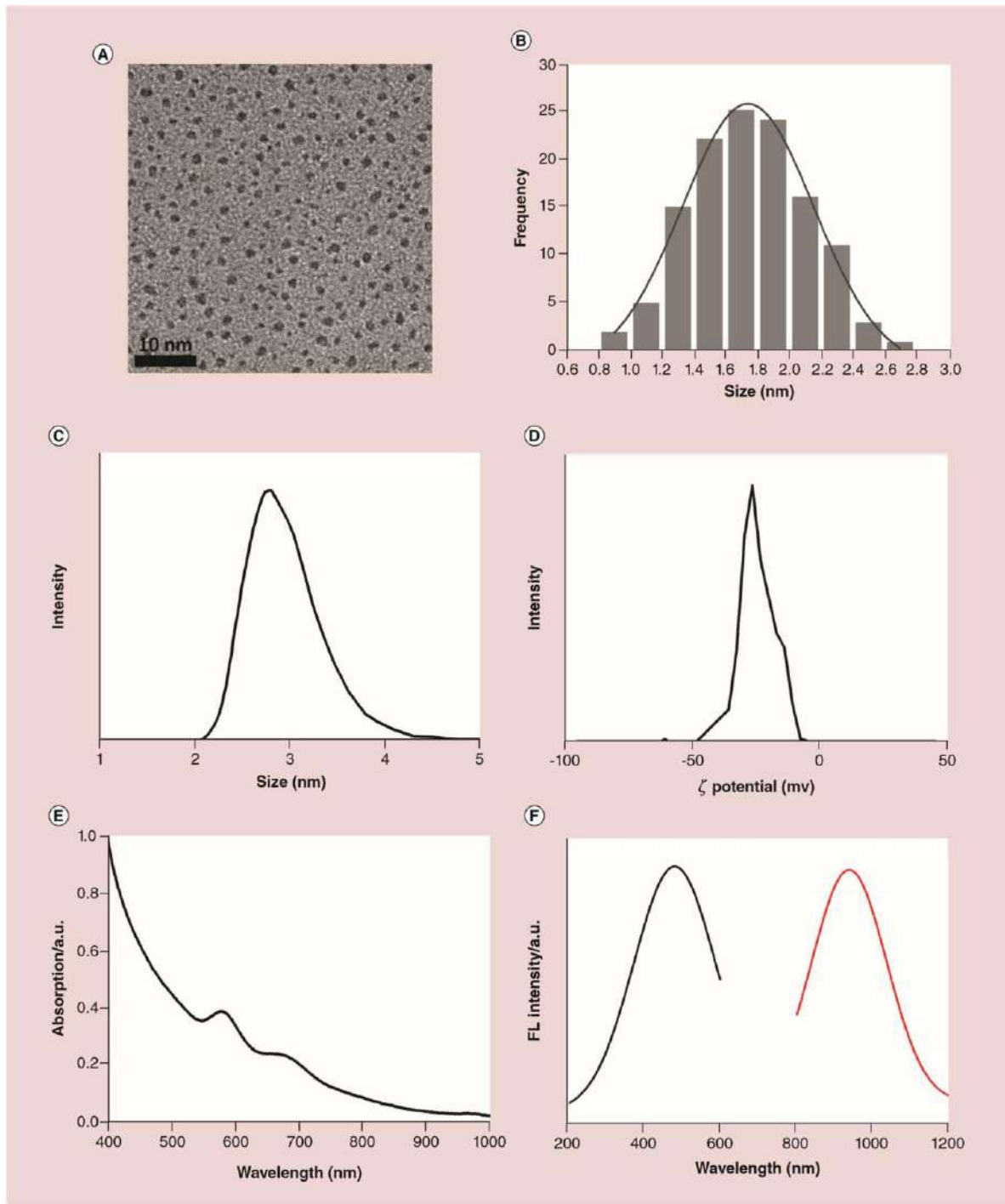


(Fig 3: Characterization of gold nanoclusters. (A) The transmission electron microscopy images of gold nanoclusters (AuNCs). (B) The average particle size distribution of AuNCs based on the transmission electron microscopy images. (C) The hydrodynamic diameter, (D) the ζ -potential, (E) the UV-Vis spectrum and (F) fluorescence spectra of AuNCs.)

3. AuNCs INHIBIT α -Syn AGGREGATION AND FIBRILLATION

α -Syn is a synuclein protein predominantly expressed in presynaptic terminals of neurons, which plays crucial roles in wide variety of neuronal functions Eg: synaptic connectivity, dopamine release, etc .

Unusual aggregation and fibrillation of α -Syn in midbrain DA neurons, which leads to the formation of Lewy bodies is a remarkable pathological hallmark of PD that is highly correlated to dysfunction and death of DA neurons . To inhibit α Syn aggregation and fibrillation is thus an important strategy for PD drug discovery .

To explore the influence of L-NIBC-AuNCs on α -Syn fibrillation dynamics, we need to incubate 2 μ mol L⁻¹ α -Syn in phosphate buffer saline (PBS, 10 mmol L⁻¹, pH = 7.4) at 37 °C with the presence of different concentrations of AuNCs. The kinetics curves were recorded by standard Thioflavin T (ThT) binding assay . The addition of AuNCs greatly postponed the growth phase of fibrillation curves; and with the increase of their concentration, the fluorescent intensity decreased sharply. Through another control experiment we can understand that free L-NIBC did not have evidential influence on α -Syn fibrillation under the same conditions. Since AuNCs do not have SPR effect, which will not induce the quench of ThT fluorescence , the decrease of fluorescence intensity should mainly be attributed to the inhibition against α -Syn fibrillation. Amazingly, when the concentration of AuNCs increased to 10 mg L⁻¹, the fluorescence intensity remained at the background level and the growth phase did not appear even after 168 hours of incubation. This demonstrated a complete inhibition against α -Syn fibrillation, which was further verified by other tests including dynamic light scattering (DLS) analyses , atomic force microscopy (AFM) and TEM studies. In DLS experiments, the average size of α -Syn aggregates increased gradually with the increase of incubation time, which was consistent with the growth curve of α -Syn fibrillation observed in ThT assay.

However, when co-incubated with 10 mg L⁻¹ AuNCs, the average apparent size remained

unchanged from the beginning throughout the incubation period . AFM and TEM studies also

showed that increasing the dosage of AuNCs remarkably reduced the amounts of α -Syn fibrils, and notably, no fibril was found within the entire range of vision when AuNCs concentration reached to 10 mg L⁻¹ even after 168 h of co-incubation.

4. PREPARATION OF AuNCs

Preparation of AuNCs can be done by dissolving ligands and chloroauric acid solution in a mixture of methanol and acetic acid. Then the mixed solution was cooled to approximately 0°C in a cool bath for 30 min in a proper stirring frequency. Then the NaBH₄ was added to the mixed solution keep reacting 2 h under vigorous stirring.

5. CELL AND ANIMAL MODELS FOR STUDIES OF PD

1-methyl-4-phenyl-1,2,3,6-tetrahydropyridine (MPTP) is the prodrug to the neurotoxin 1Methyl- 4-phenylpyridine (MPP⁺), which kills primarily DA neurons in the SN and striatum of the brain [34]. MPP⁺ also interferes with NADH dehydrogenase in the respiratory chain of mitochondrial metabolism, which leads to cell death and induces the accumulation of free radicals. These cause gross depletion of DA neurons, which has severe implications on cortical control of movement abilities, resulting in permanent symptoms of PD.

Therefore, MPP⁺ and MPTP induced to build cell and animal models for studies of PD and relevant drug discovery. We further used MPP⁺ lesioned cell models and MPTP-induced mouse models to study the anti-PD effects of AuNCs.

6. ANIMALS

Male and female Kunming mice of (25–30 g) were used. Probable infection caused to the mice can be avoided by maintaining them in a conventional cages with three animal per cage. Room temperatures needed to be regulated at 25 ± 2°C, and the room should have automatic 12-h

light/dark cycles (lights on 0700 h). All mice were allowed ad libitum access to standard laboratory chow diet and water.

7. EFFECT OF AuNCs TREATMENT IN PD MODEL MICE

MPTP- is induced in the PD model mouse to evaluate the anti-PD effects of AuNCs at an animal level. Then the mice is subjected for OPEN FIELD TEST, SWIMMING TEST AND ROTAROD TEST, respectively and then analysed their behavioural patterns . Compare with the blank controls (Mice in the normal saline solution), mice receiving 7 days continuous MPTP intraperitoneal injection showed significant PD symptoms including tremor, loss of balance, hypotonia, hollow back and hypokinesia, suggest that the mouse PD model had been successfully established.

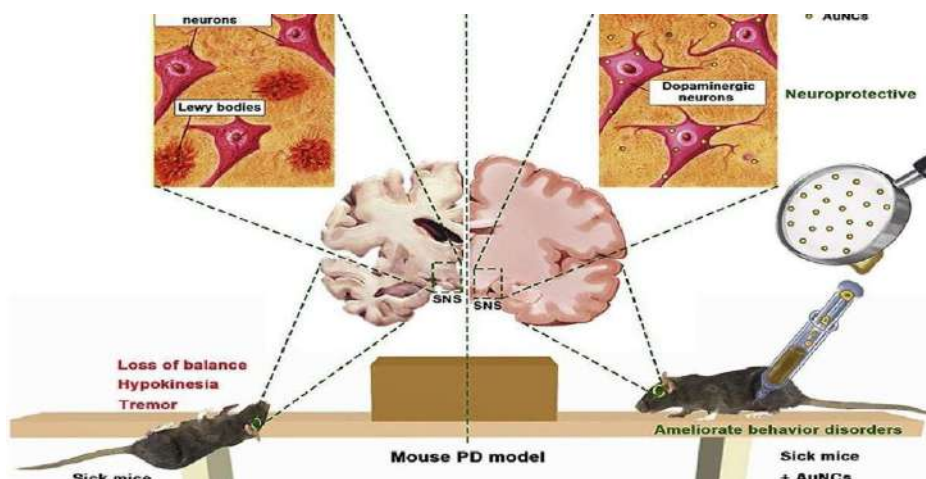


(Fig 4: Effect of AuNCs treatment in PD model mice)

8. ANIMAL EXPERIMENT

A total of 48 C57BL/6 mice were randomly divided into 6 groups (n = 8 mice/group) (blank Controls (normal saline), AuNCs high dose (20 mg kg⁻¹), AuNCs low dose (5 mg kg⁻¹), MPTP model, MPTP + AuNCs (20 mg kg⁻¹), MPTP + AuNCs (5 mg kg⁻¹)). In the model group, MPTP 30 mg kg⁻¹ was given by continuous intraperitoneal injection for 7 days to establish the mouse PD model. The blank controls were administrated with the same amount of normal saline. In the

MPTP + AuNCs groups, the corresponding doses of AuNCs (20 or 5 mg kg⁻¹, 100 µL) were given intraperitoneally for half an hour in advance (once per day), and then MPTP 30 mg kg⁻¹ was given by intraperitoneal injection for 7 days. The AuNCs control groups (20 or 5 mg kg⁻¹, 100 µL) were administrated with different doses of AuNCs and normal saline once per day.

9. OPEN FIELD TEST

Each mouse was placed in the centre of a black square arena (60 × 60 cm², 40 cm high) and allowed to explore the arena for 5 min. Total distance (cm) and average velocity (cm s⁻¹) was recorded by a video camera for 5 min. Locomotor activities were analysed by using LabMaze animal behaviour analysis system.

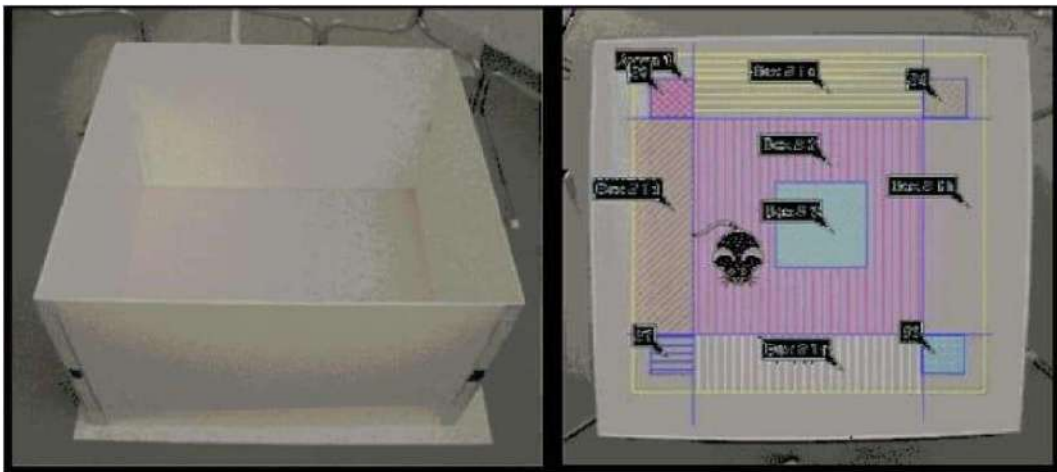


(Fig 5 : An experimental apparatus of open field test)

10. AuNCs TREATMENT SIGNIFICANTLY INCREASED TRAVELED DISTANCE AND SPEED IN THE OPEN FIELD TEST OF PD MODEL MICE

MPTP- is induced in the PD model mouse to evaluate the anti-PD effects of AuNCs at an animal level. Then the mice is subjected for OPEN FIELD TEST, SWIMMING TEST AND ROTAROD TEST, respectively and then analysed their behavioural patterns . Compare with the blank controls (mice intraperitoneally infused with only normal saline), mice receiving 7 days continuous MPTP intraperitoneal injection showed significant PD symptoms including tremor, loss of balance, hypotonia, hollow back and hypokinesia, suggests that the mouse PD model had been successfully established. The PD model mice had significantly reduced locomotor activities measured by both travelled distance ($p < 0.01$) and speed ($p < 0.01$) than those of the blank controls. The AuNCs treatment reversed the decrease of locomotor activity in PD model mice induced by MPTP in a dose-dependent manner. AuNCs high dose (20 mg kg⁻¹) significantly increased travelled distance ($p < 0.01$) and speed ($p < 0.01$) in PD model mice. AuNCs low dose (5 mg kg⁻¹) did not significantly affect locomotor activity of PD model mice. There were no effects of AuNCs treatment for either travelled distance or speed in normal mice ($p > 0.05$).

11. SWIMMING TEST

The swimming tests were made in a circular tank (120 cm diameter), filled with water at 22 °C to a depth of 60 cm. Each mouse was gently placed in the water tub for measuring swimming distance. The behaviour of the mouse in water was recorded by a video camera for 10 min. The swimming distance and swimming duration were analysed by using Lab Maze animal behaviour analysis system.

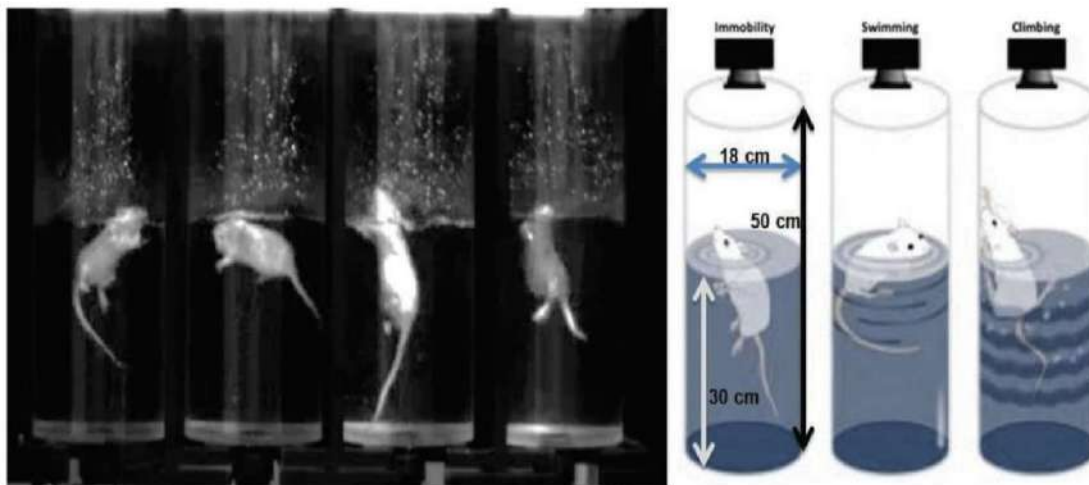


(Fig 6: Swimming test)

12. AuNCs TREATMENT REVERSED THE DECREASE OF SWIMMING DISTANCE AND SWIMMING DURATION IN THE SWIMMING TEST OF PD MODEL MICE

Swimming tests of the laboratory mice were carried out after one week of AuNCs or AuNCs + MPTP treatment. Longest swimming distance and swimming duration reflect the best motor coordination of mice. AuNCs treatment did not evidently affect the swimming distance ($p > 0.05$) and swimming duration ($p > 0.05$) of normal mice compared to the blank controls. The swimming distance of PD model mice without AuNCs treatment was significantly shortened ($p < 0.05$), and their swimming duration was also largely reduced ($p < 0.05$). A high dose AuNCs treatment remarkably reversed the decrease of swimming distance ($p < 0.05$) and swimming duration ($p < 0.05$) in PD model mice, while a low dose AuNCs injection had no evident effect (all $p > 0.005$).

13. ROTAROD TEST

The rotarod test was performed after one week of treatment by using the rotarod equipment. One day prior to the test, the mice were pre-trained on the rotarod for 3 times (one hour interval). The final test (5 sessions) was performed as: the mice were placed on the spindle, rotating at the speed progressively increasing from 5 to 20 rpm in 5 min, and the fall latency was recorded. The average of fall latency of 5 sessions was used for statistical analysis.

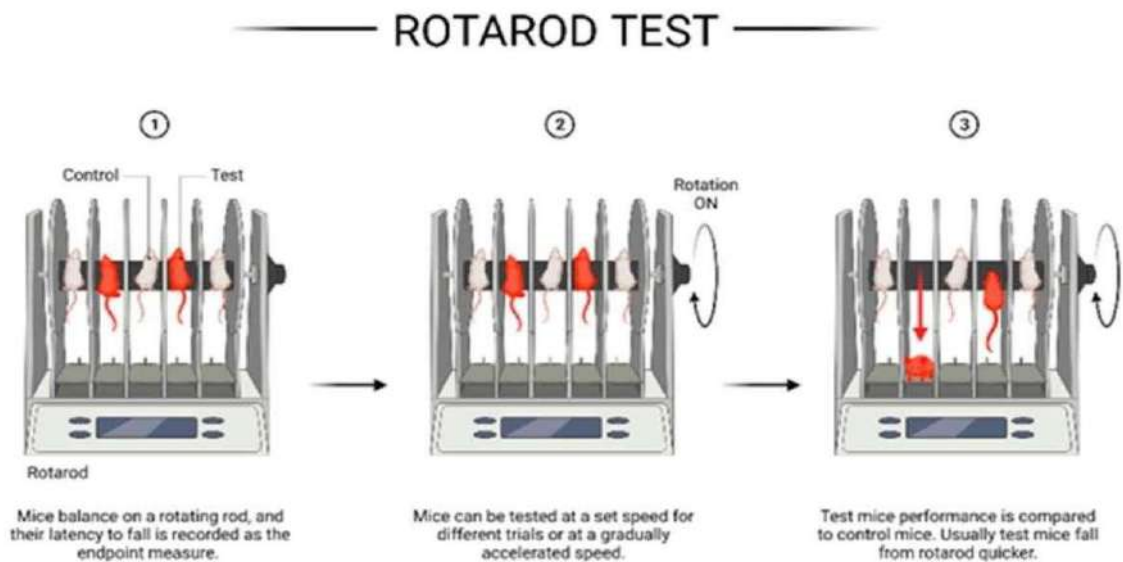


(Fig 7: Rotarod test)

14. AuNCs TREATMENT REVERSED THE DECREASED FALL LATENCY AND INCREASED DROP RATE IN THE ROTAROD TEST OF PD MODEL MICE

The motor coordination of the laboratory mice has also been measured by rotarod test which was performed after 7 days of AuNCs or AuNCs + MPTP treatment. The latency and rate of falling off the rod are a measurement of gross motor skill and coordination. The PD model

mice showed significantly decreased fall latency and increased drop rate compared to normal mice in the blank controls . However, the fall latency of PD model mice was remarkably prolonged by both high dose ($p < 0.01$) and low dose ($p < 0.01$) AuNCs treatment. While, the drop rate of PD model mice was also significantly decreased by both high dose and low dose AuNCs treatment (all $p < 0.001$).

The above findings suggested that AuNCs could markedly reverse the locomotor activity dysfunction and motor coordination dysfunctions of PD model mice in a dose-dependent manner.

15. HISTOLOGY AND TH IMMUNOHISTOCHEMISTRY

Mice were subjected to anesthesia by intraperitoneal injection of 0.5% pentobarbital sodium. The brains were fixed with 4% paraformaldehyde. The paraffin-embedded tissues were section-sliced (3 μM /section). The brain sections were incubated with anti-TH antibody (Abcam) or IBA1 antibody (Abcam) followed by biotinylated secondary antibody. The sections were stained by using diaminobenzidine (DAB) and counter-stained in hematoxylin, followed by imaging.

16. IMMUNOHISTOCHEMICAL AND WB ANALYSES SHOWED AuNCs TREATMENT REVERSED THE LOSS OF DA NEURONS AND THE DECREASE OF TH EXPRESSION IN PD MODEL MICE

A progressive loss of DA neurons in the SN that projects to the striatum is responsible for the major symptoms of PD . The expression of tyrosine hydroxylase (TH) in SN and striatum that catalyze the synthesis of L-DOPA is the rate-limiting step of dopamine biosynthesis . The neurotoxicity of MPTP to DA neurons in the SN and striatum is also available.

Therefore, the next investigated is vested on the fact that whether the improvement in locomotor activity and motor coordination ability of PD model mice induced by AuNCs treatment was due to increased DA neurons and enhanced TH expression. Immunohistochemical analyses revealed that, number of TH-positive neurons (i.e. DA neurons) in the SN markedly reduced in PD model mice compared with those of the blank controls. Obviously, the DA neurons in the SN of PD model of mice showed the cell morphological changes including shrinkage, and protrusions reduction or disappearance. On the other hand, in the striatum of PD model mice, the number of TH-positive cells and the density of nerve fibers were decreased compared to those of the blank controls. Moreover, AuNCs treatment could remarkably inhibit decrease of TH-positive cells and nerve fibers in striatum of PD model mice induced by MPTP. In addition, AuNCs treatment for normal mice (without MPTP) had no significant effect on number of TH-positive cells and densities of nerve fibers in the SN and striatum compared to those of blank controls. From the reference it is known that the TH expression in the striatum of PD model mice were significantly reduced compared to that of the blank controls (55.8% vs blank controls (100%), $p < 0.001$, Fig. 7C). Moreover, the down regulation of TH expression in the striatum of PD model mice induced by MPTP was reversed by both high dose (84.7% vs blank controls, $p < 0.01$ vs MPTP group) and low dose AuNCs treatment (65.6% vs blank controls, $p < 0.01$ vs MPTP group). These results indicated that AuNCs treatment could significantly reverse the loss of DA neurons and the decrease of TH expression in PD model mice induced by MPTP.

17. BLOOD CIRCULATION AND BIODISTRIBUTION STUDIES

Six mice were subjected for injection with a single dose (20 mg kg⁻¹) of the AuNCs. After administration, 50 μ L blood of each mouse was carefully taken from the tail vein with a quantitative capillary at predetermined time points (0, 0.083, 0.167, 0.5, 1, 2, 4, 6, 12 and 24 h). The blood samples were centrifuged at 4 °C at 5000 rpm for 5 min to obtain plasma supernatants. The AuNCs content in the plasma were analyzed by AAS. For evaluating the

tissue distribution, 18 mice were intraperitoneally injected with a single dose of AuNCs (20 mg kg⁻¹). After administration, mice were sacrificed at 2, 6 and 12 post-injection (n = 6). Tissues including heart, liver, spleen, lung, kidney and brain were collected, weighed and stored at -20 °C until analysis. To further confirm whether the AuNCs could penetrate the BBB, 18 mice were intraperitoneally injected with the AuNCs once at a dose of 20 mg kg⁻¹. 2, 6 and 12 h after AuNCs administration, the mice were perfused with 50 mL normal saline under chloral hydrate anesthesia. Then the brains were quickly removed, weighed and stored at -20 °C until analysis. The AuNCs content in the above organs were analyzed by AAS.

18. THE BLOOD CIRCULATION BEHAVIOUR AND THE TISSUE DISTRIBUTION OF AuNCs IN MICE

Circulation half-life of AuNCs in mice (n=6/group) was examined by atomic absorption spectroscopy (AAS). Blood were collected at 0.083, 0.167, 0.5, 1, 2, 4, 6, 12 and 24 hour after a single dose intraperitoneal injection of AuNCs in mice. For biodistribution analysis of AuNCs, 18 mice (n=6/group) were sacrificed after 2, 6 and 12 hour AuNCs post-injection, and heart, liver, spleen, lung, kidney and brain were collected. The tissue distribution of AuNCs in mice was examined by AAS, too. The Au amount in major tissues increased rapidly at second hour, reached their maximums at sixth hour and decreased to about a half at twelveth hour after AuNCs administration. That was consistent with general law of drug absorption . It should be noted that the Au content in the brain of mice were 1.51 ± 0.11 , 5.27 ± 0.49 and $0.50 \pm 0.09 \mu\text{g g}^{-1}$ at 2, 6 and 12 hour after a single dose of AuNCs administration, respectively.

To further confirm that whether the AuNCs could cross the blood brain barrier (BBB), 18 mice (n=6/group) were perfused with normal saline to exclude the blood interference before the brains were collected. It has been found that Au content in these brains of mice were 0.43 ± 0.02 , 0.76 ± 0.05 and $0.37 \pm 0.02 \mu\text{g g}^{-1}$ at 2, 6 and 12 hour after AuNCs administration, respectively . TEM analysis for mice SN slices were further used to prove the presence of AuNCs in the neuron. AuNCs were observed in intracellular of the neurons in the SN slices at 6 h after intraperitoneal injection of AuNCs with a dose of 20

mg kg⁻¹. In contrast, after intraperitoneal injection of same volume of normal saline, none AuNCs could be found in corresponding SN slices. The above results indicated that AuNCs could pass through the BBB. Therefore the neuronal protection effect of AuNCs in mouse PD model should not be a secondary effect of peripheral effects, but rather a direct effect of AuNCs in the central nerve system.

19. STATISTICS

The results of behavioural studies and the protein expression of TH were analysed by using one-way analysis of variance (ANOVA) or Student's t-test. All data were presented as mean \pm SD. Statistical significance was defined as $p < 0.05$.

20. TOXICITY STUDIES

In this case we are concentrating on the toxicity of AuNCs within a certain concentration range, the AuNCs that they synthesized exhibited obvious cytotoxicity. In contrast, the viabilities of the three cells cultured with the synthesized AuNCs, were all nearly 100%, which with no cell-line discrimination and no dose dependence, indicates nocytoxicity of AuNCs within the range of 0– 100 mg l⁻¹. This result may be attributed to ligand and synthesis process. On the other hand, it can be observed that major tissues of treated group mice have not been caused by pathological lesions from AuNCs, which is consistent with another groups findings. These results demonstrate that AuNCs have no toxicity in vivo, which is a precondition for AuNCs to be a potential candidate for the treatment of PD.

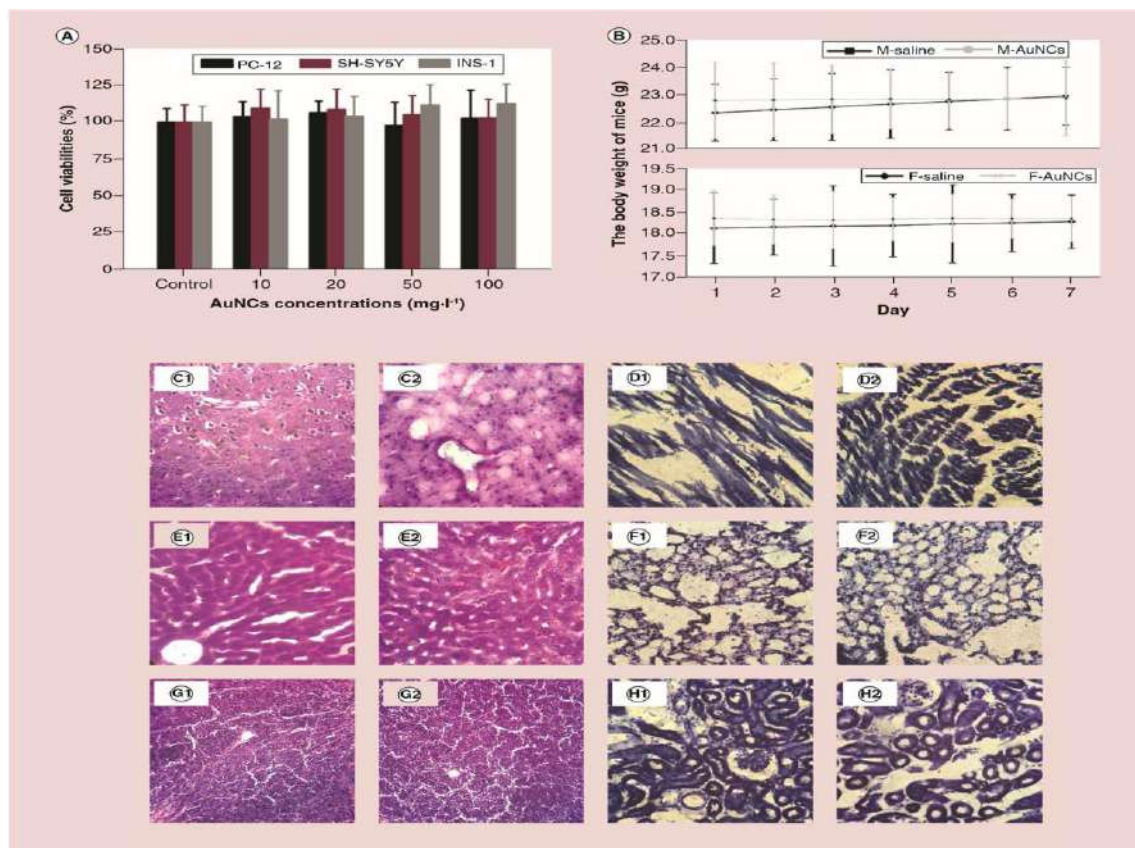


(Fig 8: The toxicity experiment of gold nanoclusters. (A) Cell viability of PC-12, SH-SY5Y and INS-1 treated by normal saline or AuNCs with different concentration for 24 h by CCK-8 assays. (B) The bodyweight of mice treated by normal saline or 100 mg·kg⁻¹ AuNCs for 7 days. Histopathology images (objective × 40) of (C) brain, (D) heart, (E) liver, (F) lung, (G) spleen and (H) kidney using hematoxylin and eosin staining for the mice of (1) AuNCs group; (2) saline group at seventh day. AuNC: Gold nanocluster; F: Female mice; M: Male mice.)

21. CONCLUSION

In conclusion, the results have demonstrated that, AuNCs could significantly inhibit the aggregation and fibrosis of α -Syn in vitro, which may be an important factor for the reduction of Lewy body formation observed in mouse PD model; and on the other hand, AuNCs exhibited superb neuroprotection effects on MPP+ lesioned cell PD model and MPTP induced mouse PD model. Notably, the neurotoxicity of MPTP (MPP+) is associated with the increase of reactive oxygen species and the accumulation of free radicals interfering the respiratory chain of mitochondrial metabolism which is a process irrelevant to α -Syn accumulation. These results revealed that AuNCs could reverse the PD syndromes from different mechanisms that would be very useful in drug discovery against PD. Such direct curative effect of AuNCs also opens a new avenue for medicinal applications of AuNCs.

The journey through Nanocluster and its applications opened us the door for some way to tackle the incurable Parkinson's disease. Our journey starts by analysing the research and studies conducted based on this subject and with the help of our teacher. Through out the process we vested our interest on know more about Parkinson's. And how nanoclusters especially Gold Nanocluster used to tackle it. The various research paper which says about the detailed study conducted over the mice help us to know more about the subject and which helped us to know more about it. The various test conducted over the mice also helped us to know how AuNCs made sound changes in affected mice.

22. ABBREVIATIONS

- AuNCs : Gold Nanocluster
- PD : Parkinson's Disease
- α -syn : Alpha synuclein
- DA neurone : Dopaminergic neurones
- SN :Subtanta nigra
- MPP⁺ : 1-Methyl-4-Phenyl-pyridine
- MPTP : 1-Methyl-4-Phenyl-1,2,3,6-Tetrahydropyridine
- WB : Western Blot
- TEM : Transmission electron microscopic
- XPS : X-ray photoelectron spectroscopy
- PBS : Phosphate Buffer Saline
- ThT : Thioflavin
- AFM : Atomic Force Microscopy
- DLS : Dynamic Light Scattering
- NaBH : Sodium borohydrate
- SPR : Surface Plasmon Resonance
- DAB : Diaminobenzidine
- TH : Tryosine Hydroxylase
- BBB : Blood Brain Barrier
- AAS : Atomic Absorption Spectroscopy
- SD : Standard Deviation
- ANOVA : Analysis of Variance
- CCK : Cholecystokinin

23. FIGURE DESCRIPTION

- Figure 1: Showing the transition from single atom to bulk material through nanocluster
- Figure 2: Transmission electron microscopic (TEM) image of L-NIBC coated AuNCs (L-NIBC-AuNCs)
- Figure 3: Characterization of gold nanoclusters. (A) The transmission electron microscopy images of gold nanoclusters (AuNCs). (B) The average particle size distribution of AuNCs based on the transmission electron microscopy images. (C) The hydrodynamic diameter, (D) the ζ -potential, (E) the UV–Vis spectrum and (F) fluorescence spectra of AuNCs.
- Figure 4: Effect of AuNCs treatment in PD model mice
- Figure 5: An experimental apparatus of open field test
- Figure 6: Swimming test
- Figure 7: Rotarod test
- Figure 8: The toxicity experiment of gold nanoclusters. (A) Cell viability of PC-12, SH-SY5Y and INS-1 treated by normal saline or AuNCs with different concentration for 24 h by CCK-8 assays. (B) The bodyweight of mice treated by normal saline or 100 mg•kg⁻¹ AuNCs for 7 days. Histopathology images (objective \times 40) of (C) brain, (D) heart, (E) liver, (F) lung, (G) spleen and (H) kidney using hematoxylin and eosin staining for the mice of (1) AuNCs group; (2) saline group at seventh day. AuNC: Gold nanocluster; F: Female mice; M: Male mice.

24. REFERENCE

1. Michel G, Alastair C. Parkinson's disease – the story of an eponym. *Nat. Rev. Neurol.* 14, 57–62 (2018).
2. Dauer W, Przedborski S. Parkinson's disease: mechanisms and models. *Neuron* 39, 889– 909 (2003).
3. Samay J. Multi-organ autonomic dysfunction in Parkinson disease. *Parkinsonism Relat. Disord.* 17, 77–83 (2011).
4. Nicolaas IB, Roger LA. The cholinergic system and Parkinson disease. *Behav. Brain Res.* 221, 564–573 (2011).
5. Kathy S, Eleonora M, Jeffrey HK. Etiology of Parkinson's disease: genetics and environment revisited. *PNAS* 99, 13972–13974 (2002).
6. William D, Serge P. Parkinson's disease: mechanisms and models. *Neuron* 39, 889–909 (2003).
7. Bastiaan RB, Nienke M. Nonpharmacological treatments for patients with Parkinson's disease. *Mov. Disord.* 30, 1504–1520 (2015).
8. Richard D, Alexandre P. The blood–brain barrier. *Cold Spring Harb. Perspect. Biol.* 7, a020412 (2015).
9. William AB. Characteristics of compounds that cross the blood–brain barrier. *BMC Neurol.* 9, S3 (2009).
10. Broadwell RD. Transcytosis of macromolecules through the blood–brain barrier: a cell biological perspective and critical appraisal. *Acta Neuropathol.* 79, 117–128 (1989).
11. McCoy RS, Choi S, Collins G, Ackerson BJ, Ackerson CJ. Superatom paramagnetism enables gold nanocluster heating in applied radiofrequency fields. *ACS Nano* 7, 2610– 2616 (2013).
12. An D, Su J, Weber JK, Gao X, Zhou R, Li J. A peptide-coated gold nanocluster exhibits unique behavior in protein activity inhibition. *J. Am. Chem. Soc.* 137, 8412–8418 (2015).
13. Yang S, Jiang Z, Chen Z, Tong L, Lu J, Wang J. Bovine serum albumin-stabilized

- gold nanoclusters as a fluorescent probe for determination of ferrous ion in cerebrospinal fluids via the Fenton reaction. *Microchim. Acta* 182, 1911–1916 (2015).
14. Anjali Devi JS, Salini S, Anulekshmi AH, Praveen GL, Sony G. Fe (III) ion modulated l-DOPA protected gold nanocluster probe for fluorescence turn on sensing of ascorbic acid. *Sensor. Actuat. B Chem.* 246, 943–951 (2017).
 15. Bhamore JR, Murthy ZVP, Kailasa SK. Fluorescence turn-off detection of spermine in biofluids using pepsin mediated synthesis of gold nanoclusters as a probe. *J. Mol. Liq.* 280, 18–24 (2019).
 16. J. A. Santiago, V. Bottero, J. A. Potashkin, Dissecting the molecular mechanisms of neurodegenerative diseases through network biology, *Front. Aging Neurosci.* 9 (2017) 166. <http://doi.org/10.3389/fnagi.2017.00166>.
 17. J. A. Santiago, V. Bottero, J. A. Potashkin, Biological and clinical implications of comorbidities in Parkinson's disease, *Front. Aging Neurosci.* 9 (2017) 394. <http://doi.org/10.3389/fnagi.2017.00394>.
 18. C. H. Adler, Systematic review of levodopa dose equivalency reporting in Parkinson's disease, *Movement Disord.* 20 (15) (2010) 2649-2653. <http://doi.org/10.1002/mds.23429>.
 19. A. B. Singleton, M. Farrer, J. Johnson, A. Singleton, S. Hague, J. Kachergus, M. Hulihan, T. Peuralinna, A. Dutra, R. Nussbaum, S. Lincoln, A. Crawley, M. Hanson, D. Maraganore, C. Adler, M. R. Cookson, M. Muentner, M. Baptista, D. Miller, J. Blacato, J. Hardy, α -Synuclein locus triplication causes Parkinson's disease, *Science* 302 (2003) 841. <http://doi.org/10.1126/science.1090278>.
 20. E. Masliah, E. Rockenstein, I. Veinbergs, M. Mallory, M. Hashimoto, A. Takeda, Y. Sagara, A. Sisk, L. Mucke, Dopaminergic loss and inclusion body formation in alphasynuclein mice: Implications for neurodegenerative disorders, *Science* 287 (2000) 1265-1269. <http://doi.org/10.1126/science.287.5456.1265>.
 21. J. Jankovic, Parkinson's disease: clinical features and diagnosis, *J. Neurol.*

- Neurosurg. Focus. 79 (4) (2008) 368-376. <http://doi.org/10.1136/jnnp.2007.131045>.
22. R. Jin, Quantum sized, thiolate-protected gold nanoclusters, *Nanoscale* 2 (3) (2010) 343-362. <http://doi.org/10.1039/b9nr00160c>.



ST. JOHN'S
COLLEGE, ANCHAL

LET YOUR LIGHT SHINE BEFORE MEN
DEPARTMENT OF PHYSICS

**A SHORT REVIEW OF THE PHYSICAL, CHEMICAL, AND
BIOLOGICAL ASPECT OF PHOTOLUMINESCENT NANOCCLUSERS**

*Project report submitted to University of Kerala, in partial fulfilment for the requirement of
the award of the degree of Bachelor of Science in Physics*

By

AZIF A (23021138001)

JEWEL S LAL (23021138009)

JITHU R (23021138010)

AKHILA R (23021138018)

Supervisor:

Dr PRAVEEN S G

UNIVERSITY OF KERALA

APRIL – 2024



ST. JOHN'S

COLLEGE, ANCHAL

LET YOUR LIGHT SHINE BEFORE MEN

DEPARTMENT OF PHYSICS

A SHORT REVIEW OF THE PHYSICAL, CHEMICAL, AND BIOLOGICAL ASPECT OF PHOTOLUMINESCENT NANOCCLUSERS

Project report submitted to University of Kerala, in partial fulfilment for the requirement of
the award of the degree of Bachelor of Science in Physics

By

NAME	REG NO.	SIGNATURE
AZIF A	23021138001	
JEWEL S LAL	23021138009	
JITHU R	23021138010	
AKHILA R	23021138018	

UNIVERSITY OF KERALA


APRIL – 2024

CERTIFICATE

This is to certify that the project entitled “**A SHORT REVIEW OF THE PHYSICAL, CHEMICAL, AND BIOLOGICAL ASPECT OF PHOTOLUMINESCENT NANOCLUSTERS** ” is a work done by **AZIF A (Reg. No. 23021138001), JEWEL S LAL (Reg. No. 23021138009), JITHU R (Reg. No. 23021138010) & AKHILA R(Reg. No. 23021138018)** who are the students of final year (6th Semester) BSc Physics, St. John’s College, Anchal and that no part of this project has been submitted earlier or elsewhere for similar purpose.

Dr. PRAVEEN S G
Assistant Professor
Department of Physics
St. John’s College Anchal

Signature



Dr. PRAVEEN S G PH.D, AMRSC(UK)
Assistant Professor
Department of Physics
St. John’s College, Anchal
Kollam-691 306, Kerala, India

Dr Benzon K B
The Head,
Department of Physics
St. Johns College, Anchal

Signature

Submitted to BSc Degree University Examinations May 2024

Signature of Examiners:

1:

2:

DECLARATION

We hereby declare that this project work entitled “**A SHORT REVIEW OF THE PHYSICAL, CHEMICAL, AND BIOLOGICAL ASPECT OF PHOTOLUMINESCENT NANOCCLUSERS**” is a project work done by Azif A, Jewel s Lal, Jithu R & Akhila R Final year BSc Physics students (6 *th* Semester), St. John’s College, Anchal and that no part of this project has been submitted earlier or elsewhere for similar purpose.

NAME	REG NO.	SIGNATURE
AZIF A	23021138001	
JEWEL S LAL	23021138009	
JITHU R	23021138010	
AKHILA R	23021138018	

Place: Anchal.

Date:

ACKNOWLEDGEMENT

We express my sincere gratitude with great pleasure towards Dr Praveen S G, Assistant Professor, Department of physics, St. John's College, Anchal for providing the necessary guidance for the completion of this project.

I also express my sincere thanks to the Head of the department for his support and guidance.

I also extend my thanks to all faculty members, laboratory staff and my fellow students for giving valuable assistance to me during the entire period of this project.

Above all I bend my head in humble gratitude to The God who permit us to finish this project work done timely.

TABLES OF CONTENTS

Sl No	CONTENT	PAGE NO
1	Introduction	7
2	Luminescence properties	10
3	Luminescence mechanisms	11
4	Factors affecting luminescence	12
5	Photoluminescence	14
5.1	Importance of photoluminescence	16
5.2	Application of photoluminescence	17
6	Up conversion Luminescence nanomaterials	19
7	Applications of luminescent nanomaterials	20-23
7.1	Bioimaging	20
7.2	Fluorescence Resonance Energy Transfer	21
7.3	Photodynamic therapy	22
7.4	Aggregation Induced Emissions	23
8	Abbreviation	24
9	Figure Description	25
10	Conclusion	26
11	Reference	27

1.INTRODUCTION

Crystal materials of atomic precision, known as nanoclusters, are typically found in the 0–2 nm range. They are frequently seen as kinetically stable intermediates that develop during the creation of more substantial materials like metallic nanocrystals and semiconductors.

Most of the research conducted to study nanoclusters has focused on characterizing their crystal structures and understanding their role in the nucleation and growth mechanisms of larger materials.

Three distinct regimes of materials can be distinguished: bulk, nanoparticle, and nanocluster. Because of surface plasmon resonance, metal nanoparticles exhibit vivid hues, and bulk metals are both good optical reflectors and electrical conductors. Nevertheless, the band structure becomes discontinuous and splits into separate energy levels as the size of metal nanoclusters is further reduced to produce a nanocluster, akin to the energy levels of molecules.

Because of this, nanoclusters are referred to be the bridging link between atoms and nanoparticles and have properties similar to those of a single molecule without exhibiting plasmonic behavior. Molecular nanoparticles is another name for nanoclusters.

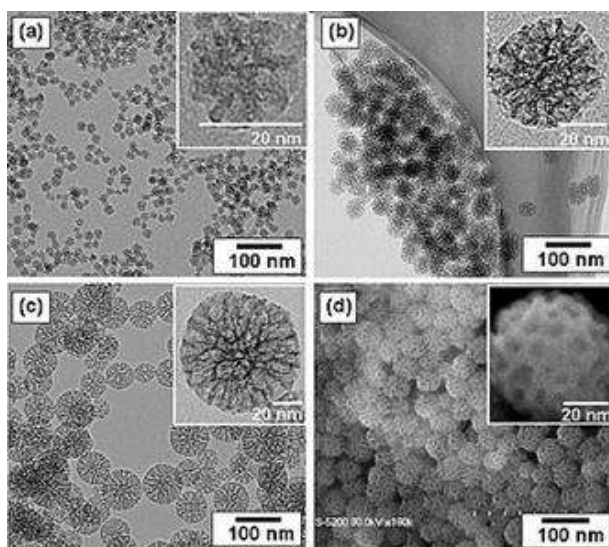


Figure 1: Resolution images of Nanoclusters

Recently, nanoclusters have become a significant class of materials employed in several life sciences disciplines, from clinical treatments to basic biophysical research. Optical bioprobes such as luminescent nanoclusters can greatly enhance the performance of fluorescent proteins that have been genetically modified and other alternative fluorophores.

Their advantages include excellent photostability, tunable and narrow spectra, controllable size, resilience to environmental conditions such as pH and temperature, combined with a large surface for anchoring targeting biomolecules. Some types of nanoparticles provide enhanced detection contrast due to their long emission lifetime and/or luminescence wavelength blue-shift (anti-Stokes) due to energy up conversion. This topical review focuses on four key types of luminescent nanoparticles whose emission is governed by different photo physics. We discuss the origin and characteristics of optical absorption and emission in these nanoparticles and give a brief account of synthesis and surface modification procedures. We also introduce some of their applications with opportunities for further development, which could be appreciated by the physics-trained readership.

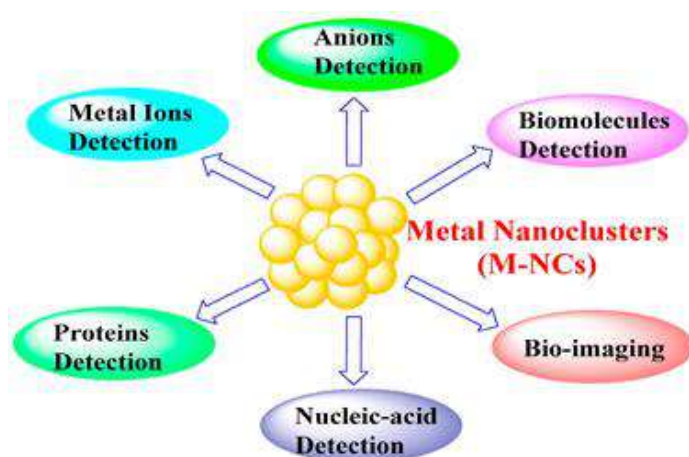


Figure 2: Applications of metal nanoclusters

Luminescent metal nanoclusters that consist of only several, to tens of, metal atoms and which possess sizes comparable to the Fermi wavelength of electrons have recently attracted significant attention.

This new class of luminescent materials not only provides the missing link between atomic and nanoparticle behaviors in metals but also they present abundant novel information for the development of new applicable material systems to meet urgent needs in many areas (such as ultrasensitive sensors for heavy metals, bioimaging, as well as information technology) mainly

because of their attractive characteristics, including ultra-small size, good dispersibility, excellent biocompatibility and photostability.

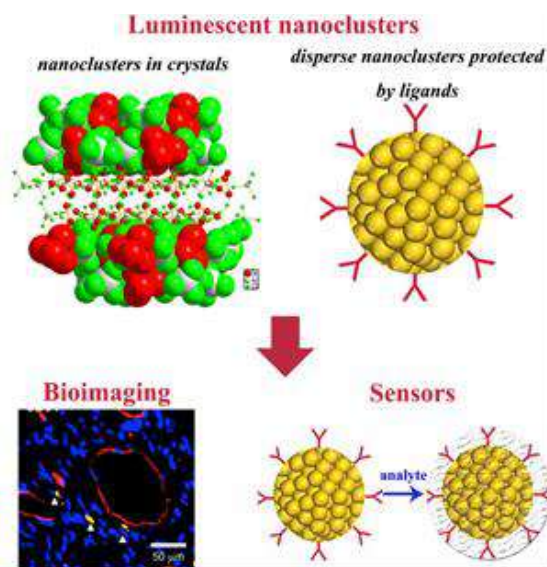


Figure 3: luminescent nanoclusters

Metal nanoclusters (MNCs) are ultrasmall metal-organic aggregates, composed of a metal core less than 2 nm and a protecting shell of metal-organic ligand motifs. The controlled aggregation of metal atoms (in the cluster core) and metal-organic ligand motifs (around the cluster core) renders MNCs with numerous molecule-like properties, among which strong and bright luminescence has attracted extensive basic and applied interests. It is now known that aggregation-induced emission is a feasible mechanism for controlling luminescence of MNCs, which makes it particularly useful in biosensing and bioimaging applications. Although the luminescence fundamentals and design principles largely determine the practicality and effectiveness of MNCs in biosensing and bioimaging applications, a systematic summary of this topic is lacking in the current literature.

In this review, a concise discussion of the latest developments in biosensing and bioimaging applications of luminescent MNCs, highlighting their luminescence mechanisms, biosensing principles, and bioimaging strategies. Specifically, we first introduce the recent advances in the synthetic chemistry of MNCs, and then briefly discuss the luminescence fundamentals of MNCs. Then the design strategy and practicality of luminescent MNCs in biosensing and bioimaging applications are exemplified. We conclude the review with our perspectives on

the further development of MNC-based optical probes in biosensing and bioimaging applications. Our review is expected to provide guidance for the future practice of designing and synthesizing luminescent MNCs for biomedical and other applications.

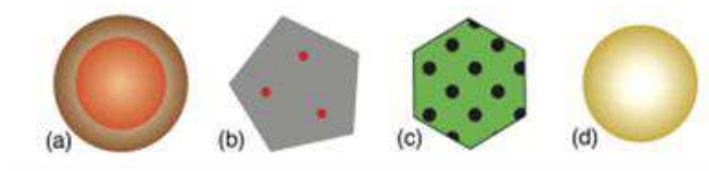


Figure 4: Schematic representation of four key of luminescent nanoparticle. (a) A quantum dot composed of two inorganic materials in a core/shell geometry. (b) A fluorescent nanodiamond containing color centers. (c) An up-conversion nanoparticle composed of an inorganic nanocrystalline host co-doped with two lanthanide (rare-earth) ion species, and (d) a pure gold nanoparticle

2. LUMINESCENCE PROPERTIES

In general, luminescence is the result of radiative decay (i.e. emission of light) by electronically excited molecules following the absorption of energy. The absorbed energy can originate from a variety of sources, which leads to different sub-classifications of luminescence. When the energy is absorbed from electromagnetic radiation in the form of photons (light), the subsequent emission of light is defined as photoluminescence.

The non-thermal production of light by a chemical reaction is termed chemiluminescence, with the special case involving living organisms being referred to as bioluminescence. In some cases, the presence of an electric field can cause electron-hole recombination in a material, producing electroluminescence. If the energy absorbed by the molecules is due to the material being bombarded with high energy ionizing radiation (> 10 eV), the emission of light is referred to as radioluminescence while a beam of high energy electrons imparted upon a material may lead to cathodoluminescence.

The understanding of the luminescence properties of MNCs is not only essential for the rational design of highly luminescent MNCs, but also for their applications in a wide range of fields such as biomedicine, energy conversion, and light emitting devices. Since the early 2000s, the luminescence properties of MNCs have attracted extensive research interest from the cluster research community. However, largely due to the unsatisfactory size Mono dispersity of MNCs in the early stage, it is difficult to establish a reliable structure property relationship at the atomic precision for luminescent MNCs.

3.LUMINESCENCE MECHANISMS

In the early stage, the luminescence of MNCs was mainly attributed to the strong quantum confinement effect in the size range of less than 2 nm. Since there is no bandgap and electron-hole separation or recombination process in plasmonic metal NPs, they hardly emit light. Nevertheless, as the size of metal NPs decreases, their metallic properties gradually disappear, and molecule-like characteristics become dominant.

When the size of MNCs is close to the Fermi wavelength of electrons, the motion of electrons in MNCs is severely restricted, which converts the energy bands of the MNCs into discrete energy levels. This inherently different electronic structure produces completely different physicochemical properties between MNCs and plasmonic metal NPs.

After absorbing light, electrons will be excited, and the excited electrons are prone to radiative relaxation between discrete energy levels, resulting in bright luminescence. The emission of MNCs can span a wide spectrum from UV to the NIR. In the quantum size effect scheme, the excitation and emission wavelengths of MNCs are highly dependent on size. As the size of MNCs decreases, the relaxation energy gap of electrons increases, therefore the emission wavelength of MNCs shifts to the hypochromic end.

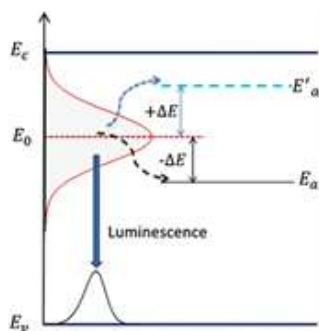


Figure 5: Energy level diagram

With the deepening of the optical research of MNCs, more and more exceptions have been documented against the abovementioned size-dependence of cluster luminescence. For example, Au₂₅ NCs with the same core size but different ligands emit different wavelengths. This readily indicates that in addition to the size of MNCs, the protecting ligand may also contribute to their luminescence. The observations of Wu et al. further support this

conclusion. The authors found that the ligand-to-metal charge transfer (LMCT) through the metal-sulfur bond has a significant impact on the luminescence properties of Au₂₅(SR)₁₈. Keeping the core size of Au NCs unchanged, the luminescence of Au₂₅(SR)₁₈ can be largely promoted by using ligands with electron-rich atoms and groups.

4. FACTORS AFFECTING LUMINESCENCE

Although the exact luminescence origin and mechanism of MNCs are not yet fully understood, some factors that influence the luminescence behavior of MNCs have been identified through the joint efforts of theoretical and experimental chemists. The metal core, surface ligands, and surrounding environment of MNCs are the key factors affecting their luminescence. Tuning the size and composition of the metal core can regulate the emission of MNCs. Since the electronic transition in the M (0) core is an important source of cluster emission, changing the aggregation size and pattern of metal atoms in individual MNCs is an effective method to adjust the luminescence of MNCs. In this scheme, the dependence of emission energy on the number of metal atoms in individual clusters can be estimated through the free electron (Jellium) model.

Metal nanoclusters, with sizes ranging from a few to a few hundred atoms, exhibit fascinating luminescent properties that can be finely tuned by several key factors:

1. **Size and Composition:** The size and composition of metal nanoclusters profoundly influence their luminescence due to quantum confinement effects. As the size decreases, the bandgap increases, leading to blue-shifted emission spectra. Additionally, different metal compositions can result in varying electronic structures and energy levels, affecting luminescent properties.
2. **Surface Ligands:** Ligands attached to the surface of metal nanoclusters play a crucial role in stabilizing the clusters and modulating their luminescence. The choice of ligands can alter the electronic environment around the metal core, affecting the energy levels and charge transfer processes involved in luminescence. Additionally, ligands can protect the nanoclusters from quenching agents, enhancing their stability and luminescent efficiency.
3. **Metal-Metal and Metal-Ligand Interactions:** Interactions between metal atoms within the nanoclusters and between metal atoms and ligands significantly influence their luminescence. Metal-metal interactions can lead to changes in the electronic structure, while metal-ligand interactions can affect the ligand-to-metal charge transfer processes responsible for

luminescence. These interactions can be tailored to optimize luminescent properties for specific applications.

4. Environment: The surrounding environment, including solvent polarity, temperature, and pH, can affect the luminescent behavior of metal nanoclusters. Solvent polarity can influence the energy levels of excited states and the rate of non-radiative decay processes, leading to changes in emission intensity and spectral shape. Temperature variations can also impact luminescence by altering the populations of excited states and the kinetics of energy transfer processes.

5. Aggregation State: The aggregation state of metal nanoclusters, whether they are dispersed or aggregated, can significantly affect their luminescent properties. Aggregation-induced changes in the nanocluster's electronic structure and interparticle interactions can lead to alterations in emission intensity, wavelength, and lifetime. Controlling the aggregation state is essential for maintaining the desired luminescent behavior in practical applications.

6. Excitation Wavelength: The choice of excitation wavelength can influence the luminescent properties of metal nanoclusters by selectively exciting different electronic transitions. Different excitation wavelengths can access distinct energy levels within the nanoclusters, resulting in variations in emission spectra, intensity, and quantum yield. Understanding the excitation wavelength dependence is crucial for optimizing the performance of metal nanoclusters in specific applications.

7. Steric Effects: Steric hindrance from nearby ligands can impact the electronic structure and luminescence efficiency of metal nanoclusters. The spatial arrangement of ligands around the metal core can affect the accessibility of excited states and the efficiency of energy transfer processes. Optimizing the ligand architecture is essential for maximizing luminescent output and minimizing non-radiative decay pathways.

The luminescent properties of metal nanoclusters are intricately governed by a combination of size, composition, surface chemistry, interactions, environmental factors, aggregation state, excitation wavelength, and steric effects. Understanding and controlling these factors are crucial for tailoring the luminescent behavior of metal nanoclusters for a wide range of applications, including sensing, imaging, and optoelectronics.

5. PHOTOLUMINESCENCE

Photoluminescence spectroscopy is a contactless, nondestructive method of probing the electronic structure of materials. Light is directed onto a sample, where it is absorbed and imparts excess energy into the material in a process called photo-excitation. One way this excess energy can be dissipated by the sample is through the emission of light, or luminescence. In the case of photo-excitation, this luminescence is called photoluminescence.

Photo-excitation causes electrons within a material to move into permissible excited states. When these electrons return to their equilibrium states, the excess energy is released and may include the emission of light (a radiative process) or may not (a nonradiative process). The energy of the emitted light (photoluminescence) relates to the difference in energy levels between the two electron states involved in the transition between the excited state and the equilibrium state. The quantity of the emitted light is related to the relative contribution of the radiative process.

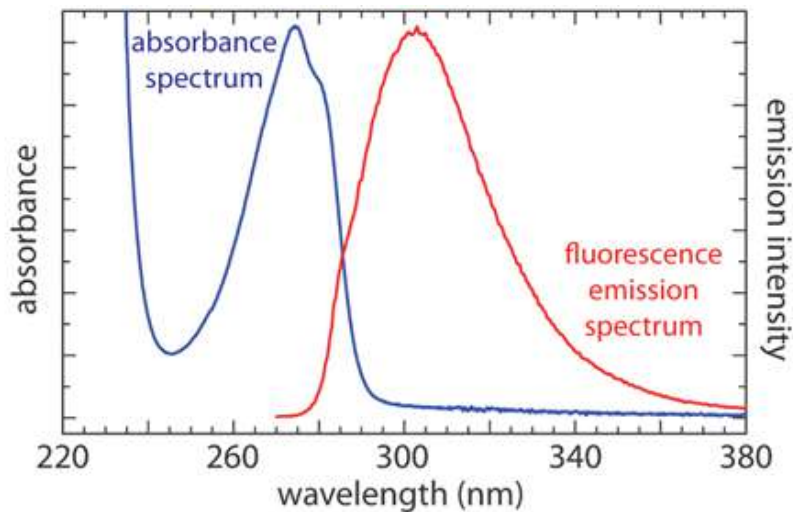


Figure 6: Absorption -Emission spectra

All solids, including semiconductors, have so-called “energy gaps” for the conducting electrons. In order to understand the concept of a *gap* in energy, first consider that some of the

electrons in a solid are not firmly attached to the atoms, as they are for single atoms, but can hop from one atom to another. These loosely attached electrons are bound in the solid by differing amounts and thus have much different energy. Electrons having energies above a certain value are referred to as conduction electrons, while electrons having energies below a certain value are referred to as valence electrons. This is shown in the diagram where they are labeled as conduction and valence bands. The word band is used because the electrons have a multiplicity of energies in either band. Furthermore, there is an energy *gap* between the conduction and valence electron states. Under normal conditions electrons are forbidden to have energies between the valence and conduction bands.

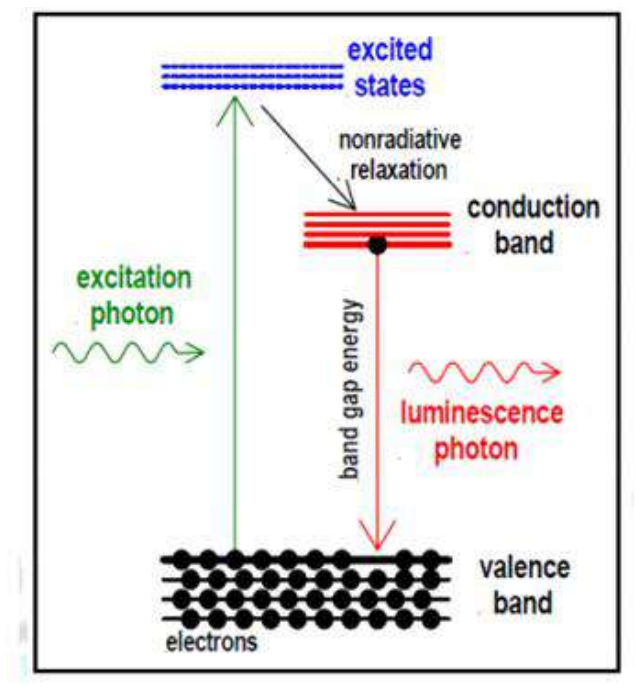


Figure 7: Schematic representation of luminescence photon emission

If a light particle (photon) has energy greater than the band gap energy, then it can be absorbed and thereby raise an electron from the valence band up to the conduction band across the forbidden energy gap. In this process of photo-excitation, the electron generally has excess energy which it loses before coming to rest at the lowest energy in the conduction band. At this point the electron eventually falls back down to the valence band. As it falls down, the energy it loses is converted back into a luminescent photon which is emitted from the material. Thus the energy of the emitted photon is a direct measure of the band gap energy, E_g . The process of photon excitation followed by photon emission is called *photoluminescence*.

5.1 The importance of photoluminescence

1. Probing Quantum Confinement Effects: PL spectroscopy enables the investigation of quantum confinement effects in nanomaterials, wherein the electronic and optical properties are governed by their nanoscale dimensions. By analyzing PL spectra, researchers can directly observe how the bandgap and energy levels of nanomaterials evolve as a function of size, providing critical insights into their quantum mechanical behavior.
2. Characterization of Defects and Surface States: PL serves as a sensitive probe for characterizing defects, impurities, and surface states in nanomaterials. Variations in PL intensity, peak position, and linewidth can reveal information about the density and nature of defects, offering valuable clues for materials engineering and defect mitigation strategies.
3. Studying Carrier Dynamics and Recombination Processes: PL kinetics provide a window into the dynamics of photoexcited carriers in nanomaterials, including their generation, transport, and recombination processes. Time-resolved PL measurements elucidate carrier lifetimes, diffusion lengths, and recombination pathways, shedding light on the underlying physical mechanisms governing charge transport and optoelectronic properties.
4. Understanding Surface and Interface Effects: PL spectroscopy allows researchers to probe the influence of surface chemistry, ligand interactions, and interface engineering on the optical properties of nanomaterials. Surface ligands and functional groups can passivate surface states, suppress non-radiative recombination pathways, and modify PL emission, impacting the overall performance and stability of nanomaterial-based devices.

5. Exploring Novel Phenomena and Quantum Effects: PL studies of nanomaterials provide a platform for exploring novel phenomena and quantum effects that emerge at the nanoscale. Examples include excitonic effects, quantum confinement, quantum dots, and single-photon emission, which have implications for both fundamental science and technological innovation in fields such as quantum information processing and nanophotonics.

6. Guiding Materials Design and Synthesis: Insights gained from PL measurements inform the rational design and synthesis of nanomaterials with tailored optical properties and functionalities. By correlating PL signatures with specific structural and compositional parameters, researchers can optimize synthetic routes, control material morphology, and engineer desired properties for targeted applications.

5.2 Applications of photoluminescence

Photoluminescence, the emission of light following the absorption of photons, holds significant importance across various scientific disciplines and technological applications. Here's a detailed review highlighting its importance:

1. Fundamental Research:

Photoluminescence serves as a powerful tool for fundamental research in physics, chemistry, and materials science. It provides valuable insights into the electronic structure, energy levels, and optical properties of materials, helping scientists understand fundamental principles governing light-matter interactions.

2. Material Characterization:

Photoluminescence spectroscopy is widely used for material characterization, allowing researchers to determine the composition, purity, and defect structure of materials. It provides information about bandgap energies, electronic transitions, and luminescent centers, aiding in the development of new materials for various applications.

3. Semiconductor Physics:

In semiconductor physics, photoluminescence is essential for studying carrier dynamics, recombination processes, and quantum confinement effects in nanostructures. It enables the

evaluation of material quality, doping levels, and interface properties in semiconductors, guiding the design and optimization of semiconductor devices.

4. Optoelectronic Devices:

Photoluminescence plays a crucial role in the development of optoelectronic devices such as light-emitting diodes (LEDs), lasers, and photodetectors. It is used for characterizing device performance, optimizing material properties, and improving device efficiency and reliability.

5. Biomedical Imaging:

In biomedicine, photoluminescence is employed for imaging biological samples with high sensitivity and resolution. Luminescent probes enable non-invasive visualization of cells, tissues, and organs, facilitating medical diagnostics, drug discovery, and biological research.

6. Sensing and Detection:

Photoluminescent sensors are utilized for detecting various analytes such as gases, ions, and biomolecules. They offer rapid, sensitive, and selective detection capabilities, making them valuable tools for environmental monitoring, food safety, and medical diagnostics.

7. Energy Conversion and Lighting:

Photoluminescence plays a crucial role in energy conversion processes, including photovoltaics, photocatalysis, and artificial photosynthesis. It enables the conversion of solar energy into electricity or chemical fuels, contributing to sustainable energy solutions and environmental protection.

8. Nanotechnology and Photonics:

In nanotechnology and photonics, photoluminescence is utilized for fabricating and characterizing nanostructures, quantum dots, and photonic devices. It enables precise control over light emission, propagation, and manipulation at the nanoscale, leading to advancements in nanophotonics, quantum optics, and information technology.

9. Cultural Heritage Preservation:

Photoluminescence techniques are employed in the conservation and authentication of cultural heritage artifacts. They enable the analysis of pigments, dyes, and coatings in artworks, archaeological objects, and historical documents, aiding in their preservation and restoration.

In accordance photoluminescence is a versatile and indispensable tool with widespread applications in scientific research, technology development, and societal challenges. Its importance spans across disciplines, driving innovation and progress in various fields of science and engineering.

6.UPCONVERSION LUMINESCENCE NANOMATERIALS

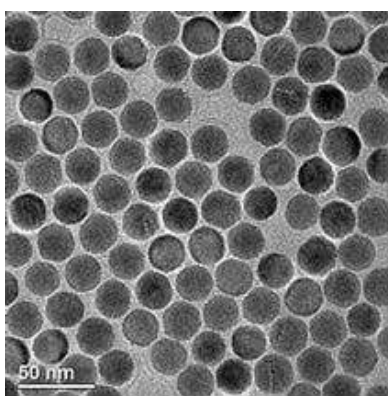


Figure 8: Image of typical up conversion nanocrystals

Up conversion nanomaterials can emit high-energy lights when excited with two or more low-energy photons. They can produce ultraviolet (UV)-visible or near-infrared (NIR) light upon excitation with NIR light, depending on size or dopants, owing to their unique properties, such as good optical stability, narrow emission band, large anti-Stokes spectral shift, high levels of light penetration in biological tissues, long luminescence lifetime, and high signal-to-noise ratio.

Mechanism of up conversion luminescence nanomaterials have potential applications in bioimaging, detection, photodynamic therapy, and therapeutics.

Up conversion nanocrystals converting near-infrared light into high-energy UV emissions may provide many exciting opportunities for drug release, photocatalysis, photodynamic therapy, and solid-state lasing. However, a key challenge is their low conversion efficiency.

- Key features:
 - Good optical stability
 - Narrow emission bands
 - Large anti-Stokes spectral shift
 - High penetration in biological tissues
 - Long luminescence lifetime.

7. APPLICATIONS OF LUMINESCENT NANOMATERIALS:

7.1 Bioimaging.

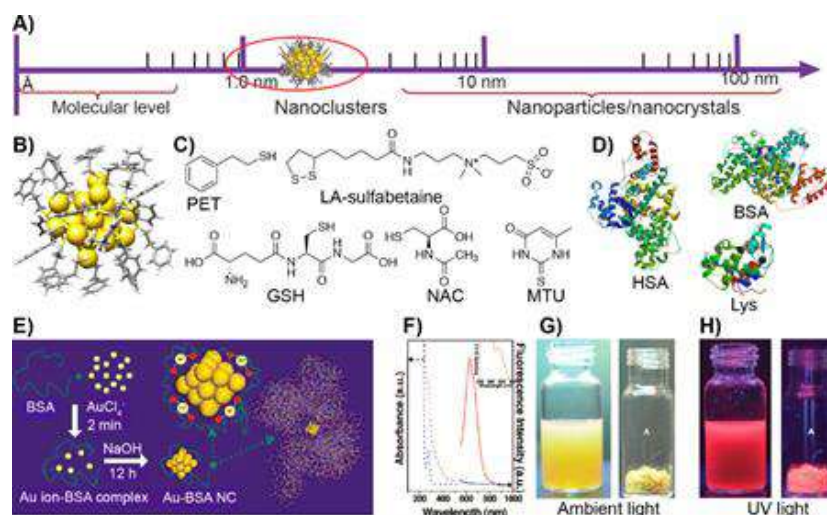


Figure 9: Bioimaging using gold nanoclusters

An effective way to study biological components in living organisms or to understand biological processes occurring *in vivo* is to make them visible. Optical imaging technique is a useful tool to achieve this goal. By using FL imaging agents, visualization of various biological components and real-time monitoring of dynamic biological processes can be achieved. Compared with other traditional imaging methods, FL imaging has the advantages of non-invasiveness, high signal-to-noise ratio, and excellent temporal and spatial resolution.

So far, several FL imaging materials have been developed, and these materials can be mainly divided into two categories: organic molecules and inorganic nanomaterials. Generally, most

organic dyes suffer from photobleaching or phototoxicity. In recent years, some luminescent inorganic nanomaterials, such as quantum dots, rare-earth doped NPs, and carbon materials, have also found potential applications in bioimaging..

Luminescent MNCs can bypass some inherent problems of organic dyes and conventional inorganic nanoparticles. Luminescent MNCs possess a series of attractive features such as easy synthesis and conjugation, excellent photostability, good biocompatibility, efficient renal clearance, large Stoke shift, long emission lifetime, and tunable emission wavelength, which make them a promising class imaging agents for biomedical applications.

7.2 Fluorescence Resonance Energy Transfer (FRET).

Fluorescence Resonance Energy Transfer (FRET) is a physical phenomenon first described over 50 years ago, that is being used more and more in biomedical research and drug discovery today. FRET relies on the distance-dependent transfer of energy from a donor molecule to an acceptor molecule. Due to its sensitivity to distance, FRET has been used to investigate molecular interactions.

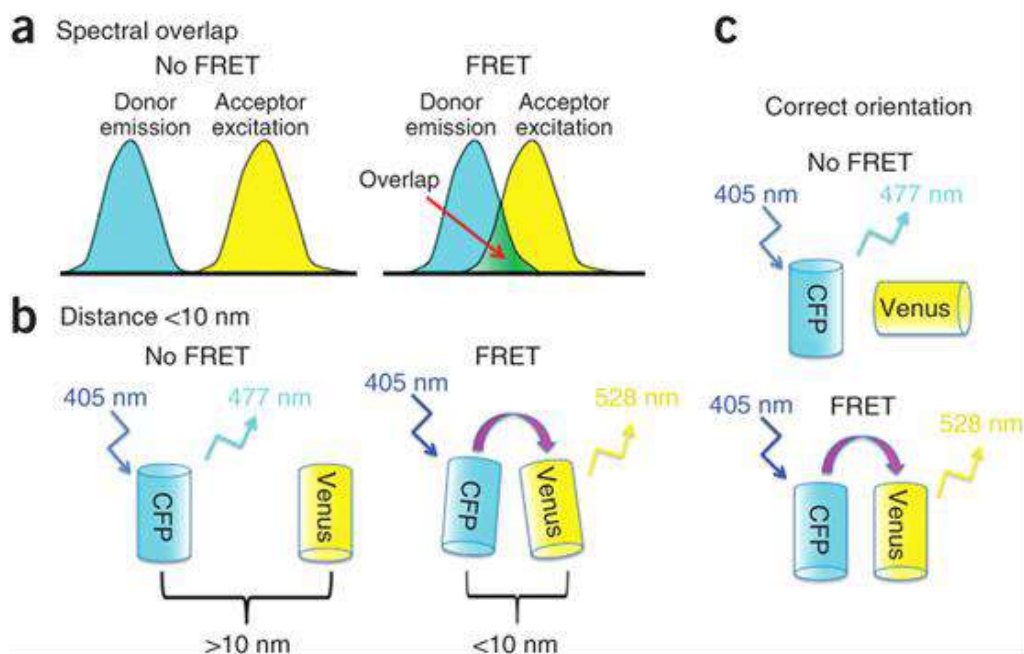


Figure 10: Diagrams showing different steps in FRET

FRET is the radiation less transmission of energy from a donor molecule to an acceptor molecule. The donor molecule is the dye or chromophore that initially absorbs the energy and the acceptor is the chromophore to which the energy is subsequently transferred. This resonance interaction occurs over greater than interatomic distances, without conversion to thermal energy, and without any molecular collision.

The transfer of energy leads to a reduction in the donor's fluorescence intensity and excited state lifetime, and an increase in the acceptor's emission intensity. A pair of molecules that interact in such a manner that FRET occurs is often referred to as a donor/acceptor pair.

7.3 Photodynamic Therapy (PDT).

Photodynamic therapy (PDT) is a two-stage treatment that implies the use of light energy, oxygen, and light-activated compounds (photosensitizers) to elicit cancerous and precancerous cell death after light activation (phototoxicity). Compared to conventional therapeutic modalities, PDT presents greater selectivity against tumor cells, due to the use of photosensitizers that are preferably localized in tumor lesions, and the precise light irradiation of these lesions. PDT studies have shown promise in directing the harmful effects of ROS toward cancer cells by utilizing the body's endogenous oxygen in combination with a photosensitizer (PS) and light at a specific wavelength.

Photodynamic therapy (PDT) is a minimally invasive method that has captured significant attention as an emerging tool for the treatment of cancer. Some studies have also reported its potential to offer several advantages when applied in combination with conventional therapies, such as chemotherapy and radiation.

The dynamics of PDT are mainly dependent on the electronic interactions between an excited photosensitizer compound (PS) and molecular oxygen. These further lead to energy transfer reactions, culminating in the generation of ROS, primarily singlet oxygen (1O_2). PDT is gaining considerable recognition for its selectivity, relative ease of therapeutic application, high tolerability by patients, and efficacy in treating certain cancers, including inoperable tumors. A significant advantage of this therapeutic approach is its ability to focus disruptive oxygenated reactions on a specific target site within the body, like tumors, thereby minimizing damage to the surrounding healthy tissue.

Applications of PDT include:

Cancer Treatment: PDT is used in the treatment of various types of cancer, including skin cancer (e.g., basal cell carcinoma, squamous cell carcinoma), lung cancer, esophageal cancer, and certain types of head and neck cancers. It can be employed as a standalone therapy or in combination with other treatment modalities, such as surgery, chemotherapy, or radiation therapy.

Dermatological Conditions: PDT is effective in treating various dermatological conditions, including actinic keratosis (pre-cancerous skin lesions), acne vulgaris, psoriasis, and certain types of skin infections.

Ophthalmology: PDT is used in ophthalmology to treat certain retinal diseases, such as age-related macular degeneration (AMD) and ocular tumors.

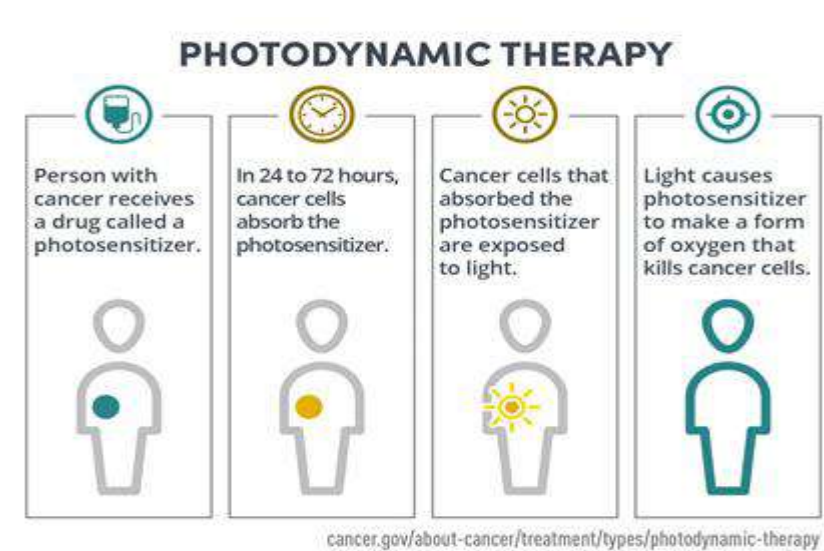


Figure 11: Photodynamic therapy

7.4 Aggregation-Induced Emissions (AIE).

The emergence of the aggregation-induced emission (AIE) concept significantly changes the cognition of the scientific community toward classic photophysical phenomena. More importantly, the AIE phenomenon has brought huge opportunities for the analysis of bioactive species, the monitoring of complicated biological processes, and the elucidation of key physiological and pathological behaviors.

As a class of promising luminescent materials, AIE luminogens (AIEgens) are weakly or non-emissive in the form of isolated molecular species but emit particularly strong fluorescence in the aggregated and solid states. Motivated by the prominent advantages such as high brightness, large Stokes shift, excellent photostability, and good biocompatibility, AIE gen-based bioprobes have been widely explored in the field of biomedicine.

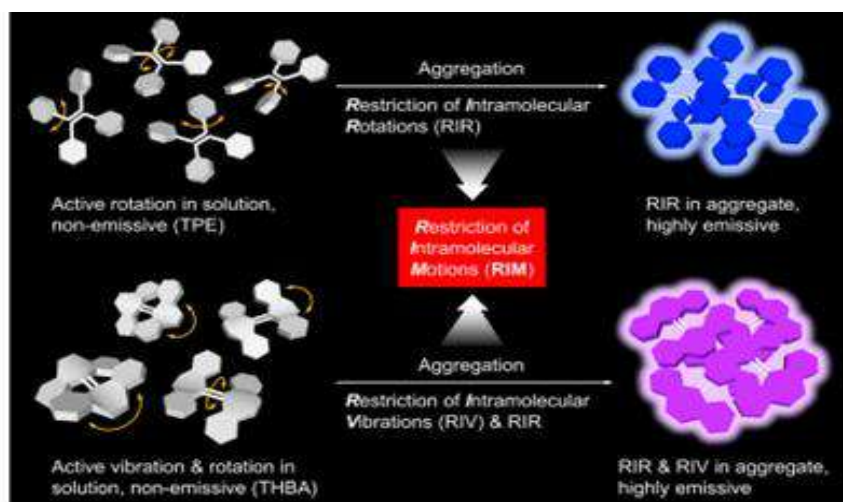


Figure 12: Schematic illustration showing the mechanisms of the AIE phenomenon

8. ABBREVIATIONS

NCs: Nanoclusters

MNCs: Metal Nanoclusters

UV: Ultraviolet

NIR: Near Infra-Red

FRET: Florescence Resonance Energy Transfer

PDT: Photodynamic Therapy

AIE: Aggregated Induced Emissions

9. FIGURE DESCRIPTION

Figure 1: Resolution image of nanoclusters

Figure 2: Applications of metal nanoclusters

Figure 3: Luminescent nanoclusters

Figure 4: Schematic representation of four key of luminescent nanoparticle. (a) A quantum dot composed of two inorganic materials in a core/shell geometry. (b) A fluorescent nanodiamond containing color centers. (c) An up-conversion nanoparticle composed of an inorganic nanocrystalline host co-doped with two lanthanide (rare-earth) ion species, and (d) a pure gold nanoparticle

Figure 5: Energy level diagram

Figure 6: Absorption-Emission Spectrum

Figure 7: Schematic representation of luminescence photon emission

Figure 8: Typical image of up conversion nanocrystals

Figure 9: Bioimaging using gold nanoclusters

Figure 10: Diagram showing different steps in FRET

Figure 11: Photodynamic therapy

Figure 12: Systematic illustration showing the mechanisms of the Aggression Induced Emission

10. CONCLUSION

Investigating luminescence in nanoclusters has been a fascinating voyage through the complex realm of photonics and nanomaterials. We have explored the basic ideas, synthesis strategies, characterization approaches, and many uses of luminous nanoclusters in this study. Let's take a moment to consider the most important lessons learned and the exciting opportunities that this dynamic area holds as we end. For years, scientists have been fascinated by the phenomena known as luminescence, which is the production of light without the usage of heat. This interest has now expanded to nanoclusters, which are minuscule groups of atoms or molecules with distinctive optical characteristics.

Because of quantum confinement phenomena, which result in distinct energy levels when electrons are confined in a limited area, nanoclusters glow. The electronic structure is changed by this confinement, which has an impact on light emission and absorption. As a result, depending on their size and makeup, nanoclusters can generate light with different colors. Quantum dots, which are semiconductor nanoclusters that have attracted attention due to their tunable luminescence throughout the visible spectrum, are one well-known example. Researchers can carefully regulate the optical properties of these nanoclusters by varying their size and composition, which makes them attractive options for use in biological imaging, lighting, and displays.

Luminescent nanoclusters represent a fascinating intersection of nanoscience and photonics, offering unprecedented control over light emission on the nanoscale. Continued research in this field promises to unlock new insights into fundamental light-matter interactions and drive innovations in various technological domains.

Furthermore, the distinctive luminescence characteristics of noble metal nanoclusters—such as those of gold and silver—are ascribed to plasmons, which are collective oscillations of electrons. These plasmonic nanoclusters are helpful for sensing and catalysis because of their high efficiency light emission and robust interactions with surrounding molecules. Composed of molecules based on carbon, organic nanoclusters have become a flexible luminous material with applications in bioimaging and optoelectronics. These nanoclusters frequently show signs of aggregation-induced emission, which allows for sensitive detection in biological systems by increasing their luminosity as they assemble.

11.REFERENCE

- 1 . Lakowicz J R 2006 Principles of Fluorescence Spectroscopy 3rd edn (Berlin: Springer)
2. Moerner W E 2007 New directions in single-molecule imaging and analysis Proc. Natl Acad. Sci. USA
3. L. Zhang, E. Wang, Nano Today 2014, 9.
4. H. Qian, M. Zhu, Z. Wu, R. Jin, Acc. Chem. Res. 2012, 45, 1470.
5. S. E. Crawford, M. J. Hartmann, J. E. Millstone, Acc. Chem. Res. 2019, 52, 695.
6. M. S. Bootharaju, S. Lee, G. Deng, S. Malola, W. Baek, H. Hakkinen, N. Zheng, T. Hyeon, Angew. Chem., Int. Ed. 2021, 60, 9038
7. Benov, L. Photodynamic Therapy: Current Status and Future Directions. Med. Princ. Pract. 2015, 24.
8. Chen, Y.; Zhang, L.; Li, F.; Sheng, J.; Xu, C.; Li, D.; Yu, H.; Liu, W. Combination of Chemotherapy and Photodynamic Therapy with Oxygen Self-Supply in the Form of Mutual Assistance for Cancer Therapy. Int. J. Nanomed. 2021, 16, 3679.
9. Benov, L. Photodynamic Therapy: Current Status and Future Directions. Med. Princ. Pract. 2015, 24,
10. Chen, Y.; Zhang, L.; Li, F.; Sheng, J.; Xu, C.; Li, D.; Yu, H.; Liu, W. Combination of Chemotherapy and Photodynamic Therapy with Oxygen Self-Supply in the Form of Mutual Assistance for Cancer Therapy. Int. J. Nanomed. 2021, 16, 3679.
11. El-Hussein, A.; Manoto, S.L.; Ombinda-Lemboumba, S.; Alrowaili, Z.A.; Mthunzi-Kufa, P. A Review of Chemotherapy and Photodynamic Therapy for Lung Cancer Treatment. Anticancer Agents Med. Chem. 2021, 22.
12. Su, C.-H.; Nowakowska, M.; Kim, T.E.; Chang, J.-E. Recent Studies in Photodynamic Therapy for Cancer Treatment: From Basic Research to Clinical Trials. Pharmaceutics 2023, 15, 2257.

13. Schulman, S.G. (1985) Luminescence Spectroscopy: An Overview, in Molecular Luminescence Spectroscopy - Methods and Applications: Part 1, (ed Schulman, S. G.), John Wiley & Sons, New York, pp.
14. Vogler, A. and Kunkely, H. (2001) Luminescence in Metal Complexes: Diversity of excited states, in Transition Metal and Rare Earth Compounds, (ed Yersin, H.), Springer, Berlin .
15. Ronda, C. (ed) (2008) Luminescence: From Theory to Applications, Wiley, Weinheim.
16. Birks, J.B. (1970) Photophysics of Aromatic Molecules, Wiley-Interscience, London.
17. Valeur, B. and Brochon, J.-C. (ed) (2001) New trends in fluorescence spectroscopy : applications to chemical and life science, Springer, New York.
18. Hong-Tao Sun and Yoshio Sakka College of Chemistry, Chemical Engineering and Materials Science, Soochow University, Suzhou 215123, People's Republic of China 2 Advanced Ceramics Group, Materials Processing Unit, National Institute for Materials Science (NIMS), 1-2-1 Sengen, Tsukuba-city, Ibaraki 305-0047, Japan
19. Yan Xiao^{1,2} Zhennan Wu¹ Qiaofeng Yao¹ Jianping Xie^{1,3} ¹ Department of Chemical and Biomolecular Engineering, National University of Singapore, 4 Engineering Drive 4, Singapore, Singapore ² College of Chemistry and Chemical Engineering, Hubei University, Wuhan, Hubei, China ³ Joint School of National University of Singapore and Tianjin University, International Campus of Tianjin University Binhai New City, Fuzhou, China
20. Pablo Llano Suáreza , Marta García-Cortésa , María Teresa Fernández-Argüellesa,b,* , Jorge Ruiz Encinara , Marta Valledorc , Francisco Javier Ferreroc , Juan Carlos Campoc , José Manuel Costa-Fernándeza,* a Department of Physical and Analytical Chemistry. University of Oviedo, Avda. Julián Clavería 8, Oviedo 33006, Spain. b Life Sciences Department, International Iberian Nanotechnology Laboratory (INL), Av. Mestre José Veiga, 4715-330 Braga, Portuga
21. Shuqi Wu¹ , Yang Li¹ , Weihang Ding¹ , Letong Xu¹ , Yuan Ma² , Lianbing Zhang¹ * * Lianbing Zhang, lbzhang@nwpu.edu.cn ¹ School of Life Sciences, Key Laboratory of Space Bioscience and Biotechnology, Northwestern Polytechnical University, Xi'an 710072, People's Republic of China ² School of Materials Science and Engineering, Northwestern Polytechnical University, Xi'an 710072, People's Republic of China.



ST. JOHN'S
COLLEGE, ANCHAL

LET YOUR LIGHT SHINE BEFORE MEN
DEPARTMENT OF PHYSICS

**A SHORT REVIEW OF THE PHYSICAL, CHEMICAL, AND
BIOLOGICAL ASPECT OF PHOTOLUMINESCENT NANOCCLUSERS**

*Project report submitted to University of Kerala, in partial fulfilment for the requirement of
the award of the degree of Bachelor of Science in Physics*

By

AZIF A (23021138001)

JEWEL S LAL (23021138009)

JITHU R (23021138010)

AKHILA R (23021138018)

Supervisor:

Dr PRAVEEN S G

UNIVERSITY OF KERALA

APRIL – 2024



ST. JOHN'S

COLLEGE, ANCHAL

LET YOUR LIGHT SHINE BEFORE MEN
DEPARTMENT OF PHYSICS

A SHORT REVIEW OF THE PHYSICAL, CHEMICAL, AND BIOLOGICAL ASPECT OF PHOTOLUMINESCENT NANOCCLUSERS

Project report submitted to University of Kerala, in partial fulfilment for the requirement of
the award of the degree of Bachelor of Science in Physics

By

NAME	REG NO.	SIGNATURE
AZIF A	23021138001	
JEWEL S LAL	23021138009	
JITHU R	23021138010	
AKHILA R	23021138018	

UNIVERSITY OF KERALA


APRIL – 2024

CERTIFICATE

This is to certify that the project entitled “**A SHORT REVIEW OF THE PHYSICAL, CHEMICAL, AND BIOLOGICAL ASPECT OF PHOTOLUMINESCENT NANOCCLUSERS** ” is a work done by **AZIF A (Reg. No. 23021138001), JEWEL S LAL (Reg. No. 23021138009), JITHU R (Reg. No. 23021138010) & AKHILA R(Reg. No. 23021138018)** who are the students of final year (6th Semester) BSc Physics, St. John’s College, Anchal and that no part of this project has been submitted earlier or elsewhere for similar purpose.

Dr. PRAVEEN S G
Assistant Professor
Department of Physics
St. John’s College Anchal

Signature



Dr. PRAVEEN S G PH.D, AMRSC(UK)
Assistant Professor
Department of Physics
St. John’s College, Anchal
Kollam-691 306, Kerala, India

Dr Benzon K B
The Head,
Department of Physics
St. Johns College, Anchal

Signature

Submitted to BSc Degree University Examinations May 2024

Signature of Examiners:

1:

2:

DECLARATION

We hereby declare that this project work entitled “**A SHORT REVIEW OF THE PHYSICAL, CHEMICAL, AND BIOLOGICAL ASPECT OF PHOTOLUMINESCENT NANOCCLUSERS**” is a project work done by Azif A, Jewel s Lal, Jithu R & Akhila R Final year BSc Physics students (6 *th* Semester), St. John’s College, Anchal and that no part of this project has been submitted earlier or elsewhere for similar purpose.

NAME	REG NO.	SIGNATURE
AZIF A	23021138001	
JEWEL S LAL	23021138009	
JITHU R	23021138010	
AKHILA R	23021138018	

Place: Anchal.

Date:

ACKNOWLEDGEMENT

We express my sincere gratitude with great pleasure towards Dr Praveen S G, Assistant Professor, Department of physics, St. John's College, Anchal for providing the necessary guidance for the completion of this project.

I also express my sincere thanks to the Head of the department for his support and guidance.

I also extend my thanks to all faculty members, laboratory staff and my fellow students for giving valuable assistance to me during the entire period of this project.

Above all I bend my head in humble gratitude to The God who permit us to finish this project work done timely.

TABLES OF CONTENTS

Sl No	CONTENT	PAGE NO
1	Introduction	7
2	Luminescence properties	10
3	Luminescence mechanisms	11
4	Factors affecting luminescence	12
5	Photoluminescence	14
5.1	Importance of photoluminescence	16
5.2	Application of photoluminescence	17
6	Up conversion Luminescence nanomaterials	19
7	Applications of luminescent nanomaterials	20-23
7.1	Bioimaging	20
7.2	Fluorescence Resonance Energy Transfer	21
7.3	Photodynamic therapy	22
7.4	Aggregation Induced Emissions	23
8	Abbreviation	24
9	Figure Description	25
10	Conclusion	26
11	Reference	27

Hydrothermal Synthesis of Fluorescent Carbon Dots: A Tutorial Review

A project report

Submitted to St. John's College, Anchal for the requirement of

Bachelor of Science in Physics

By

ANANDU JYOTHI (23021138006)

NANDHANA S (23021138011)

SURYA S (23021138015)

Under the guidance of

Dr. JIJI S.G.

Assistant Professor

St. John's College, Anchal, Kollam.

CERTIFICATE

This is to certify that the project entitled “**Hydrothermal Synthesis of Fluorescent Carbon Dots: A Tutorial Review** ” submitted by **ANANDU JYOTHI** (23021138006), **NANDHANA S** (23021138011), **SURYA S** (23021138015) carried out in the Department of Physics, St. John’s College, Anchal for the partial fulfillment for the degree program Bachelor of Science in Physics under the guidance and supervision of **Dr. JJI S.G.** , Assistant Professor, Department of Physics, St. John’s College, Anchal, Kollam during the academic year of 2023-2024.

This work is original and has not been submitted earlier for the award of any other degree.

Place: Anchal


Date: May 2024

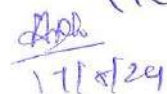


Head of the Department:

Dr BENZON K B
HOD & Assistant Professor
Department of Physics
St John's College, Anchal- 691305

Examiners:

i. 
17/5/24

ii. 
17/5/24



CERTIFICATE

This is to certify that the project entitled “**Hydrothermal Synthesis of Fluorescent Carbon Dots: A Tutorial Review** ” submitted by **ANANDU JYOTHI** (23021138006), **NANDHANA S** (23021138011), **SURYA S** (23021138015) carried out in the Department of Physics, St. John’s College, Anchal for the partial fulfillment for the degree program Bachelor of Science in Physics under the guidance and supervision of **Dr. JIJI S.G.** , Assistant Professor, Department of Physics, St. John’s College, Anchal, Kollam during the academic year of 2023-2024.

This work is original and has not been submitted earlier for the award of any other degree.

Place: Anchal

Date: May 2024



15/05/2024
Dr. JIJI S.G.
Assistant Professor
Department of Physics
St. John's College
Anchal, Kollam - 691306

DECLARATION

We **ANANDU JYOTHI** (23021138006), **NANDHANA S** (23021138011), **SURYA S** (23021138015) declare that this project work entitled “**Hydrothermal Synthesis of Fluorescent Carbon Dots: A Tutorial Review**” was carried out by us under the guidance and supervision of **Dr. JIJIS.G**, Assistant Professor, Department of Physics, St. John’s College, Anchal during the academic year 2023-2024 for the award of the degree of Bachelor of Science in Physics. This project is original, and is not submitted in part or full for any other degree or any other University.

Place: Anchal

Date: May 2024

ACKNOWLEDGEMENT

First and foremost, we bow down before Lord almighty for his blessings and care in completing our project work and throughout our life till this very second.

It is with great pleasure that we **ANANDU JYOTHI** (23021138006), **NANDHANA S** (23021138011), **SURYA S** (23021138015) present the project entitled “**Hydrothermal Synthesis of Fluorescent Carbon Dots: A Tutorial Review**”.

We would also like to express our sincere and special gratitude to **Dr. JIJI S.G**, Assistant Professor, for her guidance, tactful advice and immense encouragement that made us complete the project.

We record our sincere thanks to Dr. Benzon K.B, Assistant Professor & Head of Department of Physics, St .John’s College, Anchal, Kollam for his valuable support.

We owe our sincere thanks to our parents who supported and encouraged us during this work. Friends are the treasures to us and it is difficult to overstate our thanks to all our friends and colleagues. We wish to extend our warmest thanks to our classmates for their support. We feel delighted to express our wholehearted gratitude to all those who gave their helping hands in completing our project successfully.

TABLE OF CONTENTS

CHAPTER -1: WHAT IS NANOSCIENCE?	1
1.1 NANOSCIENCE	1
1.2 NANOSCALE STRUCTURES	1
1.3 NANOMATERIALS	1
1.4 NANOPARTICLES	2
1.5 SYNTHESIS STRATEGIES	3
1.6 CARBON NANOPARTICLES	4
1.6.1 Carbon Dots (CDs)	5
1.6.2 Green Synthesis of Carbon Dots	6
1.6.3 Applications	8
1.6.4 Futuristic perspectives	9
REFERENCES	10
CHAPTER -2: CHARACTERIZATION TECHNIQUES	12
2.1 INTRODUCTION	12
2.2 PROPERTIES OF CDs	12
2.2.1 Physiological Properties	12
2.2.2 Electrochemical Properties	12
2.2.3 Chemical Properties	13
2.2.4 Optical Properties	13
2.2.4.1 Absorbance	13
2.2.4.2 Photoluminescence	14
2.3 OPTICAL CHARACTERIZATION TECHNIQUES	14
2.3.1 UV visible absorption	14
2.3.2 Photoluminescence & Electroluminescence (PL)	15
2.3.3 Fourier Transform Infrared Spectroscopy	17
2.3.4 Raman Spectroscopy	17
2.4 MORPHOLOGICAL ANALYSIS	18
	VI

2.4.1 Electron microscopy: SEM and TEM	18
2.5 X-RAY DIFFRACTION ANALYSIS	20
REFERENCES	22
CHAPTER – 3: RESULTS & DISCUSSIONS	23
3.1 INTRODUCTION	23
3.2 SYNTHESIS	24
3.3 CHARACTERISATION	25
3.3.1 U-V Visible Absorption Spectra	25
3.3.2 XRD Analysis	27
3.3.3 FTIR	28
3.3.4 HRTEM & TEM	30
3.3.5 Photoluminescence	31
3.4 APPLICATION	32
3.5 COMPARISON	32
3.6 CONCLUSION	35
REFERENCE	37

LIST OF FIGURES

1. Figure 1.1. Types of Nanomaterials	2
2. Figure 1.2: Types of carbon nanoparticles	4
3. Figure 1.3 Scheme showing methods and applications of CDs	5
4. Figure: 1.4 –Classification of carbon dots	6
5. Figure 1.5 Scheme showing biogenic synthesis and application of CDs	7
6. Figure 2.1: The UV-visible absorption spectrum of fluorescent CQDs	13
7. Figure 2.2: Schematic diagram of the main components of a UV-vis spectrometer	15
8. Figure 2.3: Schematic illustration of main components of a spectrofluorometer	16
9. Figure 2.4: Illustration of photoluminescence	16
10. Figure 2.5 : Scheme illustrate the components of SEM	19
11. Figure 2.6 -Scheme showing the main components of TEM	20
12. Figure 3.1 - Parts of a plant used for the synthesis of CDs	24
13. Figure 3.2: The raw materials used in the synthesis processes	25
14. Figure 3.3 UV- Vis spectra of (a) Banana juice (b) orange juice (c) Sugarcane bagasse (d) Prosopis juliflora (e) Trapa bispinosa	26
15. Figure 3.4– The XRD spectra of (a) Banana juice (b) orange juice (c) Prosopis juliflora (d) Trapa bispinosa (e) sugarcane bagasse	28
16. Figure 3.5: FTIR spectra of (a) Trapa bispinosa (b) sugarcane bagasse (c) Banana juice (d) Prosopis juliflora (e) orange juice	29
17. Figure 3.6- HRTEM & TEM images of (a) Trapa bispinosa (b) Sugarcane bagasse(c) Banana juice (d) Prosopis juliflora (e) orange juice	30
18. Figure 3.7– The PL Spectra of (a) Trapa bispinosa (b) sugarcane bagasse (c) Banana juice (d) orange juice (e) Prosopis juliflora	31

LIST OF TABLES:

❖ Table 3.1 shows the comparison of CDs from all five selected papers.	32
--	----

Hydrothermal Synthesis of Fluorescent Carbon Dots: A Tutorial Review

A project report

Submitted to St. John's College, Anchal for the requirement of

Bachelor of Science in Physics

By

ANANDU JYOTHI (23021138006)

NANDHANA S (23021138011)

SURYA S (23021138015)

Under the guidance of

Dr. JIJI S.G.

Assistant Professor

St. John's College, Anchal, Kollam.

CERTIFICATE

This is to certify that the project entitled “**Hydrothermal Synthesis of Fluorescent Carbon Dots: A Tutorial Review** ” submitted by **ANANDU JYOTHI** (23021138006), **NANDHANA S** (23021138011), **SURYA S** (23021138015) carried out in the Department of Physics, St. John’s College, Anchal for the partial fulfillment for the degree program Bachelor of Science in Physics under the guidance and supervision of **Dr. JIJI S.G.** , Assistant Professor, Department of Physics, St. John’s College, Anchal, Kollam during the academic year of 2023-2024.

This work is original and has not been submitted earlier for the award of any other degree.

Place: Anchal


Date: May 2024

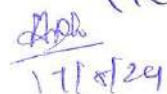


Head of the Department:

Dr BENZON K B
HOD & Assistant Professor
Department of Physics
St John's College, Anchal- 691305

Examiners:

i. 
17/5/24

ii. 
17/5/24



CERTIFICATE

This is to certify that the project entitled “**Hydrothermal Synthesis of Fluorescent Carbon Dots: A Tutorial Review** ” submitted by **ANANDU JYOTHI** (23021138006), **NANDHANA S** (23021138011), **SURYA S** (23021138015) carried out in the Department of Physics, St. John’s College, Anchal for the partial fulfillment for the degree program Bachelor of Science in Physics under the guidance and supervision of **Dr. JJI S.G.** , Assistant Professor, Department of Physics, St. John’s College, Anchal, Kollam during the academic year of 2023-2024.

This work is original and has not been submitted earlier for the award of any other degree.

Place: Anchal

Date: May 2024



15/05/2024
Dr. JJI S.G.
Assistant Professor
Department of Physics
St. John's College
Anchal, Kollam - 691306

DECLARATION

We **ANANDU JYOTHI** (23021138006), **NANDHANA S** (23021138011), **SURYA S** (23021138015) declare that this project work entitled “**Hydrothermal Synthesis of Fluorescent Carbon Dots: A Tutorial Review**” was carried out by us under the guidance and supervision of **Dr. JIJIS.G**, Assistant Professor, Department of Physics, St. John’s College, Anchal during the academic year 2023-2024 for the award of the degree of Bachelor of Science in Physics. This project is original, and is not submitted in part or full for any other degree or any other University.

Place: Anchal

Date: May 2024

ACKNOWLEDGEMENT

First and foremost, we bow down before Lord almighty for his blessings and care in completing our project work and throughout our life till this very second.

It is with great pleasure that we **ANANDU JYOTHI** (23021138006), **NANDHANA S** (23021138011), **SURYA S** (23021138015) present the project entitled “**Hydrothermal Synthesis of Fluorescent Carbon Dots: A Tutorial Review**”.

We would also like to express our sincere and special gratitude to **Dr. JIJI S.G**, Assistant Professor, for her guidance, tactful advice and immense encouragement that made us complete the project.

We record our sincere thanks to Dr. Benzon K.B, Assistant Professor & Head of Department of Physics, St .John’s College, Anchal, Kollam for his valuable support.

We owe our sincere thanks to our parents who supported and encouraged us during this work. Friends are the treasures to us and it is difficult to overstate our thanks to all our friends and colleagues. We wish to extend our warmest thanks to our classmates for their support. We feel delighted to express our wholehearted gratitude to all those who gave their helping hands in completing our project successfully.

TABLE OF CONTENTS

CHAPTER -1: WHAT IS NANOSCIENCE?	1
1.1 NANOSCIENCE	1
1.2 NANOSCALE STRUCTURES	1
1.3 NANOMATERIALS	1
1.4 NANOPARTICLES	2
1.5 SYNTHESIS STRATEGIES	3
1.6 CARBON NANOPARTICLES	4
1.6.1 Carbon Dots (CDs)	5
1.6.2 Green Synthesis of Carbon Dots	6
1.6.3 Applications	8
1.6.4 Futuristic perspectives	9
REFERENCES	10
CHAPTER -2: CHARACTERIZATION TECHNIQUES	12
2.1 INTRODUCTION	12
2.2 PROPERTIES OF CDs	12
2.2.1 Physiological Properties	12
2.2.2 Electrochemical Properties	12
2.2.3 Chemical Properties	13
2.2.4 Optical Properties	13
2.2.4.1 Absorbance	13
2.2.4.2 Photoluminescence	14
2.3 OPTICAL CHARACTERIZATION TECHNIQUES	14
2.3.1 UV visible absorption	14
2.3.2 Photoluminescence & Electroluminescence (PL)	15
2.3.3 Fourier Transform Infrared Spectroscopy	17
2.3.4 Raman Spectroscopy	17
2.4 MORPHOLOGICAL ANALYSIS	18
	VI

2.4.1 Electron microscopy: SEM and TEM	18
2.5 X-RAY DIFFRACTION ANALYSIS	20
REFERENCES	22
CHAPTER – 3: RESULTS & DISCUSSIONS	23
3.1 INTRODUCTION	23
3.2 SYNTHESIS	24
3.3 CHARACTERISATION	25
3.3.1 U-V Visible Absorption Spectra	25
3.3.2 XRD Analysis	27
3.3.3 FTIR	28
3.3.4 HRTEM & TEM	30
3.3.5 Photoluminescence	31
3.4 APPLICATION	32
3.5 COMPARISON	32
3.6 CONCLUSION	35
REFERENCE	37

LIST OF FIGURES

1. Figure 1.1. Types of Nanomaterials	2
2. Figure 1.2: Types of carbon nanoparticles	4
3. Figure 1.3 Scheme showing methods and applications of CDs	5
4. Figure: 1.4 –Classification of carbon dots	6
5. Figure 1.5 Scheme showing biogenic synthesis and application of CDs	7
6. Figure 2.1: The UV-visible absorption spectrum of fluorescent CQDs	13
7. Figure 2.2: Schematic diagram of the main components of a UV-vis spectrometer	15
8. Figure 2.3: Schematic illustration of main components of a spectrofluorometer	16
9. Figure 2.4: Illustration of photoluminescence	16
10. Figure 2.5 : Scheme illustrate the components of SEM	19
11. Figure 2.6 -Scheme showing the main components of TEM	20
12. Figure 3.1 - Parts of a plant used for the synthesis of CDs	24
13. Figure 3.2: The raw materials used in the synthesis processes	25
14. Figure 3.3 UV- Vis spectra of (a) Banana juice (b) orange juice (c) Sugarcane bagasse (d) Prosopis juliflora (e) Trapa bispinosa	26
15. Figure 3.4– The XRD spectra of (a) Banana juice (b) orange juice (c) Prosopis juliflora (d) Trapa bispinosa (e) sugarcane bagasse	28
16. Figure 3.5: FTIR spectra of (a) Trapa bispinosa (b) sugarcane bagasse (c) Banana juice (d) Prosopis juliflora (e) orange juice	29
17. Figure 3.6- HRTEM & TEM images of (a) Trapa bispinosa (b) Sugarcane bagasse(c) Banana juice (d) Prosopis juliflora (e) orange juice	30
18. Figure 3.7– The PL Spectra of (a) Trapa bispinosa (b) sugarcane bagasse (c) Banana juice (d) orange juice (e) Prosopis juliflora	31

LIST OF TABLES:

❖ Table 3.1 shows the comparison of CDs from all five selected papers.	32
--	----

CHAPTER 1

NANOSCIENCE

1.1 NANOSCIENCE

The word Nanoscience refers to the study, manipulation, and engineering of matter particles and structures on the nanometer scale (one millionth of a millimeter, the scale of atoms and molecules). Important properties of materials, such as the electrical, optical, thermal and mechanical properties, are determined by the way molecules and atoms assemble on the nanoscale into larger structures. The National Nanotechnology Initiative (NNI) in the United States defines nanotechnology as “a science, engineering, and technology conducted at the nanoscale (1–100 nm), where unique phenomena enable novel applications in a wide range of fields, from chemistry, physics and biology, to medicine, engineering, and electronics.” Nanotechnology is also called an enormous change from the small world and can play an active role everywhere needed. The concept of a “nanometer” was first suggested by Richard Zsigmondy who has won the 1925 Nobel Prize Laureate in chemistry. Richard Feynman is recognized as the father of modern nanotechnology, but the prime pioneer of nanoscience and nanotechnology is not identified. [1]

1.2 NANO SCALE STRUCTURES

A nanostructure is a structure of intermediate size between microscopic and molecular structures. Nanostructural detail is microstructure at nanoscale. Nano textured surfaces have one dimension on the nanoscale, i.e., only the thickness of the surface of an object is between 0.1 and 100 nm. Nanotubes have two dimensions on the nanoscale, i.e., the diameter of the tube is between 0.1 and 100 nm; its length can be far more. Finally, spherical nanoparticles have three dimensions on the nanoscale, i.e., the particle is between 0.1 and 100 nm in each spatial dimension. The term nanostructure is often used when referring to magnetic technology. Nanoscale structure in biology is often called ultrastructure [2].

1.3 NANOMATERIALS

The key elements of nanotechnology are the nanomaterials. Nanomaterials are defined as materials where at least one of their dimensions is in the nanoscale, i.e. smaller

than 100 nm. Based on their dimensionalities, nanomaterials are placed into four different classes, summarized in Fig. 1.1 [3].

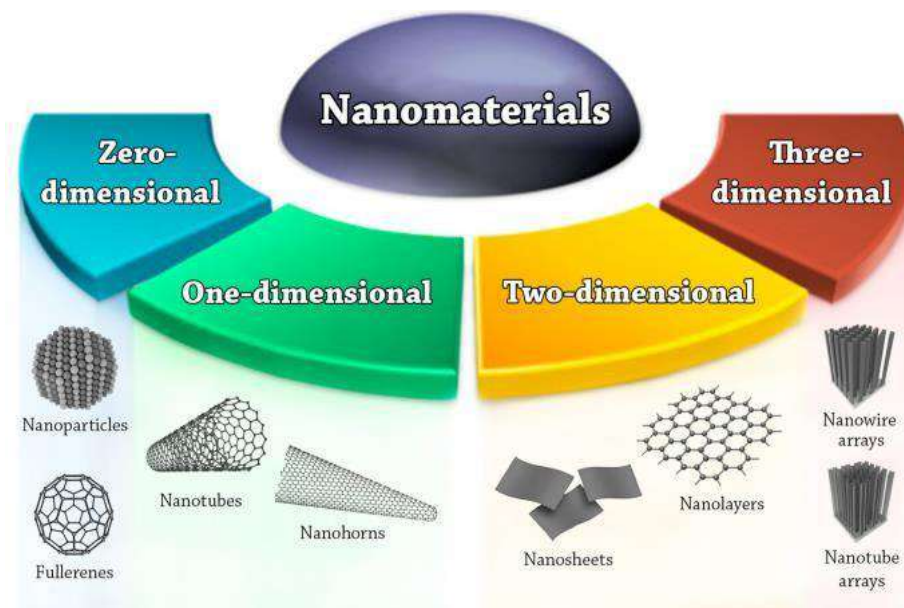


Figure 1.1. Types of Nanomaterials [1]

- 1. Zero-dimensional nanomaterials (0-D):** the nanomaterials in this class have all their three dimensions in the nanoscale range. Examples are quantum dots, fullerenes, and nanoparticles. [1]
- 2. One-dimensional nanomaterials (1-D):** the nanomaterials in this class have one dimension outside the nanoscale. Examples are nanotubes, Nano fibers, Nano rods, nanowires, and Nano horns. [1]
- 3. Two-dimensional nanomaterials (2-D):** the nanomaterials in this class have two dimensions outside the nanoscale. Examples are Nano sheets, Nano films, and nanolayers. [1]
- 4. Three-dimensional nanomaterials (3-D) or bulk nanomaterials:** In this class the materials are not confined to the nanoscale in any dimension. This class contains bulk powders, dispersions of nanoparticles, arrays of nanowires and nanotubes, etc. [1].

1.4 NANOPARTICLES

The International Organization for Standardization (ISO) defines nanoparticles as Nano-objects with all external dimensions in the nanoscale, where the lengths of the longest and the

shortest axes of the Nano-object do not differ significantly. NPs can be of different shapes, sizes, and structures. They can be spherical, cylindrical, conical, tubular, hollow core, spiral, etc., or irregular. The size of NPs can be anywhere from 1 to 100 nm. If the size of NPs gets lower than 1 nm, the term atom clusters is usually preferred. NPs can be crystalline with single or multi-crystal solids, or amorphous. NPs can be either loose or agglomerated [2].

Based on their composition, NPs are generally placed into three classes:

- Organic,
- Carbon-based
- Inorganic
- Composite

Organic NPs comprises NPs that are made of proteins, carbohydrates, lipids, polymers, or any other organic compounds. The most prominent examples of this class are dendrimers, liposomes, micelles, and protein complexes such as ferritin. Carbon based NPs comprises of NPs that are made solely from carbon atoms. Famous examples of this class are fullerenes, carbon black NPs, and carbon quantum dots. Inorganic NPs comprises NPs that are not made of carbon or organic materials. The typical examples of this class are metal, ceramic, and semiconductor NPs. The composite nanomaterials are the combination of metal-based, metal oxide-based, carbon-based, and or organic-based nanomaterials, and these nanomaterials have complicated structures. [4]

1.5. SYNTHESIS STRATEGIES

There are two basic approaches commonly employed to prepare NPs;

1. **Top-down approach**, where synthesis is initialized with the bulk counterpart that leaches out systematically bit-after-bit leading to the generation of fine NPs. Photolithography, electron beam lithography, milling techniques, anodization, ion and plasma etching are some of the commonly used top-down methods for the mass production of NPs. [18]
2. **Bottom-up approach**, which involves the coalescence or assembling of atoms and molecules to generate diverse range of NPs. Examples of bottom-up approach include self-assembly of monomer/polymer molecules, chemical or electrochemical Nanostructural precipitation, sol–gel processing, laser pyrolysis, chemical vapor deposition (CVD), plasma or flame spraying synthesis and bio-assisted synthesis.[19]

In general, NP synthesis methods can be divided in three groups –

- Physical methods
- Chemical methods
- Bio-assisted methods

1.6 CARBON NANOPARTICLES

Carbon is one of the most abundant minerals on Earth. It is one component of a large number of macromolecules that are essential for life, including sugars, proteins, DNA; etc. Pure carbon exists in various forms, such as allotropes. The extraordinary properties of carbon are exploited in carbon-based nanomaterials. CNPs represent a wide range of carbon individuals, including amorphous carbon nanoparticles (ultrafine carbon particles, carbon nanoparticles, and carbon dots), sp^2 carbon nanomaterials (fullerene, carbon nanotubes, carbon nanohorns, graphene, graphene quantum dots), and nanodiamonds.

CNPs are formed from pure carbon; therefore, they have high stability, outstanding electrical and heat conductivity, mechanical properties (extreme stiffness, strength, and toughness), and are highly biocompatible with low toxicity; furthermore, they are highly hydrophobic due to their sp^2 hybridization. One of the most studied CNPs is graphene, which is a structural parent of several carbon allotropes (graphenoids), including nanorings, single-, double-, and multi-walled nanotubes, graphite, carbon fibers, and graphyne (Figure 1.2).

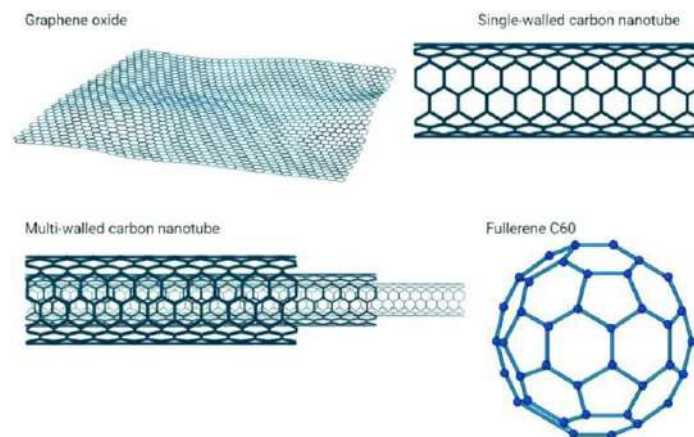


Figure 1.2: Types of carbon nanoparticles.[3]

1.6.1 Carbon Dots (CDs)

Carbon dots (CDs) are a newly developed type of carbon nanomaterial and composed of discrete, quasi-spherical nanoparticles. They were first discovered from the components of

fluorescent nanoparticles during single-walled carbon nanotubes purification in 2004. Until 2006, these carbon nanoparticles were named as “carbon quantum dots” .As one of the new allotropes of carbon, CDs show many remarkable advantages, such as low cytotoxicity , good biocompatibility , stable chemical inertness , efficient light harvesting and outstanding photo induced electron transfer ,thus making them promising candidates for various applications in biosensors, bio-imaging ,optoelectronic devices , solar cells, etc.[6,9]

Carbon dots (CDs) are a type of carbon-based nanomaterial with fluorescence properties, consisting of carbon nanoparticles with quasi-spherical structures with a size of less than 10 nm .They generally have O/N g functional groups such as amino group (-NH₂),carboxyl group (-COOH) and hydroxyl group(-OH). Carbon dots, are generally categorized into three types, namely,

- 1) Carbonized Polymeric Dots (CPDs)
- 2) Graphene Quantum Dots (GQDs)
- 3) Carbon Quantum Dots (CQDs)
- 4) Carbon Nanodots (CNDs)

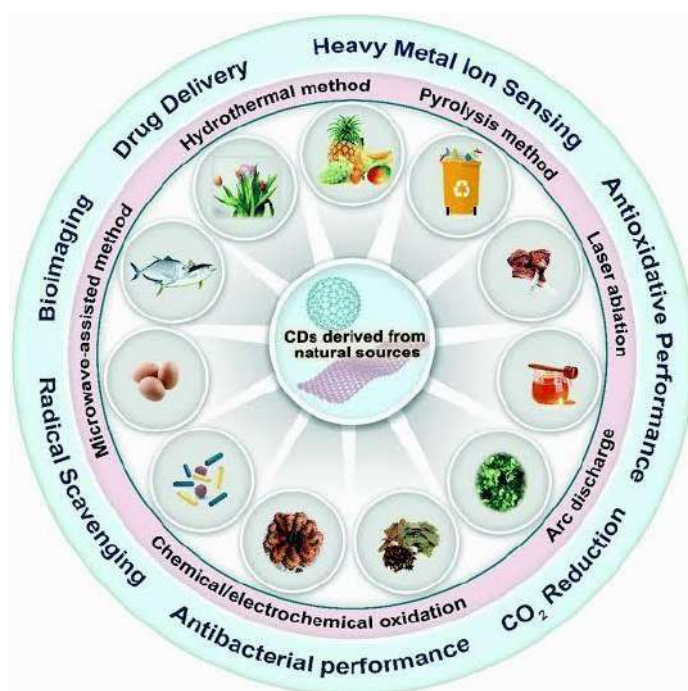


Figure 1.3 Scheme showing methods and applications of CDs [2]

GQDs, or graphene quantum dots, are small graphene Fragments consisting of a single grapheme sheet or a few grapheme sheets with obvious grapheme Lattices and chemical groups on the edge or within the interlayer defect; CQDs, or carbon quantum Dots are always spherical and possess obvious crystal lattices and chemical groups on the surface; CNDs, or carbon Nano dots, possess a high carbonization degree with some chemical groups on the surface, but usually show no obvious crystal lattice structure and polymer features; CPDs, or Carbonized polymer dots, possess a polymer/carbon hybrid structure comprising abundant functional groups/polymer chains on the surface and a carbon core.[5]

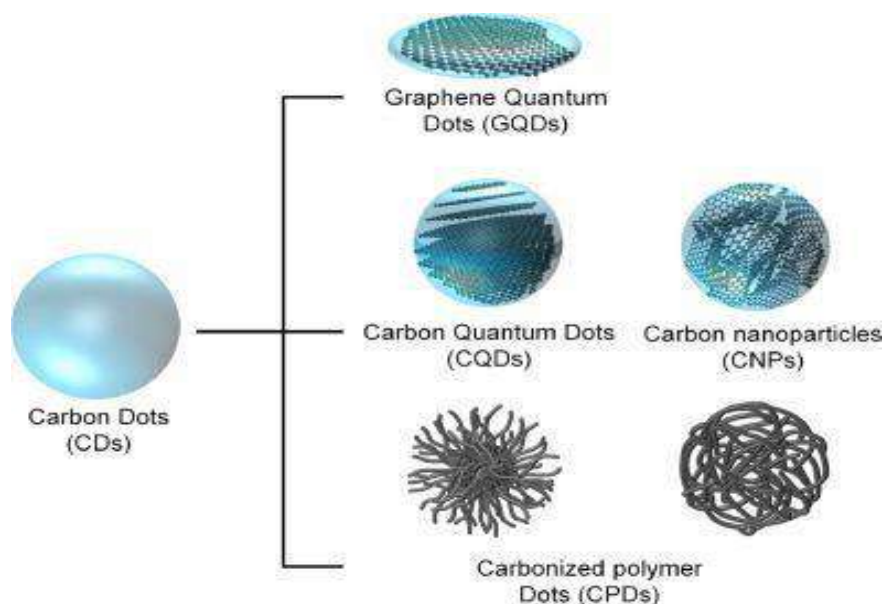


Figure: 1.4 –Classification of carbon dots [3]

1.6.2 Green Synthesis of Carbon Dots

Chemical based synthesis of carbon dots may limit its clinical application due to its toxicity. In order to find a solution to this problem green synthesis of carbon dots is introduced. Green synthesis of carbon dots includes hydrothermal method, high-temperature pyrolysis, microwave method, and solvothermal method (Fig 1.5)

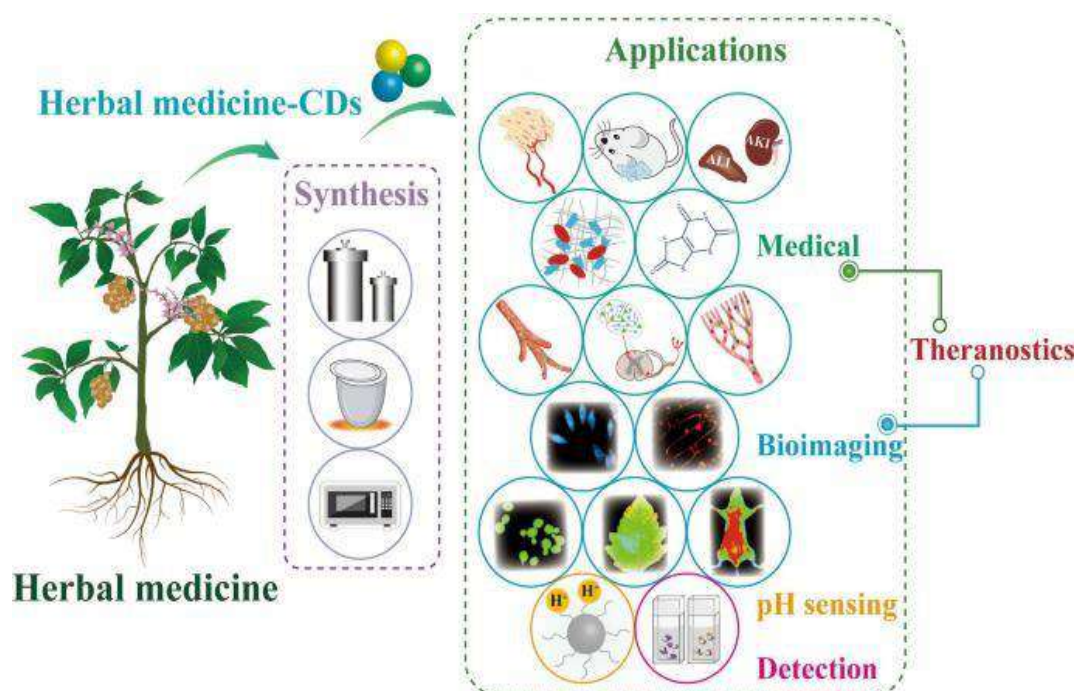


Figure 1.5 Scheme showing biogenic synthesis and application of CDs [8]

1. Owing to its low cost and ease of implementation, **Hydrothermal Synthesis** is the most common green CD preparation method. The hydrothermal process for carbon dot synthesis involves the utilization of water as a reaction medium under high temperature and pressure conditions to generate carbon dots [Feng & Li, 2017] from carbon-containing precursors. During the hydrothermal process, the carbon-containing precursor is mixed with an aqueous solution and placed within a sealed reaction vessel. The mixture is then heated to a specific temperature and maintained under high pressure for a certain period of time. Under these conditions, the carbon-containing precursor undergoes various chemical reactions, leading to the formation of carbon dots. These carbon dots can then be recovered and further characterized for their size, morphology, and optical properties. Some commonly used precursors for making carbon dots through the hydrothermal process include candle soot, glucose, graphite, carbon nanotubes, and graphene, among others [19]. The hydrothermal process for carbon dot synthesis involves using water as a reaction medium under high temperature and pressure conditions to generate carbon dots from carbon-containing precursors.[11]

2. **Solvent-free synthesis** (i.e., dry heating) is usually performed at temperatures as high as 300°C under ambient pressure conditions. Although simple to implement, these approaches require high temperatures and long reaction times. These reaction parameters can

be readily optimized to maximize product yield and application-specific performance while minimizing energy requirements. [10]

3. Microwave synthesis is advantageous as it enables direct heating of reaction mixtures, typically using 800 W of microwave power for only a few minutes. Unlike hydrothermal synthesis that relies on conductive heat transfer, microwaves allow for direct and selective heating via resonance with the vibrational frequencies of molecules. Therefore, a microwave reaction is often complete before an appreciable change in temperature of an equivalent hydrothermal synthesis is attained.[10]

1.6.3 Applications

1. Chemical sensing: Chemical sensing is typically performed by monitoring changes in CD fluorescence or absorbance in the presence of a target analyte. N/P doped CDs synthesized from *Eleocharis dulcis* (water chestnut) juice exhibit high selectivity towards Fe^{3+} relative to other metals. [13]

2. Bioimaging: Bioimaging is one of the most studied applications of CDs due to their generally low cytotoxicity and resistance to photo bleaching. CDs synthesized from watermelon peels we used to image He-La cells, demonstrating that CDs can be good candidates for Bioimaging due to their stability in aqueous solutions, small size, and strong fluorescence. Some CDs exhibit excitation-dependent fluorescence allowing for their use in multicolor fluorescence imaging. This feature can be useful when imaging cells, tissues, or organisms which exhibit auto-fluorescence by allowing the user to easily switch between fluorescence wavelengths while using a single type of CD. [12]

3. Ink: Inexpensive fluorescent inks for anti-counterfeiting applications (e.g., invisible security inks) have been developed using green-synthesized CDs. For instance, CDs synthesized from oriental plane leaves were used as fluorescent inks to print patterns that were invisible under daylight and became visible under UV light Similarly, CDs synthesized from milk which were used as fluorescent inks. They were able to refill regular commercial inkjet cartridges with their CDs which were then used to produce fluorescent patterns on commercial paper .In another green synthesis, used citric acid and urea to produce CDs with fluorescent patterning capabilities. [14, 15, 16].

4. Catalysis: With their high surface area-to-volume ratio and their versatile functional groups, CDs find application in catalysis. CDs synthesized from willow bark were

used as a photocatalyst for the fabrication of an Au nanoparticle/reduced graphene oxide nanocomposite, demonstrating that the CDs effectively reduced both materials. The resulting nanocomposite was used in a system that catalyzes the reaction of glucose and oxygen into H_2O_2 allowing it to be an indirect method of glucose sensing via the detection of H_2O_2 . The use of waste products in green synthesis is often desirable to reduce the overall environmental impact of the synthesis process.[17]

1.6.4 Futuristic perspectives

Carbon dots offer several advantages compared to traditional organic dyes or semiconductor quantum dots, such as low toxicity, good biocompatibility, and high photo stability. They can be used in various bioimaging applications, including fluorescence imaging, intracellular imaging, and biosensors. Carbon dots have a high quantum yield, making them effective fluorescent probes for detecting cancer cells, pathogens, and other biological targets. Their small size and ability to penetrate cell membranes make them ideal for imaging intracellular structures and studying cellular processes such as endocytosis, exocytosis, and cell division. In addition, carbon dots can be used as biosensors to detect specific biomolecules or environmental factors, such as glucose, heavy metals, and other chemicals in biological and environmental samples.

Another potential application of CDs in medicine is in drug delivery. CDs can be functionalized with different types of molecules such as drugs, peptides, or nucleic acids, and can be used to deliver these molecules to specific cells or tissues. CDs have shown promise for delivering drugs to cancer cells, for example, by targeting tumor-associated macrophages or by enhancing the therapeutic efficacy of chemotherapy drugs. [20]

REFERENCES

- 1) <https://www.science.org.au/curious/nanoscience>
- 2) <https://en.wikipedia.org/wiki/Nanostructure>.
- 3) Carbon Nanoparticles and Their Biomedical Applications by Drahomira Holmannova ORCID, Pavel Borsky ,*ORCID, Tereza Svadlakova ORCID, Lenka Borska ORCID and Zdenek Fiala.
- 4) Chetna Dhand, Neeraj Dwivedi, Xian Jun Loh, Alice Ng Jie Ying, Navin Kumar Verma, Roger W. Beuerman, Rajamani Lakshminarayanan and Seeram Ramakrishna; Methods and strategies for the synthesis of diverse nanoparticles and their applications: a comprehensive overview , RSC Adv., 2015, 5, 105003
- 5) <https://www.azonano.com>
- 6) Junjun Liu, Rui Li, and Bai Yang, Carbon Dots: A New Type of Carbon-Based Nanomaterial with Wide Applications, ACS Central Science 2020 6 (12), 2179-2195
- 7) Salata O. Applications of nanoparticles in biology and medicine. J Nanobiotechnology. 2004 Apr 30;2(1):3.
- 8) Luo, WK., Zhang, LL., Yang, ZY. et al. Herbal medicine derived carbon dots: synthesis and applications in therapeutics, bioimaging and sensing. J Nanobiotechnol 19, 320 (2021).
- 9) Junjun Liu, Rui Li, and Bai Yang, Carbon Dots: A New Type of Carbon-Based Nanomaterial with Wide Applications, ACS Central Science 2020 6 (12), 2179-2195
- 10) E. Arkan, A. Barati, M. Rahmanpanah, L. Hosseinzadeh, S. Moradi and M. Hajialyani, Adv. Pharm. Bull., 2018, 8, 149–155.
- 11) Kofi Oti Boakye-Yiadom, Samuel Kesse, Yaw Opoku-Damoah, Mensura Sied Filli, Md Aquib, Mily Maviah Bazezy Joelle, Muhammad Asim Farooq, Rukhshona Mavlyanova, Faisal Raza, Rohit Bavi, Bo Wang International journal of pharmaceutics, 2019.
- 12) H. Li, S. Ye, J. Guo, H. Wang, W. Yan, J. Song and J. Qu, Nano;Res., 2019, 12, 3075–3084
- 13) S. Chahal, N. Youse and N. Tufenkji, ACS Sustainable Chem. Eng., 2020, 8, 5566–5575
- 14) L. Zhu, Y. Yin, C.-F. Wang and S. Chen, J. Mater. Chem. C, 2013, 1, 4925–4932.
- 15) J. Wang, F. Peng, Y. Lu, Y. Zhong, S. Wang, M. Xu, X. Ji, Y. Su, L. Liao and Y. He, Adv. Opt. Mater., 2015, 3, 103–111.
- 16) S. Qu, X. Wang, Q. Lu, X. Liu and L. Wang, Angew. Chem., Int. Ed., 2012, 51, 12215–12218

- 17) Z.-Y. Shih, A. P. Periasamy, P.-C. Hsu and H.-T. Chang, *Appl. Catal., B*, 2013, 132–133, 363–369.
- 18) Sun, Y.P.; Zhou, B.; Lin, Y.; Wang, W.; Fernando, K.A.S.; Pathak, P.; Meziani, M.J.; Harruff, B.A.; Wang, X.; Wang, H.; et al. Quantum-sized carbon dots for bright and colorful photoluminescence. *J. Am. Chem. Soc.* 2006, 128, 7756. [CrossRef] [PubMed]
- 19) Pires, N.R.; Santos, C.M.W.; Sousa, R.R.; De Paula, R.C.M.; Cunha, P.L.R.; Feitosa, J.P.A. Novel and Fast Microwave-Assisted Synthesis of Carbon Quantum Dots from Raw Cashew Gum. *J. Brazil. Chem. Soc.* 2015, 26, 1274–1282. [CrossRef]
- 20) S. N. Baker, G. A. Baker, *Angew. Chem., Int. Ed.* 2010, 49, 6726.
- 21) Fernando, K. A Shiral, Sahu, Sushant, Liu, Yamin, Lewis, William K., Guliants, Elena A., Jafariyan, Amirhossein; Wang, Ping, Bunker, Christopher E Sun, Ya-Ping (2015). "Carbon Quantum Dots and Applications in Photocatalytic Energy Conversion" *ACS Applied Materials & Interfaces* 7 (16) 8363-76. doi: 10.1021/acsami.5b00448 PMID 25845394.

CHAPTER - 2

CHARACTERIZATION TECHNIQUES

2.1 INTRODUCTION

Carbon quantum dots (CQDs), also known as carbon dots (CDs), are zero-dimensional fluorescent carbon-based nanomaterials. CQDs have attracted enormous attention around the world because of their excellent optical properties as well as water solubility, biocompatibility, low toxicity, eco-friendliness, and simple synthesis routes. CQDs have numerous applications in bioimaging, biosensing, chemical sensing, nanomedicine, solar cells, drug delivery, and light-emitting diodes. In this chapter, their physical and chemical properties are incorporated for the better understanding of CD materials.[1]

2.2 PROPERTIES OF CDs

The properties of the Carbon Dots mainly include:

- Physiochemical properties
- Electrochemical properties
- Chemical properties
- Optical properties

2.2.1 .PHYSIOLOGICAL PROPERTIES

The photoluminescence and electronic properties of CDs depend on electronic transitions across the band gap of sp^2 domains, and strongly affected by surface states, fluorophores, and element doping. The quantum confinement effect (QCE) is a major attribute of CDs, especially GQDs and CQDs with crystalline lattice, where the size of CDs is smaller than Bohr radius. [3]

2.2.2. ELECTROCHEMICAL PROPERTIES

The following aspects of CDs are advantages in electrochemistry; (i) large surface area increases electrical conductivity as a result of electron- hole pair formation (ii) low cost and low toxicity (iii) abundant surface functionalities including carboxyl, amino, and hydroxyl groups, all of which enable surface modification to enhance particles stability and fine-tune their chemical and physical properties and (iv) heteroatom doping can increase the electronic

properties of CDs via promoting the intramolecular charge transfer as well as providing reactive sites in electro catalysis . [3]

2.2.3. CHEMICAL PROPERTIES

There are various synthesis methods to prepare various types of CDs with chemical properties depending on the synthesis methods. CNDs are divided into two subgroups: (i) CQDs and (ii) CNPs. CQDs have crystal lattice, while CNPs are spherical shape amorphous particles. There are a variety of characterization techniques to identify the structure of CDs including investigating crystallinity, morphology, size distribution, and chemical functionality like Transmission electron microscopy (TEM), High-resolution transmission electron microscopy (HRTEM), and Atomic force microscopy (AFM), Raman spectroscopy, XRD. [3]

2.2.4 OPTICAL PROPERTIES

The optical properties of CQDs can be customized by doping/co-doping with heteroatoms, functional groups, and surface passivation

2.2.4.1. Absorbance

CQDs generally exhibit two absorption bands in the visible region around 280 nm and 350 nm, alongside a tail broadly in the UV region. Figure 2.1 is the typical UV-visible absorption spectrum of fluorescent CQDs. The absorption properties of CQDs can be influenced by surface modification or surface passivation. Doping in CQDs can also alter the absorption wavelength. [1]

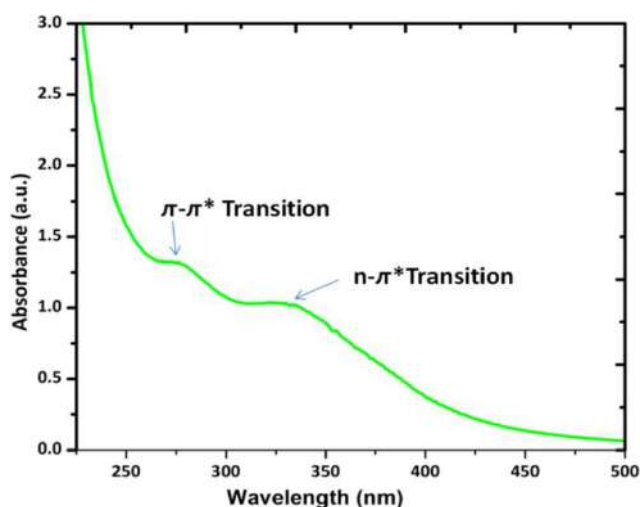


Figure 2.1: The UV-visible absorption spectrum of fluorescent CQDs [2]

2.2.4.2. Photoluminescence

The emission of light from a substance upon the absorption of light (photon) is called photoluminescence (PL). Photoluminescence includes two types, namely fluorescence and phosphorescence. Fluorescent materials emit absorbed light from the lowest singlet excited state (S_1) to the singlet ground state (S_0). This process is very fast and has a nanosecond lifetime. The transitions that occur among two electronic states in the fluorescence process are allowed because it has the same spin multiplicity. In contrast, in phosphorescence, the transition occurs from the lowest triplet excited state (T_1) to singlet ground state (S_0), i.e., a forbidden transition occurs according to the spin selection rule. [2]

2.3 OPTICAL CHARACTERIZATION TECHNIQUES

Optical characterization techniques are used to study the optical properties of materials. There are different techniques used for the study of optical properties. They are done on the basis of measuring absorption, scattering or emission of light. Commonly used techniques include, UV-Visible absorption, Infrared absorption, Raman scattering, photoluminescence, etc. [1]

2.3.1 UV Visible absorption

For studying optical and electronic properties of nanomaterials, one of the simplest and most useful optical techniques is the UV-visible spectrometer. It is a technique based on the measurement of light absorption due to electronic transitions in a sample. Since the wavelength of light required for electronic transitions is typically in the UV and visible region of the electromagnetic radiation spectrum, electronic absorption spectroscopy is often called UV visible or UV-vis spectroscopy. It is named electronic absorption spectroscopy because the absorption in the UV-visible regions involves mostly electronic transitions.

Operating principle:

Based on Beer's law, the absorbance, A , is related to the incident light intensity, I_0 , and transmitted light intensity I , concentration of a solution sample, c , path length of the sample, l , absorption coefficient, α , and molar absorptivity, ϵ , by the following equation:

$$A = \log I_0 / I = \epsilon lc = \alpha c$$

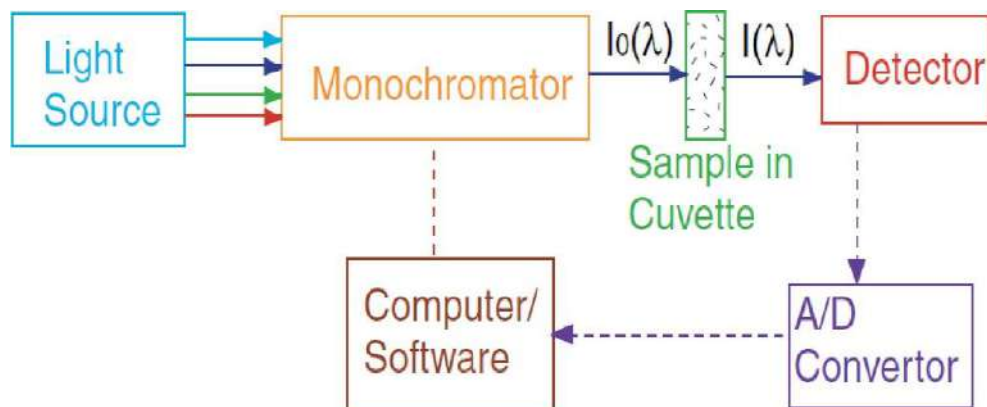


Figure 2.2: Schematic diagram of the main components of a UV-vis spectrometer

The above fig 2.2 shows the diagram of UV-vis spectrometer that includes a light source, e.g. a lamp, monochromator to disperse the incident light, sample cuvette and holder, detector, e.g. PMT, photodiodes or CCD, analog-to-digital (A/D) converters, and computer with software to control the scan of the monochromator and data acquisition. If the sample absorbs light at some wavelength, the transmitted light will be reduced. The intensity of the transmitted light plotted as a function of light wavelength will give a spectrum of the sample absorption. Most spectrometers cover the wavelength range from about 200 nm to 800 nm. [1, 2]

2.3.2 Photoluminescence and electroluminescence spectroscopy

It involves electronic transition of initial and final states coupled by the electrical dipole operator and this transition is from a higher energy level or state to a lower energy level. PL is a zero-background experiment, i.e. no signal detected when there is no PL. Zero-background experiments are intrinsically more sensitive than nonzero background experiments. Therefore, PL is a sensitive technique. A PL spectrum is a plot of the PL intensity as a function of wavelength for a fixed excitation wavelength. A photoluminescence excitation (PLE) spectrum is a measure of PL at a fixed emission wavelength as a function of excitation wavelength.

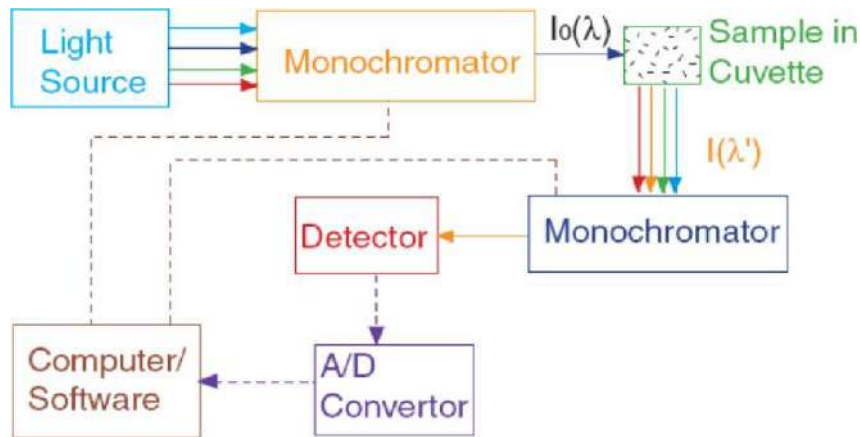


Figure 2.3: Schematic illustration of main components of a spectrofluorometer

Schematic illustration gives components of a typical spectrofluorometer that include a light source, e.g. a lamp, monochromator to disperse the incident light, sample cuvette and holder, a second monochromator to disperse the emitted light, detector, e.g. PMT, photodiodes or CCD, analog-to-digital (A/D) converters, and computer with software to control the scan of the monochromators and data acquisition. PL is important for understanding the structural, surface and energetic properties of Nanomaterials. Besides the PL spectrum, the PL quantum yield, measured as the intensity ratio of the emitted light over the absorbed light, provides important indications about the properties of the nanoparticles. If the PL quantum yield is low, it usually means that the nanoparticles [1, 2]

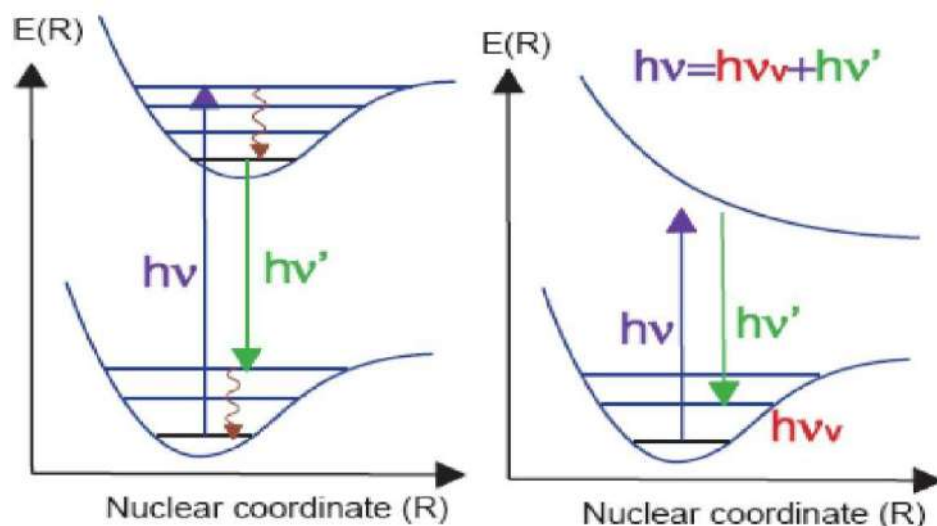


Figure 2.4: Illustration of photoluminescence

2.3.3 Fourier Transform Infrared Spectroscopy

It is a technique to obtain the infrared spectrum of material of absorption or emission. It has the advantage that it collects high resolution spectral data over a wide range, and has the double advantage of measuring the intensity over a narrow range of wavelengths. The term Fourier transform spectroscopy literally originated from the mathematical process called Fourier transform which converts raw data to actual spectrum. The first low cost spectrometer was capable of covering a range of wavelengths from 2.5 to 15 μm ; it was the Perkin -Elmer infracord produced in 1957. [1]

2.3.4 Raman Spectroscopy

Raman spectroscopy is a spectroscopic technique used to detect vibrational, rotational and other states in a molecular system capable of probing the chemical composition of materials. It is based on the phenomenon called Raman scattering, discovered by C.V. Raman in 1928. A single frequency light from a single mode laser source shines on the sample and scattered light is measured at the angle with respect to the incident light to minimize Rayleigh scattering. The inelastically scattered light with lower frequencies called Stokes scattering and with high frequencies called Anti-Stokes scattering can be measured with a photo detector. The energy difference between the scattered and incident light is called Raman shift which is equal to the vibrational or phonon frequencies of the sample. The spectrum is usually presented in terms of the intensity of the Raman scattered light as a function of Raman shift.

There is a similarity between Photoluminescence and Raman scattering that particularly resonance Raman scattering that involves electronic states. Raman can be practically considered as PL involving an extremely short lived excited state called virtual state for normal Raman. If the excited state is very short lived like in dissociated state, resonant excitation would produce primarily Raman scattering and no PL. When the excited state is long lived, PL should be very strong and Raman would be comparatively very weak. A major difference between PL and Raman is that relaxation or energy loss in the excited state usually occurs for PL but not for Raman. So Raman provides specific information about vibrational frequencies in the ground electronic state while PL is determined by the excited and ground electronic states. Raman is a zero background measurement and more sensitive than IR. Raman scattering quantum yield is often very low on the order of 10^{-6} to 10^{-8} . Raman signal

can be enhanced by using light frequency that is in resonance with an electronic transition of sample resonance Raman scattering.

While the signal can be enhanced by a factor of 100-1000, sample degradation often occurs due to the electronic absorption of the incident light and subsequent photochemical reactions. The resonance enhancement is due to the fact that the Raman signal depends on the detuning or energy difference between the electronic and ground electronic states. As this energy difference becomes smaller, the signal becomes larger.

Raman signal can be observed in practical PL measurements mainly when the PL signal is weak. The Raman signal from the embedding medium such as a solvent can be easily seen due to the very high concentration. Raman peaks are narrower than PL peaks especially for nanoparticles. Both IR and Raman have been used for characterizing vibration or phonon features of nanoparticles or molecules associated with nanoparticles such as surfactants and adsorbates. [1, 2]

2.4 MORPHOLOGICAL ANALYSIS

Morphology, that is, the study of form comprising shape, size, and structure, is important for materials research in general.

Morphology of different nanostructures may vary significantly depending on their material composition, crystal structure and manufacturing method. Different shapes of nanomaterials include nanospheres, nanocube, nanowires, nanoreefs, nanoclusters, and nanotubes. Various properties of nanomaterials can be finely tuned based on its morphology, therefore a detailed study on the morphology of nanomaterials and its effect on the optical, electrical, magnetic, electronic, and thermal properties is required. Various morphological characterization techniques are atomic force microscope, scanning electron microscope, transmission electron microscope etc. [1]

2.4.1 Electron microscopy: SEM and TEM

❖ SEM

Scanning electron microscopy (SEM) is a powerful and popular technique for imaging the surfaces of almost any material with a resolution down to about 1 nm. The image resolution offered by SEM depends not only on the property of the electron probe, but also on the

interaction of the electron probe with the specimen. The interaction of an incident electron beam with the specimen produces secondary electrons; with energies typically SEM can thus provide information about the surface topology, morphology and chemical composition.

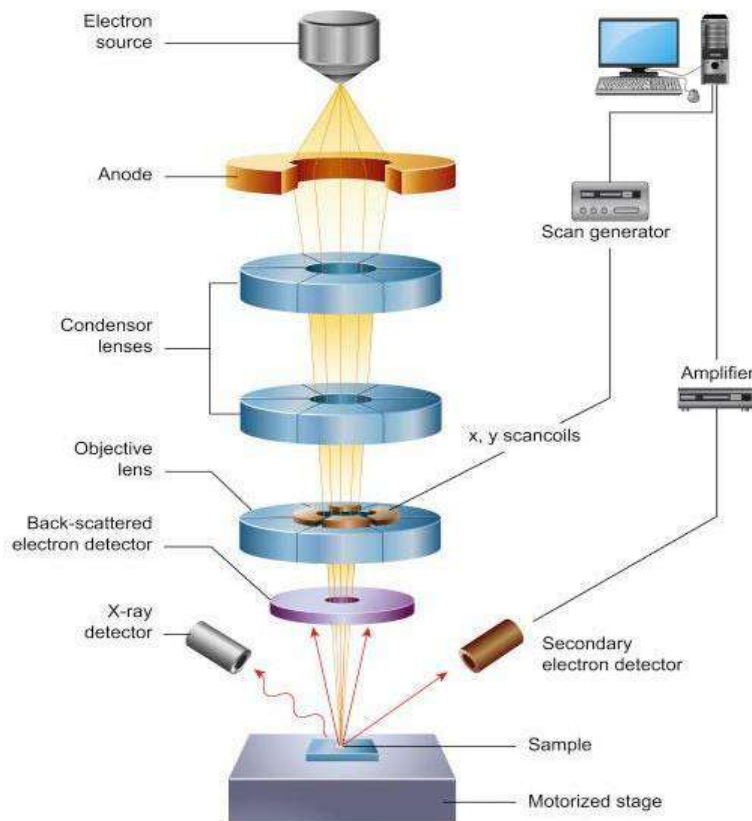


Figure 2.5 : Scheme illustrate the components of SEM [5]

FESEM is the abbreviation of Field Emission Scanning Electron Microscope. FESEM is microscope that works with electrons (particles with a negative charge) instead of light. These electrons are liberated by a field emission source. The object is scanned by electrons according to a zig-zag pattern. The Field Emission Scanning Electron Microscope (FESEM) has a much brighter electron source and smaller beam size than a typical SEM increasing the useful magnification of observation and imaging up to 500,000 x. A second advantage of the FESEM is that high resolution imaging can be performed with very low accelerating voltages. This enhances the observation of very fine materials. Surface features, electron beam sensitive materials, and non-conductive. [1, 2]

❖ TEM

Transmission electron microscopy (TEM) is a high spatial resolution structural and chemical characterization tool. A modern TEM has the capability to directly image atoms in crystalline specimens at resolutions close to 0.1 nm, smaller than interatomic distance. An electron beam

can also be focused to a diameter smaller than ~ 0.3 nm, allowing quantitative chemical analysis from a single nanocrystal.

This type of analysis is extremely important for characterizing materials at a length scale from atoms to hundreds of nanometers. TEM can be used to characterize nanomaterials to gain information about particle size, shape, crystallinity, and interparticle interaction. [1,2]

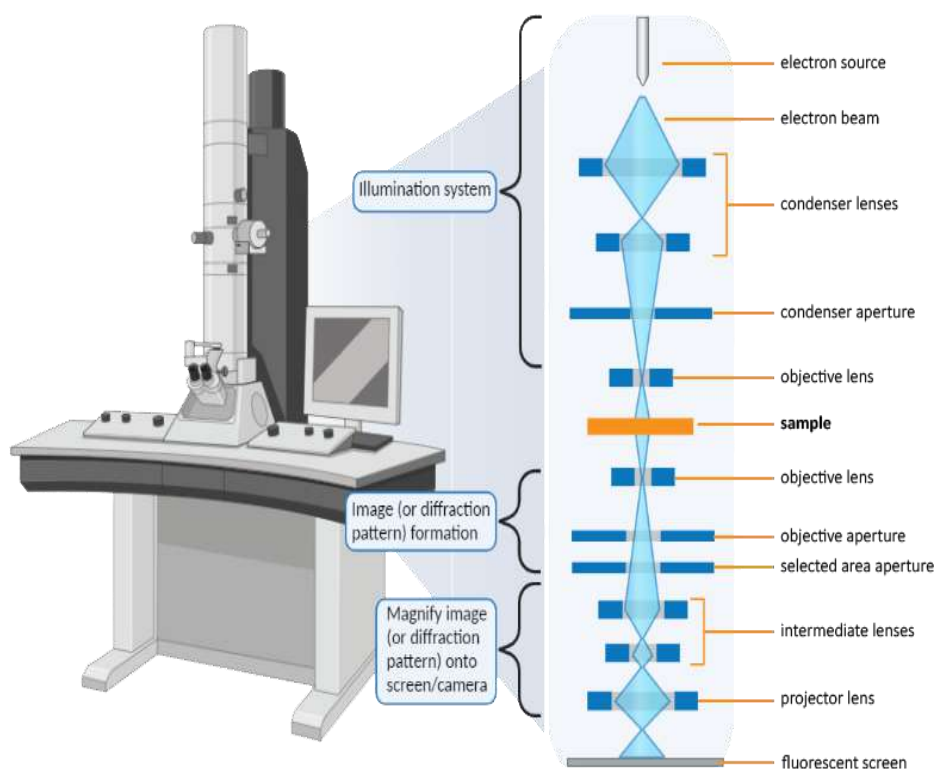


Figure 2.6 -Scheme showing the main components of TEM [6]

2.5 X-ray Diffraction Analysis

X-ray diffraction (XRD) is a powerful and routine technique for determining the crystal structure of crystalline materials. The widths of the diffraction lines are closely related to the size, size distribution, defects and strain in nanocrystals. As the size of the nanocrystals decreases, the line width is broadened due to loss of long range order relative to the bulk. This XRD line width can be used to estimate the size of the particle via the Debye–Scherrer formula; [1, 2]

$$D = \frac{K\lambda}{\beta \cos\theta}$$

D ← *nanocrystal diameter*

K ← *the Scherrer constant (0.98)*

λ ← *wavelength of light*

β ← *full width half at maximum (FWHM) of the peak in radians*

θ ← *Bragg Angle*

REFERENCES

1. Anshida Mayeen, Leyana K. Shaji, Anju K. Nair and Nandakumar Kalarikkal, Chapter 12 - Morphological Characterization of Nanomaterials, Woodhead Publishing, 2018, Pages 335-364,
2. Jin Zhong Zhang, Optical Properties and Spectroscopy of Nanomaterials, World Scientific, Singapore, 2009. Pages 335-364,
3. <https://www.nanoscience.com>
4. X. Wang, Y. Feng, P. Dong, J. Huang, A mini review on carbon quantum dots: preparation, properties, and electrocatalytic application, *Front. Chem.* 7 (2019)
5. B.D. Mansuriya, Z. Altintas, Carbon dots: classification, properties, synthesis, characterization, and applications in health care-an updated review (2018-2021), *Nanomaterials* (10) (2021) 2525 .
6. S.K. Guin, A.S. Ambolikar, J. Paul Guin, S. Neogy, Exploring the excellent photophysical and electrochemical properties of graphene quantum dots for complementary sensing of uranium, *Sens. Actuators B Chem.* 272 (2018) 559–573.
7. L. Đorđević, F. Arcudi, M. Cacioppo, M. Prato, A multifunctional chemical toolbox to engineer carbon dots for biomedical and energy applications, *Nat. Nanotechnol* (2) (2022) 112–130.

CHAPTER – 3

RESULTS & DISCUSSIONS

3.1 INTRODUCTION

Carbon dots (CDs) have emerged as a fascinating class of carbon - based nanomaterials due to their unique properties and environmentally friendly synthesis methods. CDs are nanometer – sized carbonaceous particles, typically less than 10 nm in diameter, with a variety of desirable characteristics such as excellent photoluminescence, biocompatibility, chemical stability, low cost, high availability and low toxicity. These properties make them promising candidates for a wide range of applications in fields such as bioimaging, sensing, drug delivery, and optoelectronics. One of the most compelling aspects of carbon dots is their green synthesis, which aligns with the growing demand for sustainable and ecofriendly manufacturing processes.

In this review, we provide an overview of the synthesis of carbon dots from five different plant extracts like Banana juice, Orange juice, Prosopis juliflora, Sugarcane bagasse and Trapa bispinosa via green synthesis approaches. Understanding the properties and synthesis methods of carbon dots is essential for harnessing their full potential, diverse technological and biomedical applications.

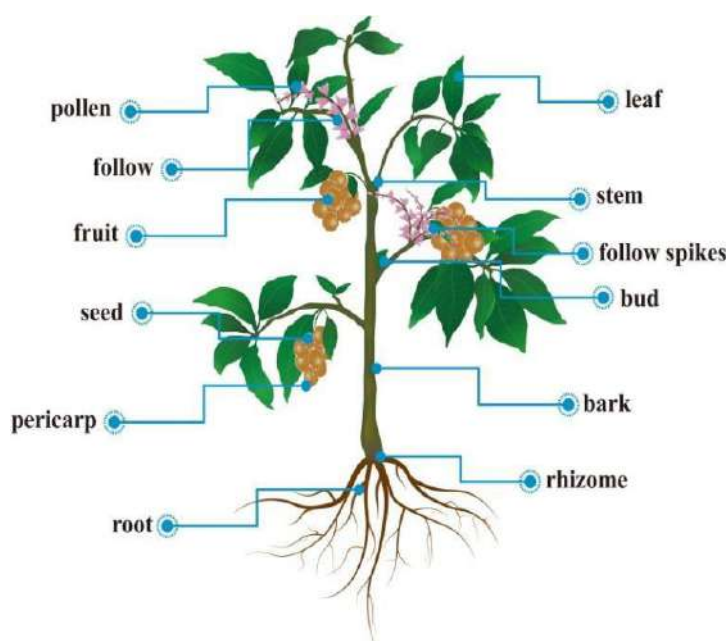


Figure 3.1 - Parts of a plant used for the synthesis of CDs [1]

3.2 SYNTHESIS

In this review report, we take hydrothermal method as a synthesis methodology. Here, the carbon dots were synthesized from five different plant extracts such as Banana juice , Orange juice , *Prosopis juliflora* , Sugarcane bagasse and *Trapa bispinosa* peel.

80 gm of banana was cut in to small and turned into paste with 100 ml of water, then 20 ml of juice was taken with 20 ml of ethanol in a glass bottle plugged with a cotton cork at 150°C over 4 hr. The dark brown product was dissolved in 20 ml of water, then 50 ml of ethanol was added to aqueous filtrate, centrifuge (3000 rpm) for 15 min and the solvent evaporated at room temperature and highly fluorescent carbon dots (600 mg 58% mass yield) are obtained.

In 40 ml of orange juice was mixed with 30 ml ethanol and heated at 120 °C for 150 min in 80 ml Teflon lined stainless steel. The dark brown solution was washed with dichloromethane at it centrifuged at 3000 rpm for 15 min .The excess acetone was added to the upper brown solution and centrifuged at 10000 rpm for 15 min and obtain highly fluorescent carbon dots .

In *Prosopis juliflora*, the plant leaves were washed carefully and soaking in double distilled water for 5 times and drying for 15 days and grounded into a fine powder. 5 gm of plant leaves powder was dispersed in 50 ml of double distilled water and placed in Teflon autoclave at 180°C for 5 hrs. After cooling, natural brown colour solution passed through whatsmann no.1 filter paper and centrifuged at 8000 rpm for 15 min.

In sugarcane bagasse, the sugarcane bagasse pulp was dehydrated in sunlight for 3 days before being ignited at 70°C in air atmosphere to form a carbon matrix. 2 gm of yielded carbon (sugarcane bagasse pulp) and 2 gm of citric acid were homogenously mixed with 25 ml of double distilled water, the aqueous ammonia was added to the precursor and it shift to autoclave at 200°C for 6 hrs. The reactive mixture solution was ultrasonicated for 1 hr and centrifuged for 60 min at 5000 rpm .The supernatant liquid was formed [5].

In *Trapa bispinosa* peel, *Trapa bispinosa* which is soaked in cold water for 30 min. 50 gm of peel was crushed in 500 ml of distilled water and centrifuged to obtain clear pink extract for the synthesis of carbon dots. 100 ml of *Trapa bispinosa* peel extract was refluxed for 2 hrs. at 90°C till the solution becomes greenish brown. The resulting solution was centrifuged at 5000 rpm for 20 min and suspended with 5 ml 1N NaOH to solubilize carbon dots and enhance the fluorescence ability. In order to purify carbon dots, 3 ml of the above

solution was dialyzed against nano pure water for 24 hr. A clear yellowish suspension of carbon dots was observed.



Figure 3.2: The raw materials used in the synthesis processes

3.3 CHARACTERIZATION

3.3.1 U-V Visible Absorption Spectra

In banana juice the optical absorption peak of the carbon dots was observed in the uv region with a maximum absorption at 283 nm and tail extending into the visible range. This is attributed to the $n - \pi^*$ transition of the $C = O$ band and $\pi - \pi^*$ transition of the conjugated $C = C$ band show green colour in the UV.

In orange juice, CD show broad UV absorption at 288 nm which is consistent with carbon nano particles synthesised by carbonisation of chitosan. In the case of coarse particles

the absorption in the visible region intensifies and the shoulder in the UV region becomes more prominent.

The UV visible spectra of *Prosopis juliflora* CDs show a peak value of 270 nm which represents the transition of carbonyl functional groups. The plant extract was observed with 2 peaks at 313 and 271 nm.

The characteristics absorption of *Trapa bispinosa* peel between 450 and 650 nm shows intense green colour under uv light at ($\lambda=365$ nm) [2].

The spectrum of the Sugarcane bagasse showed significant absorptions in the wavelength range of 200 -300 nm.

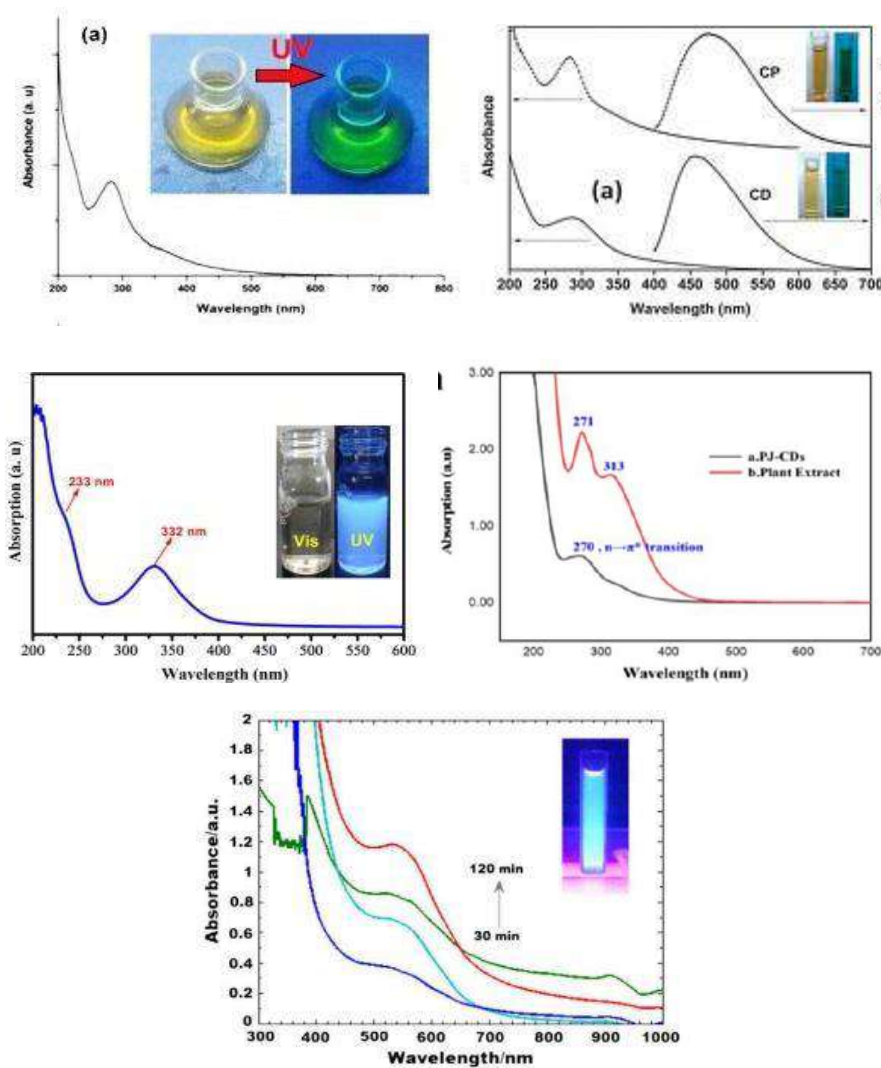


Figure 3.3 UV- Vis spectra of (a) Banana juice (b) orange juice (c) sugarcane bagasse (d) *Prosopis juliflora* (e) *Trapa bispinosa*

3.3.2 XRD Analysis

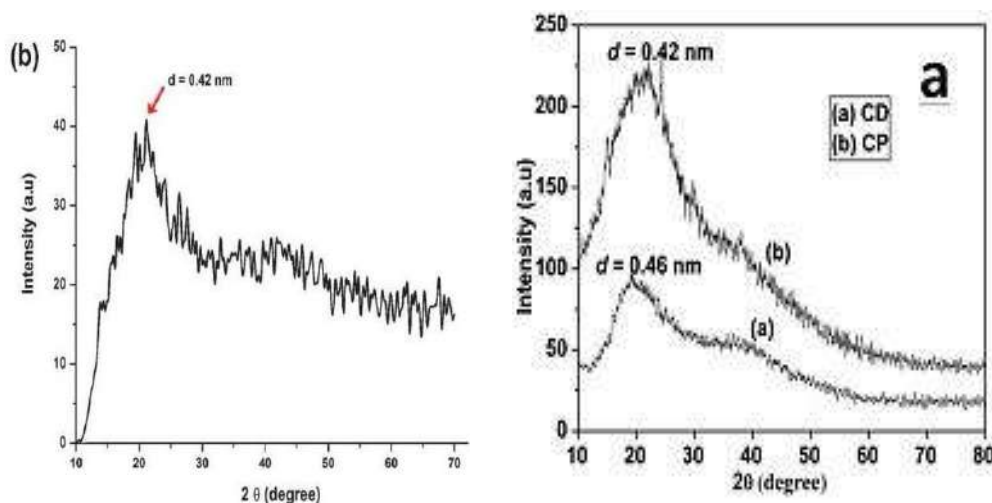
In banana juice, the XRD pattern of the carbon dots shows a broad peak at 21.1° corresponding to the (002) peak. This indicates the interlayer spacing (d) of the carbon dots (0.42 nm) is higher than that of graphitic interlayer spacing (0.33 nm) along with the broadness character. This confirms the **poor crystalline nature of carbon dots**, which is attributed to the generation of more oxygen containing group.

In orange juice, the (002) peak centered at 19.1° in CDs has shifted to 21° in the case of CPs. The corresponding interlayer spacing in graphite (0.34 nm) becomes larger in CDs (0.42 nm) which shift to further layer end in CP (0.46 nm). The increase in d value indicates an increase in **amorphous nature** attributed to the information of more oxygen-containing groups [9].

In *Prosopis juliflora*, the XRD shows a broad peak position at $2\theta = 20.74^\circ$. The PJ-CPs d -spacing value is 23 nm, according to the lattice plane [002]. The nature carbon dots have **amorphous properties** due to C – N, C – C, C = O bonds of CDs [8].

The presence of an intense peak at *Trapa bispinosa* at $2\theta = 24.7^\circ$ and a weak peak at 43.3° are assigned to (002) and (001) diffraction patterns of graphitic carbon respectively [7].

Intensity variation of XRD in sugarcane bagasse is in the range of 10° to 30° (2θ) with a broad peak centered at lower angles.



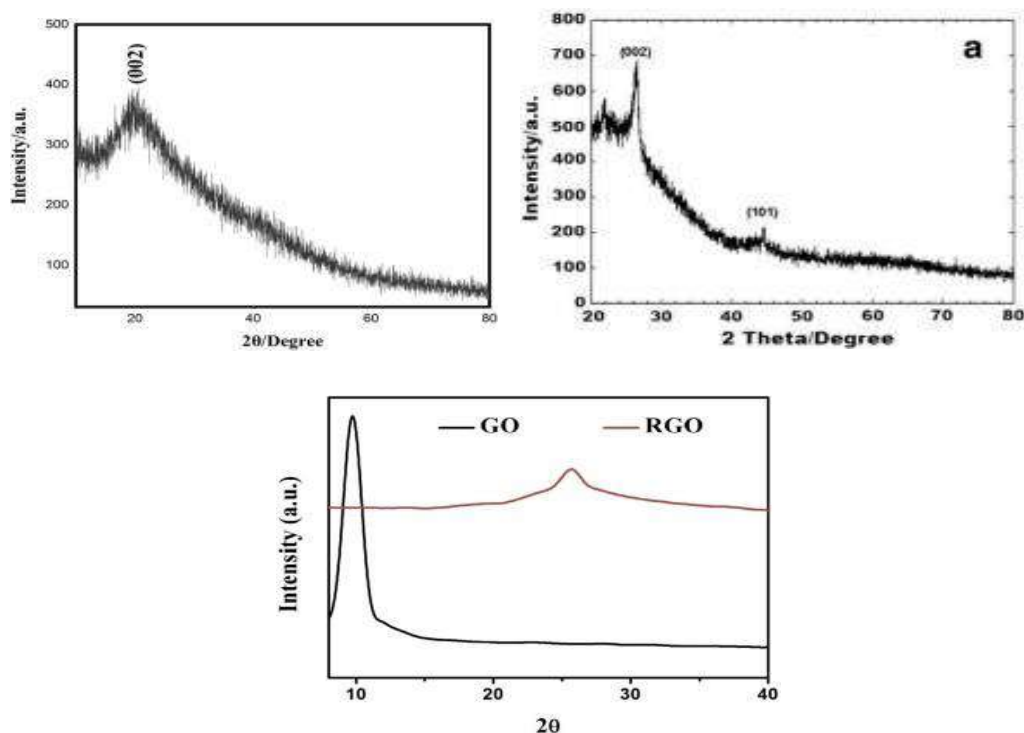


Figure 3.4– The XRD spectra of (a) Banana juice (b) orange juice(c) Prosopis juliflora (d) Trapa bispinosa (e) sugarcane bagasse

3.3.3 FTIR

Figure 3.5(a) shows the FTIR spectra of CDs produced from *Trapa bispinosa* peel, strong absorption at 2925 cm^{-1} & 2860 cm^{-1} and is assigned with to -C-H stretching and a weak absorption at 3394 cm^{-1} -OH stretching, an overtone at 1648 cm^{-1} due to the -C=C- stretching.

Figure 3.5(b) shows the FTIR spectra of CDs produced from sugarcane bagasse, broad peaks around $3200\text{-}3600\text{ cm}^{-1}$ (stretching vibration) and $1600\text{-}1700\text{ cm}^{-1}$ (bending vibration) for -OH, peaks around $(1700\text{-}1750)\text{ cm}^{-1}$ for -C=O, peaks around $1700\text{-}1750\text{ cm}^{-1}$ (stretching vibration) and $1300\text{-}1400\text{ cm}^{-1}$ (bending vibration) for -COOH, peaks around $1550\text{-}1650\text{ cm}^{-1}$ for -NH₂. Peaks corresponding to C-H stretching and bending vibrations in the aliphatic and aromatic regions around $2800\text{-}3000\text{ cm}^{-1}$ and $(3000\text{-}3100)\text{ cm}^{-1}$, respectively) may be seen [5].

Figure 3.5(c) shows the FTIR spectra of CDs produced from banana juice, Stretching frequencies at $3492, 2935, 1730, 1625, 1422, 1264$ and 918 cm^{-1} indicating the presence of -OH, -C-H, C=O, C=C, C-O-C & an epoxy ring.

Figure 3.5(e) shows the FTIR spectra of CDs produced from orange juice, The high-resolution scan of the C1s region shows carbons present in five different chemical environments corresponding to sp^2 (C=C) at 284.1 eV , sp^3 (C-C and C-H) at 285.5 eV , C-

OH/C–O–C at 285.7 eV, C=O at 288 eV and –COOH at 289.3 eV. The presence of C=C, C–O, COOH bonds indicates that the CDs are functionalized with hydroxyl, epoxy, carbonyl, and carboxylic acid groups which is also evidenced by FTIR.

Figure 3.5(d) shows the FTIR spectra of CDs produced from *Prosopis juliflora*. The broad band absorption peaks at 3391 cm^{-1} is due to O–H stretching, 918 cm^{-1} is due to the C–H of alkanes. The peaks at 1604 cm^{-1} and 1400 cm^{-1} correspond to the absorption peaks attributed to C=C and O–H stretching vibrations, respectively. Additional peaks at 1079 cm^{-1} signifies C–N stretching vibrations. The presence of the hydroxyl group (O–H) is critical in enhancing the antibacterial activity of the prepared PJ-CD [10]

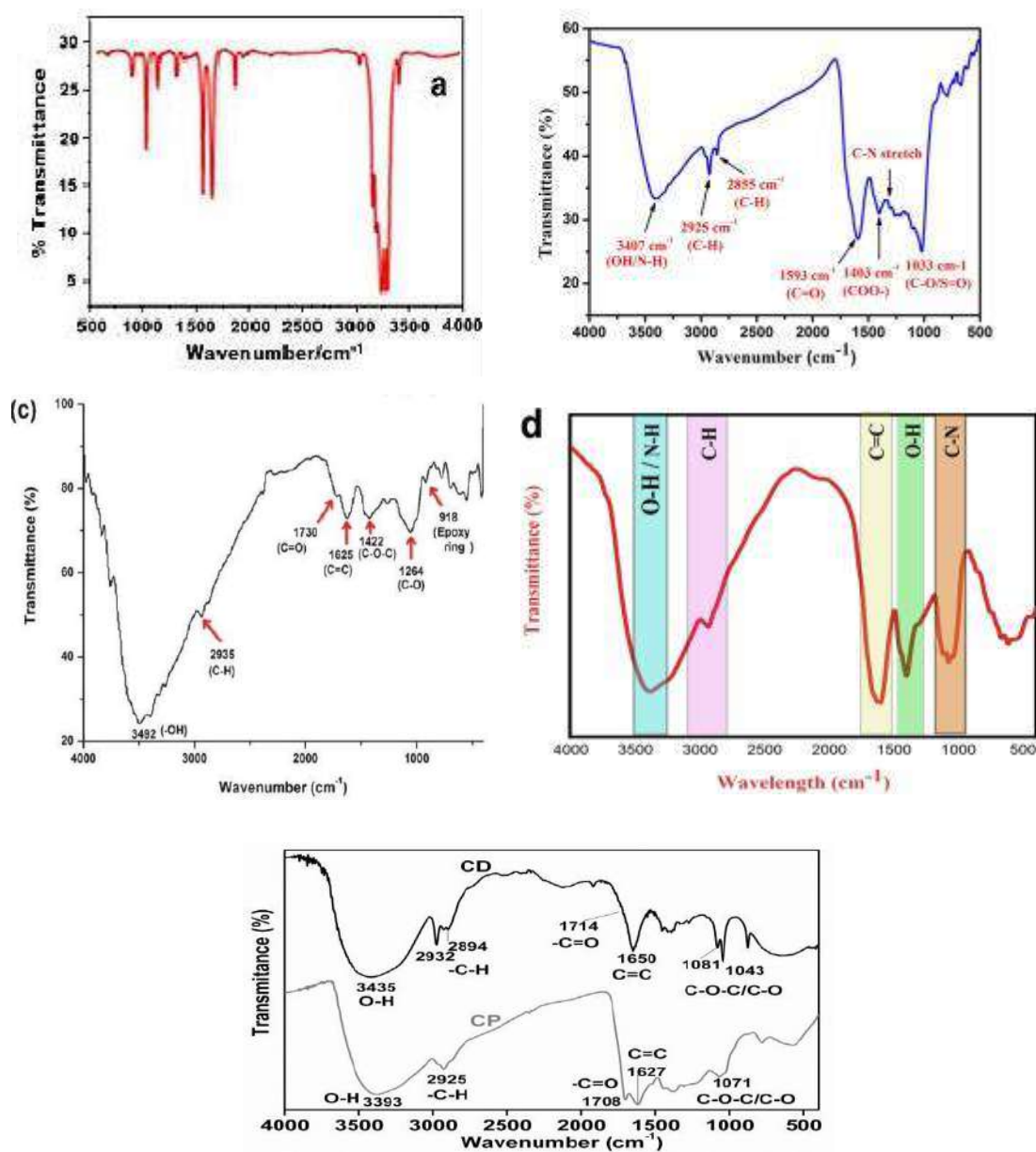


Figure 3.5: FTIR spectra of (a) *Trapa bispinosa* (b) sugarcane bagasse (c) Banana juice (d) *Prosopis juliflora* (e) orange juice

3.3.4 HRTEM & TEM

In case of the *Trapa bispinosa*, from the HRTEM we observe spherical dots ranging from 5 to 10 nm.

In the case of sugarcane bagasse, The TEM images were nanodots of average size 5.18 nm & monodisperse luminescent CD of average diameter 2.94 nm. Thus the formation of the CDs of average size 3 nm was confirmed [5].

TEM image of banana juice it reveals that the carbon dots are spherical with a narrow size distribution ranging between 1.5 to 4.5 nm.

For the orange juice, HRTEM images reveal that the CDs are spherical, monodisperse and have a narrow size distribution between 1.5 and 4.5 nm with maximum population at 2.5 nm. And finally from the *Prosopis juliflora*, we observe that particles were spherical in shape. The diffraction pattern presented indicates the **amorphous nature** of the synthesized PJ-CDs which showed that the majority of PJ-CDs were in range of 5-12 nm with average size of 8 nm.[6]

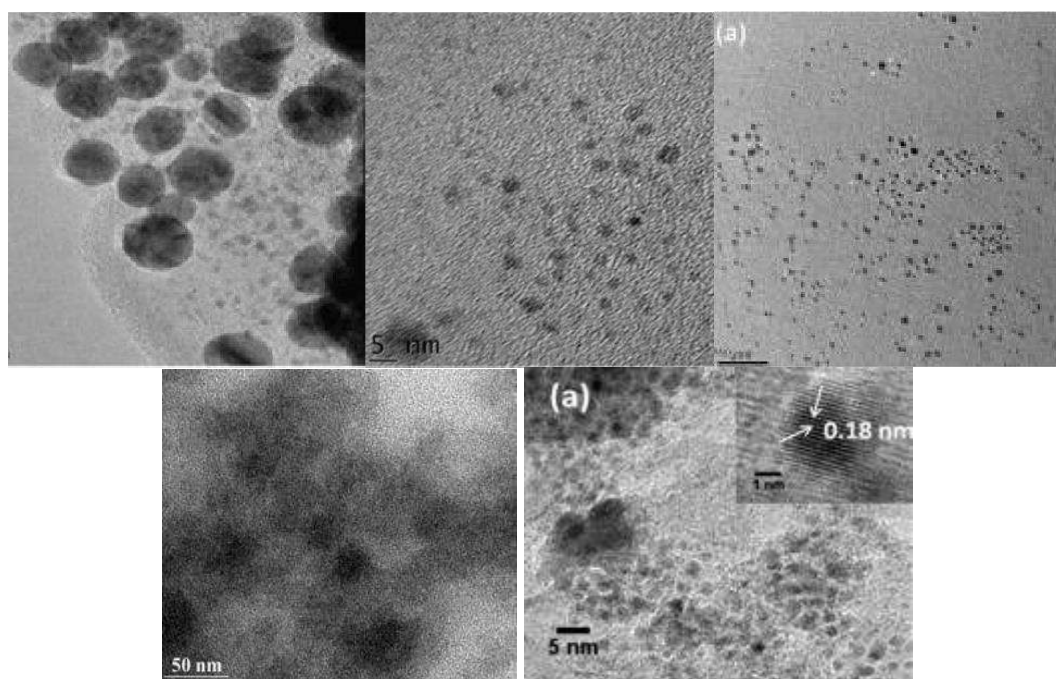
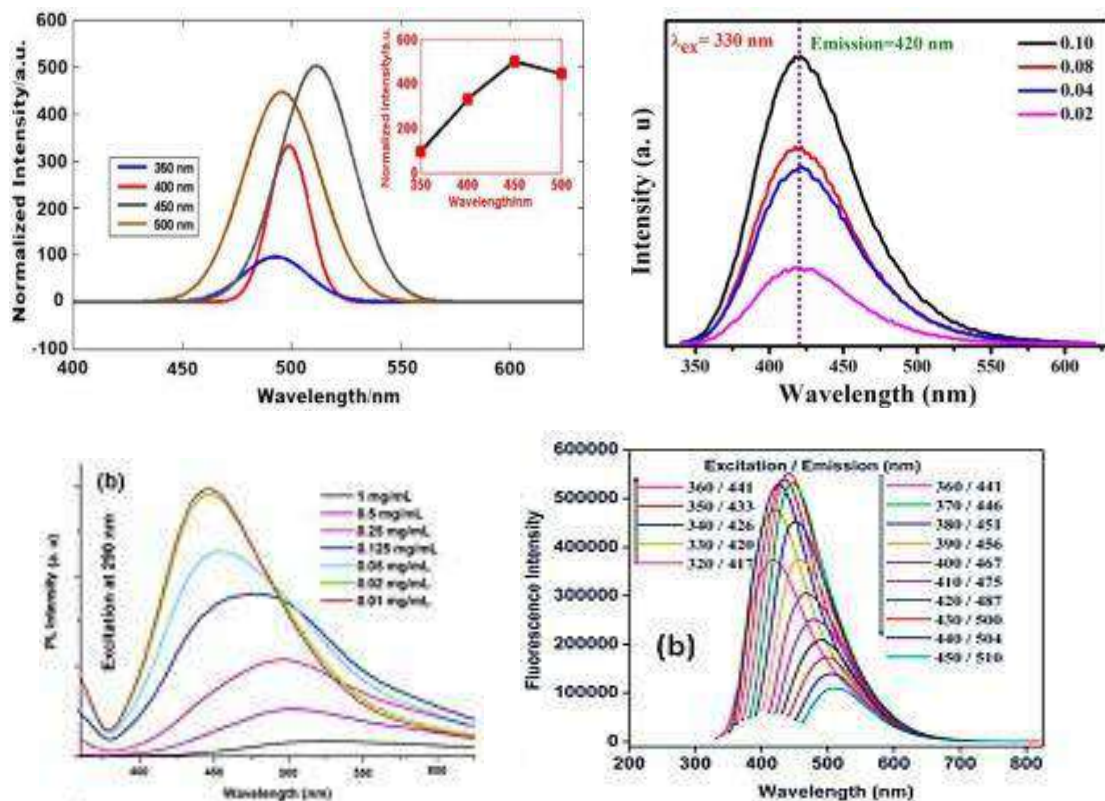


Figure 3.6- HRTEM & TEM images of (a) *Trapa bispinosa* (b) sugarcane bagasse (c) Banana juice (d) *Prosopis juliflora* (e) orange juice

3.3.5 Photoluminescence

Trapa bispinosa Shows photoluminescent behavior as shown in the figure 3.7(a), now for sugarcane bagasse, the hydrothermal time on enhancing the PL Intensity, The maximum emission Spectra at 420nm under 330 nm excitation Sufficient to improve PL intensity The effect of the amount of NaOH enhancing the PL intensity in the absence of NaOH, PL of S-B was only changed from 4.4 to 52-5 au fig (b) [5]. For banana juice, the excitation occurs at 290 nm. The PL intensity is also dependent upon the excitation wavelength (340-420 nm). The strong PL emission peak located at 460 nm was observed with an excitation wavelength of 360 nm. A strong PL intensity was observed in the PH range of (4-8). From the orange juice, PL mechanism is controlled by both size effect and surface defect. Another interesting phenomenon here is the pH dependent PL behavior. PL intensity decreased at very high pH and slightly decreased at low pH, but remained almost unchanged at pH 4.8–8.7, from *Prosopis juliflora*, the fluorescence study was carried out in wavelength ranges between 395 and 480 nm and shows emission peak at 540 nm around an excitation wavelength of 480 nm. Fig (e)



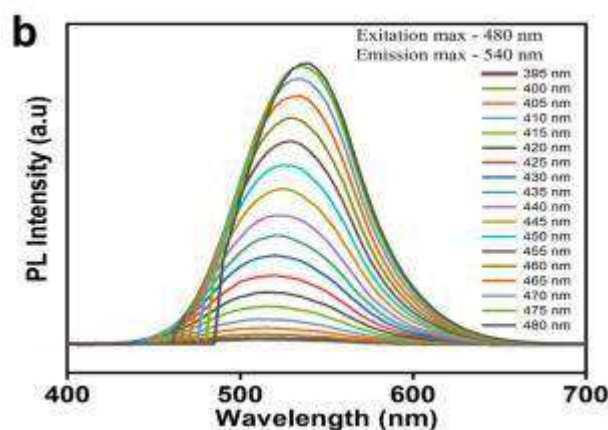


Figure 3.7– The PL Spectra of (a) *Trapa bispinosa* (b) sugarcane bagasse (c) Banana juice (d) orange juice (e) *Prosopis juliflora*

3.4 APPLICATIONS

The CDs synthesized from *Trapa bispinosa* were found to be exceptionally biocompatible against MDCK (Madin-Darby canine kidney (MDCK) cells are a model mammalian cell line used in biomedical research) cells. The obtained luminescent carbon dot derived from sugarcane bagasse can be used to remove Cd (II) ($Q = 24.47 \text{ mg/g}$), and it has much potential to remove heavy metals. This environmental friendly reduced graphene oxide has promise as an adsorbent for the removal of pollutants. The antibacterial potentially PJ-CDs can also be useful in providing sterile environment for bio-image and biomedical applications. The CDs obtained from orange juice can serve as a potential substitute for organic dyes or semiconductor QDs in bioimaging. The bio-based and water soluble highly luminescent carbon dots obtained from banana juice can potentially be applied in solution state optoelectronics.

3.5 COMPARISON

Table 3.1 shows the comparison of CDs from all five selected papers.

Properties	<i>Trapa bispinosa</i>	Sugarcane bagasse	Banana juice	Orange juice	<i>Prosopis juliflora</i>
Synthesis method	Hydrothermal method	Hydrothermal method	Hydrothermal method	Hydrothermal method	Hydrothermal method
Economic importance	Cheap price and high availability	Cheap price and high availability	Cheap price and high availability	Cheap price and high availability	Cheap price and high availability

End product	Forms luminescent & fluorescent carbon dots	Forms luminescent & fluorescent carbon dots	Forms luminescent & fluorescent carbon dots	Forms luminescent & fluorescent carbon dots	Forms luminescent & fluorescent carbon dots
Temperature	90°C for 2 hours	200°C for 6 hours	150°C for 4 hours	120°C for 150 minutes	180°C for 5 hours
UV Visible absorption spectra	Represents characteristic absorption between 450 & 650nm shows intense green colour under UV light at ($\lambda=365\text{nm}$)	The spectrum of the S-B showed significant absorptions in wavelength range of 200-300 nm rather than S-A.	The optical absorption peak of the carbon dot was observed in the UV region with a maximum absorption at 283 nm & a tail extending into visible range	CDs show broad UV absorption at 288nm which consistent with CNPs synthesized by carbonization of chitosan. In the coarse particles the absorption in the visible region intensifies and the shoulder in the uv region become more important .the size dependent absorption is associated with at the red shift in the emission spectra. At a fixed $\lambda_{\text{ex}} = 390 \text{ nm}$, CDs show an emission peak at 455 nm while the corresponding peak for CPs appears at 474 nm	The UV-visible spectra of PJ-CDs shows a peak value of 270 nm which represents the $n-\pi^*$ transition of carbonyl functional groups. Whereas the plant extract observed with two peaks at 313 and 271 nm confirms to previous report. In a previous report, a water-soluble CDs produced from citric acid and Curcumin with effective antibacterial and anti - biofilm activities showed the UV-Vis spectra peak value of 280 nm which stands for $n-\pi^*$ transitions
Revolutions per minute (rpm)	5000	5000	3000.	3000	8000
Solubility	Shows excellent water solubility	Shows excellent water solubility	Shows excellent water solubility	Shows excellent water solubility	Shows excellent water solubility

TEM & HRTEM	Spherical dots ranging from 5 to 10 nm.	The TEM image of S-A were nanodots of average size 5.18 nm & monodisperse luminescent CD of average diameter 2.94 nm	The formation of the CDs of average size 3nm was confirmed. The TEM image clearly reveal that the carbon dots are spherical shape with a narrow size distribution ranging between 1.5 nm to 4.5 nm	HRTEM images clearly reveal that the CDs are spherical, monodisperse and have a narrow size distribution between 1.5 and 4.5 nm with maximum population at 2.5 nm.	The particles were spherical in shape, and. The diffraction pattern presented indicates the amorphous nature of the synthesized PJ-CDs Which showed that the majority of PJ-CDs were in range of 5-12 nm with average size of 8 nm
XRD analysis	Intense peak at $2\theta = 24.7^\circ$ & weak peak at $2\theta = 43.3^\circ$	Intensity variation in the range of approximately 10° to 30° (2θ), with a broad peak centered at lower angles	Broad peak at 21.1°	The peak centered at 19.11°	Shows a broad peak position at $2\theta = 20.74^\circ$
FTIR	Strong absorption at 2925 cm^{-1} & 2860 cm^{-1} and is assigned with to -C-H stretching and a weak absorption at 3394 cm^{-1} -OH stretching, an overtone at 1648 cm^{-1} due to the -C=C-stretching	Broad peaks around $3200\text{-}3600\text{ cm}^{-1}$ (stretching vibration) and $1600\text{-}1700\text{ cm}^{-1}$ (bending vibration) for -OH, peaks around $1700\text{-}1750\text{ cm}^{-1}$ for -C=O, peaks around $1700\text{-}1750\text{ cm}^{-1}$ (stretching vibration) and $1300\text{-}1400\text{ cm}^{-1}$ (bending vibration) for -COOH, peaks around $1550\text{-}1650\text{ cm}^{-1}$ for -NH ₂ Peaks corresponding to C-H stretching and bending vibrations in the aliphatic and aromatic regions (around $2800\text{-}3000\text{ cm}^{-1}$ and $3000\text{-}3100\text{ cm}^{-1}$, respectively)	Stretching frequencies at 3492, 2935, 1730, 1625, 1422, 1264 and 918 cm^{-1} indicating the presence of -OH, -C-H, C=O, C=C, C-O-C & an epoxy ring	The high resolution scan of the C1 s region shows carbons present in five different chemical environments corresponding to sp^2 (C=C) at 284.1 eV, sp^3 (C-C and C-H) at 285.5 eV, C-OH/C-O-C at 285.7 eV, C=O at 288 eV and -COOH at 289.3 eV. The presence of C=C, C-O, COOH bonds clearly indicates that the CDs are functionalized with hydroxyl, epoxy, carbonyl, and carboxylic acid groups which is	The broad band absorption peaks at 3391 cm^{-1} is due to O-H stretching, 2918 cm^{-1} is due to the C-H of alkanes The peaks at 1604 cm^{-1} and, 1400 cm^{-1} correspond to the absorption peaks attributed to C=C and O-H stretching vibrations, respectively. Additional peaks at 1079 cm^{-1} signifies C-N stretching vibrations. The presence of the hydroxyl group (O-H) is critical in enhancing the antibacterial activity of the prepared

		may be seen		also evidenced by FTIR	PJCDs
Photoluminescence	Shows Photoluminescent behavior	The hydrothermal time on enhancing the PL Intensity of S-A ,The maximum emission Spectra at 420nm under 330 nm excitation wavelength Sufficient to improve PL intensity. The effect of amount of NaOH En enhancing the PL intensity in the absence of NaOH, PL of S-B was only changed from 4.4 to 52-5 au	The intensity depends upon the concentration of CDs. The excitation occur at 290 nm .the PL intensity is also dependent upon the excitation wavelength(340-420nm).The strong PL emission peak located at 460nm was observed with an excitation wavelength of 360nm.A strong PL intensity was observed in the PH range of (4-8)	PL mechanism is controlled by both size effect and surface defect. Another interesting phenomenon here is the pH dependent PL behavior. PL intensity decreased at very high pH and slightly decreased at low pH, but remained almost unchanged at pH 4.8–8.7	The fluorescence study was carried out in wavelength ranges between 395 and 480 nm and shows emission peak at 540 nm around an excitation wavelength of 480 nm.
Quantum yield	The maximum no of CDs are excited at the 450 nm. The QY at 450nm is 1.2%	Fluorescence of S-A was very weak with the quantum yield of 0.2% under a 33000 excitation wavelength. The S-B had strong fluorescence The quantum yield was 4.4% with a maximum emission spectrum at 420 nm under 330 nm.	Quantum yield of carbon dots in aqueous solution as measured at an excitation wavelength of 360 nm and was found to be 8.95%	Quantum yield of CD is 26%. This value is appreciably higher QY of carbon nanoparticles synthesized by other methods	The absolute photoluminescence Quantum yield of CD is 7.88 %

3.6 CONCLUSION

This review report provides an overview of the synthesis of carbon dots from five different plant extracts like Banana juice, Orange juice, *Prosopis juliflora*, Sugarcane bagasse, and *Trapa bispinosa* via green synthesis approaches. Understanding the properties and synthesis methods of carbon dots is essential for harnessing their full potential, and diverse technological and biomedical applications. These CDs were prepared using the simple hydrothermal method. The absorption spectra of the raw precursor extracted from the

different plant derivatives are mainly in the UV region of the electromagnetic spectrum. They are all highly soluble in water. Morphological analysis shows that the synthesized CDs are ~ 4 nm in diameter. All the CDs show a poor crystalline nature. Most of the CDs possess almost similar functional groups. This may be because of the bio-origin of the CDs. The Quantum yield of the orange juice is very high compared to all other CDs. This high quantum efficiency is due to the pH-dependent behavior of the CDs. Also, the high luminescent property of CDs reveals a pH ranging from 4 to 8.5. This pH range is also very important for the biomedical application of CDs as sensors.

REFERENCES

1. Luo, WK., Zhang, LL., Yang, ZY. et al. Herbal medicine derived carbon dots: synthesis and applications in therapeutics, bioimaging and sensing. *J Nanobiotechnol* 19, 320 (2021)
2. S.N. Baker, G.A. Baker, *Angew. Chem. Int.* 49 (2010) 6726–6744
3. Y. Yang, J. Cui, M. Zheng, C. Hu, S. Tan, Y. Xiao, Q. Yang and Y. Liu, *Chem. Commun.*, 2012, 48, 380–382.
4. . Lu, F. et al. Water-solvable carbon dots derived from curcumin and citric acid with enhanced broad-spectrum antibacterial and antibiofilm activity. *Mater. Today Commun.* 26, 102000 (2021)
5. Raghavan, N., Thangavel, S., Sivalingam, Y., Venugopal, G., 2018. Investigation of photocatalytic performances of sulfur based reduced graphene oxide-TiO₂ nanohybrids. *Appl. Surf. Sci.*
6. Sivanandhan, M. et al. Facile approach for green synthesis of fluorescent carbon dots from *Manihot esculenta* and their potential applications as sensor and bio-imaging agents. *Inorg. Chem. Commun.* 137, 109219 (2022)
7. D.Y. Pan, J.C. Zhang, W.Q. Shen, Z.W. Zhang, Y.G. Fang, M.H. Wu, *New J. Chem.* 34 (2010) 591–593.
8. Pandey, S. C., Kumar, A. & Sahu, S. K. Single step green synthesis of carbon dots from *Murraya koenigii* leaves; a unique turn-of fluorescent contrivance for selective sensing of Cd (II) ion. *J. Photochem. Photobiol. A* 400, 112620 (2020)
9. J. Peng, W. Gao, B. K. Gupta, Z. Liu, R. Romero-Aburto, L. Ge, Li Song, L. B. Alemany, X. Zhan, G. Gao, S. A. Vithayathil, B. A. Kaiparettu, A. A. Marti, T. Hayashi, J. Zhu and P. M. Ajayan, *Nano Lett.*, 2012, 12, 844–849.
10. Pandiyan, S. et al. Biocompatible carbon quantum dots derived from sugarcane industrial wastes for effective nonlinear optical behavior and antimicrobial activity applications. *ACS Omega* 47, 30363–72 (2020).

SYNTHESIS OF SILVER NANOPARTICLES USING DIFFERENT REDUCTION APPROACHES: A COMPARATIVE REVIEW

A project report

Submitted to St. John's College, Anchal for the requirement of

Bachelor of Science in Physics

By

VISAL MS (23021138004)

PRATHYUSH SH (23021138012)

VIGNESH NARAYANAN (23021138017)

Under the guidance of

Dr. JIJI S.G.

Assistant Professor

St. John's College, Anchal, Kollam




CERTIFICATE

This is to certify that the project entitled "SYNTHESIS OF SILVER NANOPARTICLES USING DIFFERENT REDUCTION APPROACHES :A COMPARATIVE REVIEW " submitted by VISAL MS (23021138004), PRATHYUSH SH (23021138012), VIGNESH NARAYANAN (23021138017) carried out in the Department of Physics, St. John's College, Anchal for the partial fulfillment for the degree program Bachelor of Science in Physics under the guidance and supervision of Dr. JIJI S.G. , Assistant Professor, Department of Physics, St. John's College, Anchal, Kollam during the academic year of 2023-2024.

This work is original and has not been submitted earlier for the award of any other degree.

Place: Anchal

Date: May 2024


Head of the Department:
Dr BENZON K B
HOD & Assistant Professor
Department of Physics
St John's College, Anchal- 691 001

Examiners:

i.


17/5/24

ii.


17/5/24



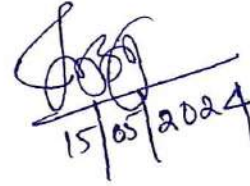
CERTIFICATE

This is to certify that the project entitled "SYNTHESIS OF SILVER NANOPARTICLES USING DIFFERENT REDUCTION APPROACHES : A COMPARATIVE REVIEW" submitted by VISAL MS (23021138004), PRATHYUSH SH (23021138012), VIGNESH NARAYANAN (23021138017) carried out in the Department of Physics, St. John's College, Anchal for the partial fulfillment for the degree program Bachelor of Science in Physics under the guidance and supervision of Dr. JJI S.G., Assistant Professor, Department of Physics, St. John's College, Anchal, Kollam during the academic year of 2023-2024.

This work is original and has not been submitted earlier for the award of any other degree.

Place: Anchal

Date: 15th May 2024



Dr. JJI S.G.
Assistant Professor
Department of Physics
St John's College
Anchal, Kollam - 691306

ACKNOWLEDGEMENT

First and foremost, we bow down before Lord almighty for his blessings and care in completing our project work and throughout our life till this very second.

It is with great pleasure that we **VISAL MS** (23021138004), **PRATHYUSH SH** (23021138012), **VIGNESH NARAYANAN** (23021138017) present the project entitled **“SYNTHESIS OF SILVER NANOPARTICLES USING DIFFERENT REDUCTION APPROACHES :A COMPARATIVE REVIEW”** .

We would also like to express our sincere and special gratitude to **Dr. JIJI S.G**, Assistant Professor, for her guidance, tactful advice and immense encouragement that made us complete the project.

We record our sincere thanks to **Dr. Benzon K.B**, Assistant Professor & Head of Department of Physics, St .John’s College, Anchal, Kollam for his valuable support.

We owe our sincere thanks to our parents who supported and encouraged us during this work. Friends are the treasures to us and it is difficult to overstate our thanks to all our friends and colleagues. We wish to extend our warmest thanks to our classmates for their support. We feel delighted to express our wholehearted gratitude to all those who gave their helping hands in completing our project successfully.



ST. JOHN'S COLLGE

ANCHAL

Project report

Submitted to the University of Kerala for the requirement of the degree of Bachelor of Science in Physics

“Literature review of spectroscopic and computational study of derivatives of imidazole”

Submitted By

KAVYA KRISHNA : 23021138002

MEGHA RAJ : 23021138003

SNEHA NADH L : 23021138013

Under the supervision of

Dr . Benzon K B

Assistant Professor & Head

Department of physics

St . John's college , Anchal

2021-24

CERTIFICATE

Dr Benzon K B
Head of the Department
Assistant Professor
St John's college
Anchal , Kollam

This is to certify that the **“Literature review of spectroscopic and computational study of derivatives of imidazole”** submitted by **Kavyakrishna (23021138002) , Megha Raj (23021138003) and Sneha Nadh L (23021138013)**, in partial fulfillment of the requirement for the award of Degree of Bachelor of Science in Physics is based on their original work under my guidance .It is further certified .

Anchal

Signature :

Date :

DECLARATION

We hereby declare that the “**Literature review of spectroscopic and computational study of derivatives of imidazole**” is a bonafide work submitted to the University of Kerala in partial fulfillment of the requirement for the award of degree of Bachelor of Science in Physics under the guidance of **Dr Benzon K B**, Assistant Professor & Head of the Department of Physics, St. John’s College, Anchal, Kollam. This has not been previously submitted for the award of any degree, diploma, associate ship and fellowship or other similar title to any candidates of any universities.

Kavya Krishna (23021138002)

Megha Raj (23021138003)

Sneha Nadh L (23021138013)

Anchal

Date :

ACKNOWLEDGEMENT

Our project would have not been a success without the grace of the almighty God . On the successful completion of the project work, we would like to give our sincere gratitude to all those who assisted us directly and indirectly .

We take this opportunity to express our deepest sense of gratitude to our guide **Dr Benzon K B**, Assistant professor & Head of Department of Physics, St. John's College Anchal , Kollam, for this valuable guidance throughout this project work .

We sincerely acknowledge our gratitude to the principal **Dr Nisha Thomas , St John's College Anchal, Kollam** for having provided the facilities to complete this work. We sincerely thank the authorities of St. John's College Anchal, Kollam for allowing us to carry out our project work in their prestigious organization . We also extend our thanks to all other faculty members and fellow students for their valuable assistance during the entire period of this project.

Kavya Krishna (23021138002)

Megha Raj (23021138003)

Sneha Nadh L (23021138013)

Anchal

Date :

LIST OF CONTENTS

NO	CONTENTS	PAGE NO
1	INTRODUCTION	8-11
2	DETAILED EXPLANATION OF SELECTED DERIVATIVES	13-50
3	COMPARITIVE STUDY AND CONCLUSION	52-56
4	REFERENCE	57-61

ABSTRACT

Spectroscopy deals with the interaction between radiation and matter . It study the absorption and emission spectrum of the matter. This can be achieved only because the atoms and molecules exist only in some certain allowed energy states . when a energy is supplied to the molecule it get excited and jumps to higher energy level . It jumps to the higher energy level by absorbing or releasing radiation . every compound have a unique spectrum because each compound interact differently to radiation . Through spectroscopic study the structure and constituent of the compound . Not only spectroscopic study but also computational study is also used to obtain more information about the compound . Computation study obtain information about a compound using different software . Though different methods are used the result will be the same . Both spectroscopic study and computational study are considered as non destructive study because the sample is not destroyed during the study . So this method are widely used in forensic and medical fields . The structure , constituent particle, and its reactivity , interaction can be predicted using this method . So these methods have a greater future importance , some applications are the we can predict drug efficiency , toxicity , and interaction using computational and spectroscopic studied , it can also used for environmental , agricultural , biomedical researches to draw more accurate information .

In our literature review we analysed many derivatives of imidazole . some derivatives were spectroscopically analysed and some of the were computationally analysed . In both of the cases the conclusion are the same . Through this review we are able to understand the interaction of imidazole compounds , its electronic structure , global hardness . imidazole is a compound with many applications. It is widely used as antifungal and antibacterial agents , corrosion inhibitor , catalyst in organic compound , as a flavouring agent in food industry , it is also used in advanced batteries for the storage of energy . So it important to understand the property of imidazole more accurately . Through these study the properties and its interaction with different radiations are studied . This will help to understand more about imidazole and its derivatives and its future applications .

CHAPTER 1
INTRODUCTION

INTRODUCTION

1. SPECTROSCOPY

Spectroscopy records the emission and absorption of light or other radiation by the matter and it also provide chemical, physical and electrical structure of numerous molecule or particle that are under the examination . In spectroscopy we study the relationship between light and matter . Through spectroscopy many quantities of a sample can be studied .Basically spectroscopy is a study of absorption and emission of light and other radiation by matter itself. It's done by splitting radiation into its constituent wavelength by grating and is fed into CCD's. Thus 2D spectrum is extracted in the digital format and is manipulated to form 2D Spectra which contain useful data. We know the fact that atoms and molecules exist only in a certain energy level which is allowed. When the Energy is supplied to the atoms and molecule it is excited and Radiation may be emitted or absorbed. The sample is excited with a known force of energy and the expected energy transition is measured. Thus the detail about the sample is obtained because the interaction with light and matter is unique for every chemical compound.

1.1. PRINCIPLE OF SPECTROSCOPY

Each molecule have a unique atomic or molecular constitution . So it shows a variety of energy absorption at different frequencies . This is the basic principle of Spectroscopy . A molecule or atom shows different energy in different energy state . The energy difference between the energy of two states determines the frequency of light radiation absorbed by the substance . The absorption produces an absorption spectrum . When a sufficient energy photon interact with the electron , it absorbs the energy and moves to an excited state . This causes the production of absorption spectrum . Spectroscopic techniques are effective for both quantitative and qualitative analysis . It normally use specialized equipment called spectrometer to record the wave length of the electromagnetic radiation to get information about the structure and other properties of the sample. A spectrometer mainly consist of a radiation source detection source and a analysis equipment . Spectroscopic techniques involves passing a beam of energy through a sample and recording and analyzing the result through a sample and recording and analyzing the result to determine the identity , composition , and quantities of the components of the sample .There are a number of spectroscopic techniques are present in now a days . Different spectroscopic techniques use different wavelength of the electromagnetic spectrum as energy source . The methods changes according with the type of radiation matter interaction .

1.2. TYPES OF SPECTROSCOPY

1.2.1. Infrared spectroscopy (IR Spectroscopy)

IR Spectroscopy studies the vibrational and rotational modes of a molecule . Because the energy of the photon in infrared region of an electromagnetic spectrum matches the molecular vibration .

IR Spectrometer records the specific frequencies absorbed by the sample in the infrared region . The absorption spectrum thus obtained can be used to determine the different types of chemical bonds and different types of molecular structure present in the sample . IR Spectroscopy works on the absorption spectroscopy . High chemical specificity and wide applicability are the advantages of IR Spectroscopy .

1.2.2. Raman Spectroscopy

Raman spectroscopy measures the inelastic scattering of light .When light hit a molecule it scatters in different direction and majority of the scattered light have the same wavelength as that of the incident light this is called Rayleigh scattering but some have different wave length than that of the incident light this scattering is called Raman scattering . Raman spectrum analyse the changed wavelength and the Raman spectrum shows the wavelength of light that shifted in frequency .This provides the information about the molecular structure and bonds .

- Comparison between Raman spectroscopy and IR Spectroscopy
 - Both IR and Raman spectra can be used to identify the characteristics of the molecule , chemical bonding ,functional groups and molecular interaction .
 - IR spectra can only be used for organic compound while Raman spectra is used for inorganic compound and biomolecules
 - IR spectroscopy requires a sample in solid or liquid state but Raman spectroscopy analyse samples in all three states .

1.2.3. Nuclear Magnetic Resonance Spectroscopy (NMR Spectroscopy)

NMR Spectroscopy measures the magnetic field occur about the nuclei of an atom The nuclei of the atom excited by using Radio waves . The sensitive radio receivers detect the vibration of the nuclei when it starts to vibrate .

NMR Spectroscopy gives the detailed information about the structure and reaction state of the molecule . So it is an exact method for determining the composition of the sample .

1.3. COMPUTATIONAL METHOD

Not only spectroscopic method computational method is also used to study about an atom or molecule. Computational physics is the study of scientific problems using computational method . It combines Physics, Applied Mathematics , and computer science to develop scientific solutions for complex problems . Computational physics combines the area of theory and experimentation in a theory and experimentation in a traditional scientific investigation.

Computational Physics can be used to stimulate and analyse spectroscopic data ,helping to interpret experiment Results and understand the behavior of compound at a molecular level .Different computational method are used to study about the sample.

1.3.1. Molecular Docking

Molecular docking is a computational simulation through which it is possible to predict interaction between two structures, which may be between a protein and a ligand or between two proteins .it is the study of how two or more molecule structure fit together The ability of a protein and nucleic acid to interact with small molecules to form a supra molecular complex play a major role in the dynamics of the protein , which may enhance or inhibit its biological function . The behavior of small molecule in the binding pocket of target protein can be described by molecular docking. Based on the type of ligand docking can be classified as

- Protein-small molecule docking
- Protein- nucleic acid docking
- Protein-protein docking

Each docking process is different but they all share common features involve ligand and receptor, sampling, and scoring. Sampling involve conformational and orientational location of the ligand within the constraints of the receptor-site binding. A scoring function selects the best ligand conformation, orientation and translation and classifies ligand in rank order. Docking is widely used to suggest the binding modes of protein inhibitors. Most docking algorithms are able to create a large number of possible structure. Thus the docking problem is the generation and evaluation of possible structures of inter-molecular complexes. Various algorithms are developed to solve this problem. Among them the simplest algorithm treats the two molecules as rigid body and explore only the six degrees of freedom .In early algorithm for small molecule ligands into the binging sides of protein and DNA used this approximation. The ideal docking method allows the ligand and receptor to explore their conformational degrees of freedom. Molecular docking can predict the binging mode of a single active molecule.

1.3.2. Density Function Theory (DFT)

Density function theory is a very popular quantum mechanical technique used to calculate the electronic structure of material . This theory states that the ground state property of a system can be determined by its electron density than its wave number . It is more convenient method than any other quantum mechanical technique .Through DFT technique we calculate electronic structure, geometry, vibrational frequency and thermodynamic property of a material. DFT technique is widely used because its computational efficiency, ability to handle large system, and its accuracy for ground state property .but DFT technique is less accurate for excited state system .

1.3.3. Molecular Electrostatic Potential (MEP)

MEP measures the electrostatic potential of molecule with its distribution of electric charge around the molecule. MEP represents a 3D surface where electrostatic potential have a specific value .MEP is useful in identifying the region of high and low electrostatic potential, distribution of electric charge around molecule; it determines the shape and size of the molecule. MEP is also used in design new molecule, to understand the binding of molecule with other protein

1.3.4. Frontier molecular orbital analysis (FMO)

It helps to understand the reactivity of the molecule. It focuses on the HOMO and LUMO orbitals. HOMO means highest occupied molecular orbital and LUMO means lowest occupied molecular orbital. HOMO is considered as an electron donating and LUMO is electron accepting molecular orbital. Chemical reactions and resonance can be explained by the interaction between a filled HOMO and an empty LUMO on one or mole molecule .FMO theory uses this idea to explain the structure of molecule. HOMO and LUMO can determine the molecular reactivity and also it can express the ionization energy and electron affinity. By understanding the FMO one can predict and design the outcome of a chemical reaction.

1.3.5. Non Linear Optical property (NLO)

Nonlinear optical property deals with the behavior of light in nonlinear medium .It explains the properties like frequency, polarization, phase difference of incident light. NLO describes the interaction between the light and matter when the intensity of light is high enough to change the property of material. The non-linearity is typically observed at very intensity light such as laser .In nonlinear optics super position principle is not followed .

CHAPTER 2

IMIDAZOLE

"Imidazole" is a five-membered aromatic molecule that contains of two annular nitrogen atoms. Where, One of two nitrogen atoms behaves like a pyrrole-type nitrogen and the other nitrogen atom shows a close resemblance to a pyridine-type nitrogen. The systematic name of this structure is 1,3-diazole, and the molecular formula is $C_3H_4N_2$, which is very rarely used in the chemical literature. This is classified as an alkaloid. An imidazole ring is an important biological building block of many natural compounds with a wide range of biological activities, such as Histidine and the related hormone histamine. An imidazole can serve as both base and as a weak acid. Many drugs such as antifungal drugs and nitroimidazole contain imidazole rings. Imidazole and its derivatives are widely used as intermediates in synthesis of organic target compounds, including pharmaceuticals, agrochemicals, dyes, photographic chemicals, corrosion inhibitors, epoxy curing agents, adhesives and plastic modifiers etc. Several biologically active synthetic compounds contained of five-membered nitrogen-those have structure that contain heterocyclic ring. Structural frameworks have been described as privileged structures particular; nitrogen containing polycyclic structures has been reported to be associated with a wide range of biological activity. The high therapeutic properties of the imidazole related drugs have encouraged the medicinal chemists to synthesize a large number of novel chemotherapeutic agents. Imidazole drugs have broadened scope in remedying various dispositions in clinical medicines. Its wide range Medicinal properties include anticancer, β -lactamase inhibitors, carboxypeptidase inhibitors, hemeoxygenase inhibitors, anti-aging agents, anticoagulants, anti-inflammatory, antibacterial, antifungal, antiviral, anti-tubercular, anti-diabetic and anti-malarial etc. Imidazole and its derivatives are said to be physiologically and pharmacologically active and find applications in the treatment of several diseases. Imidazole is also present in the structure of many natural synthetic drug molecules, for Azomycin and metronidazole etc. Imidazole that present in polymers has been traditionally utilized in a variety of applications that include immobilized catalysts, redox reactions, water purifications, hydrometallurgy/metal recovery ion, proton conductors etc. They also have major applications in biochemical processes, catalysis, electron transport systems, and nanoparticle electron hypothesis etc. One of the major applications of imidazole is in the role of purification of his tagged proteins in immobilized metal affinity chromatography (MAC). Imidazole is a major part of the theophylline molecule, found in tea leaves and coffee beans, which stimulates the central nervous system. Many compounds of industrial and technological importance contain imidazole derivatives. The thermostable polybenzimidazole (PBI) contains imidazole fused to a benzene ring and linked to benzene and acts mainly as a fire retardant. Imidazole can also be found in various compounds which are used for photography and electronics.

Spectroscopic, DFT molecular dynamics and molecular docking study of 1-butyl 2-(4-hydroxyphenyl) 4, 5-dimethyl -imidazole 3-oxide

This compound is a derivative of imidazole derivative . Spectroscopic , DFT , molecular dynamics and molecular docking of the derivative can be studied.

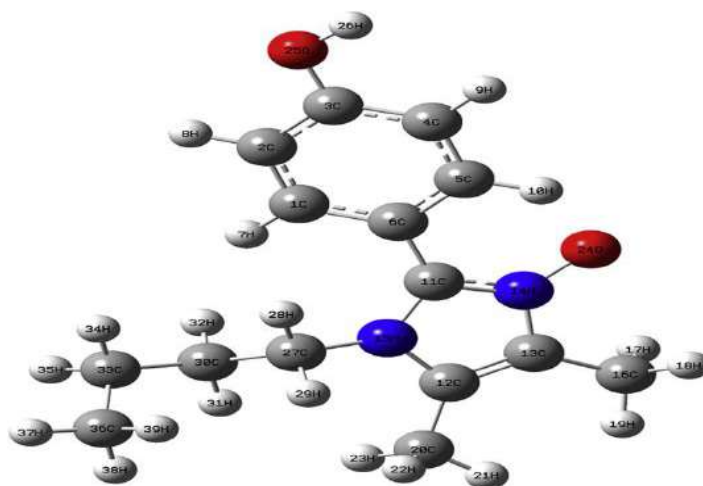


Fig:2.1 -structure of 1-butyl-2-(4-hydroxyphenyl)-4, 5-dimethyl-imidazole 3-oxide

- Using Gaussian software package FTIR and FT Raman spectrum of 1 butyl 2 (4hydroxyphenyl) 4,5 dimethyl imidazole 3 oxide has been recorded and theoretical study has been made.
- To determine the vibrational frequencies and geometrical parameters DFT / B3LYP calculations has been done using 6.311++G (d,p) (5D , 7F) basic set Using potential energy distribution (PED) calculations the assignment of the normal modes are done .
- In order to find its role in non linear optics first and second hyperpolarizabilities are calculated .
- using NBO analysis the stability of the molecule arising from hyper conjugative interaction and charge delocalization has been done .
- using DFT method the molecular electrostatic potential was calculated and most reactive part in the molecule .
- By calculate the average local ionization surface and fukui function reactive sites of the title molecules have been determined.

- Intra molecular non covalent interaction , analyzing electron density between atoms have been determined.
- Using bond dissociation energies for all single acyclic bond the possible location prons autoxidation and location where degradation could have been determined .
- Atoms with pronounced interactions with water molecules have been located by calculation of radicle distribution function obtained after molecular dynamics simulations .
- The calculated NMR values are in good agreement with experimental data .

EXPERIMENTAL DETAILS

1-butyl-2-(4-hydroxyphenyl)-4,5-dimethyl-imidazole 3-oxide was synthesized via a solvent free procedure. 10 mmole (1.01 g) of 3-(hydroxyimino) butan-2-one was mixed with 10 mmole (1.36 g) of 4-hydroxybenzaldehyde and 15 mmole (1.5 ml) of n-butyl amine in an agate mortar and grinded thoroughly for 2 minutes with a pestle into an intimate mixture and subsequently heated in an oil bath at 115-120°C, when a melt was formed. After further 8 minutes of heating, the completion of the reaction was indicated by thin layer chromatography (TLC), performed using 0.25 mm Merck Aluminium silica gel 60-F254 precoated plates. On cooling the melt slowly solidified and to the product so formed was added a little amount of ether whereby a precipitate was obtained. The precipitate was washed with hot ethyl acetate. Recrystallization from ethanol gave a product with the same melting point. The FT-Raman spectrum was recorded using KBr pellets on a DR/Jasco FT-IR 6300 spectrometer.

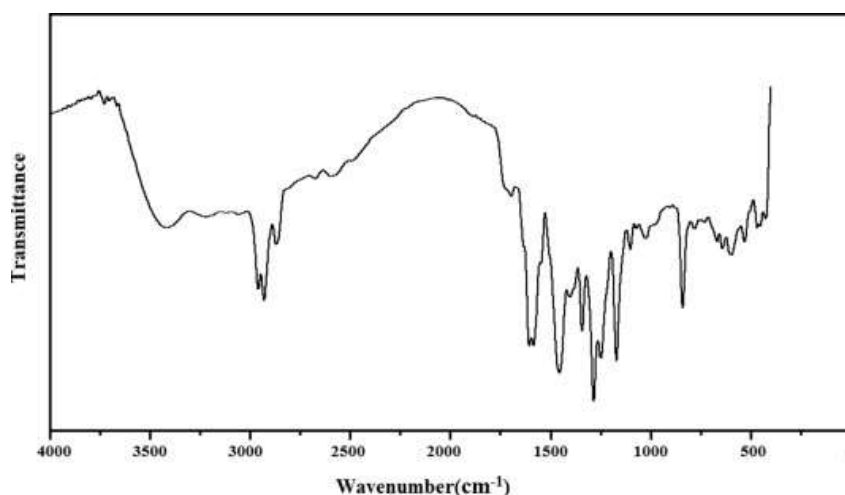


Figure 2.2 FT IR spectrum

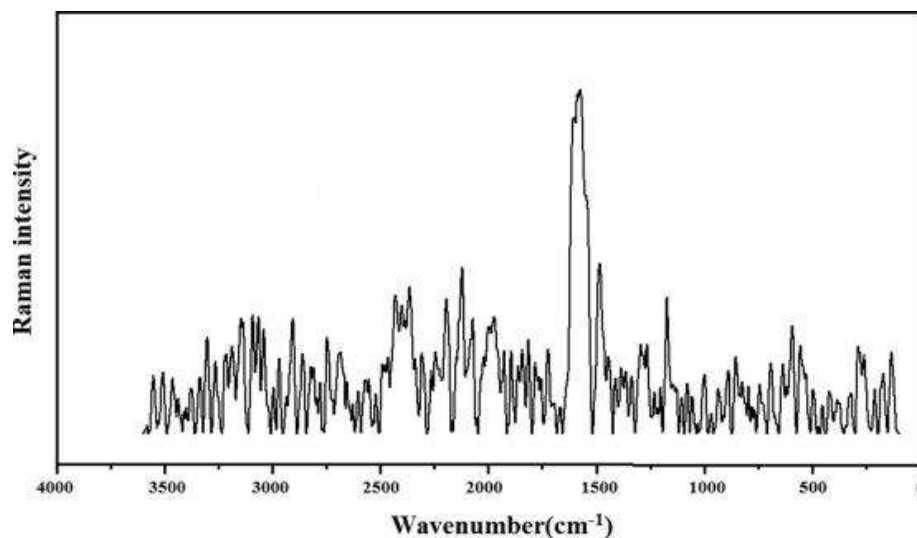


Figure 2.3 FT Raman spectrum

The FT-Raman spectrum was obtained on a Bruker RFS 100/s, Germany. For excitation of the spectrum the emission of Nd:YAG laser was used, excitation wavelength 1064 nm, maximal power 150 mW, measurement on solid sample. The spectral resolution after apodization was 2 cm^{-1} . NMR were recorded in dms_o-d₆ on a Bruker Avance 300 spectrometer. The electrospray mass spectrum was recorded on a MICROMASS QUATTRO II triple quadruple mass spectrometer. The ESI capillary was set at 3.5 kV and cone voltage was 40V. ESI m/z found for $\text{C}_{15}\text{H}_{20}\text{N}_2\text{O}_2$: 260.15 (M+1). Melting Point (uncorrected): 128-130°C. Anal. Calcd. for $\text{C}_{15}\text{H}_{20}\text{N}_2\text{O}_2$: C, 69.20; H, 7.74; N, 10.76; O, 12.29; Found: C, 69.12; H, 7.81; N, 10.52; O, 12.45.

RESULT

IR and Raman Spectra

IR and Raman bands and calculated frequencies and assignment are observed. The phenyl ring and imidazole ring are designed as ph I and Ring II and the experimentally observed IR and Raman band are compared with the values given by B3LYP/6-311+G(d,p)(5D,7F) values.

Geometrical Parameters

The optimized molecular structure of 1-butyl-2-(4-hydroxyphenyl)-4, 5-dimethyl-imidazole 3-oxide was determined by using Gaussian09 program. From the optimized geometry it shows that the C-C bond length of $\text{C}_6\text{-C}_{11}$ (1.4582Å) is greater than that of $\text{C}_5\text{-C}_6$ (1.4068Å) and $\text{C}_1\text{-C}_6$ (1.4064Å), because of the delocalization of electron density of $\text{C}_6\text{-C}_{11}$ with the ring in which N-O is substituted. Also the

slight difference in the bond length of C₂-C₃ (1.3943 Å), C₃-C₄ (1.3960 Å) is due to the presence of -OH group in the neighborhood. The C-N bond lengths C₁₁-N₁₄ (1.3536), C₁₁-N₁₅ (1.3869), C₁₂-C₁₅ (1.3829), and C₁₃-C₁₄ (1.3944) are different because of the difference in their environment and also assume a double bond character in C₁₁-C₁₄. The bond angle between C₆-C₁₁-N₁₄ (124.5°) and C₆-C₁₁-N₁₅ (128.4°) indicates the better. Also C₁₁-N₁₄-C₁₃ (109.3°) and C₁₁-N₁₂-C₁₅ (108.8°) indicates slightly higher electronegative property of atom.

Frontier Molecular Orbital analysis (FMO)

The frontier molecular orbital can offer a reasonable qualitative prediction of the excitation properties and the ability of electron transport. The highest molecular orbital (HOMO) is the outermost higher energy orbital containing electron so it acts as an electron donor. The lowest unoccupied molecular orbital (LUMO) is the lowest energy orbital that has the room to accept electron and act as an electron acceptor. HOMO and LUMO are very popular quantum parameter which determine the molecular reactivity. The energies of the HOMO and LUMO orbitals of the given compound are calculated using B3LYP/6-311++G (d,p) (5D,7F) basis set. The HOMO, LUMO energy and Energy gap are -7.99, -5.11, and 2.88 respectively. The energies of HOMO and LUMO are negative, which shows that the compound is stable. Conceptual DFT based descriptors have helped in many ways to understand the structure of the molecule and their reactivity by calculating the chemical potential, global hardness and electrophilicity.

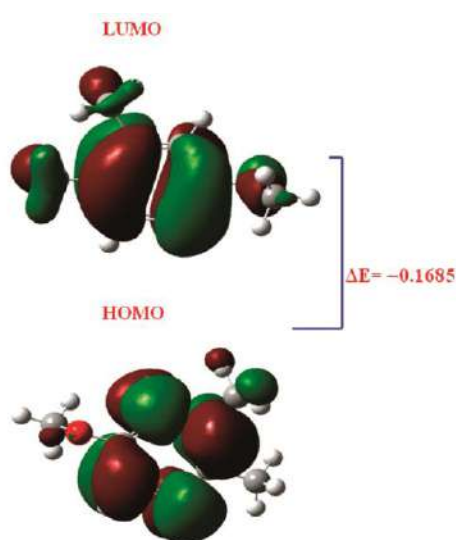


Figure 2.4-Homo and lumo plots of 1-butyl-2-(4-hydroxyphenyl)-4,5-dimethyl-imidazole 3-oxide

Molecular Electrostatic Potential (MEP)

MEP is very useful descriptor in understanding sites for electrophilic attack and nucleophilic reactions and for the study of biological recognition process. MEP mapping is useful in the investigation of the molecular structure with its physicochemical property relationship. To predict reactive sites of electrophilic and nucleophilic attacks for the investigated molecule, MEP at the B3LYP/6-311++G (d,p) (5D,7F) optimized geometry was calculated.

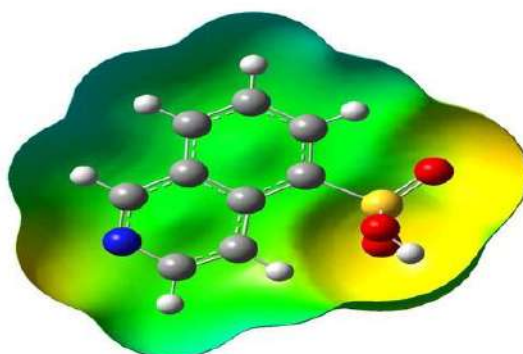


Figure 2.5 MEP plot of 1-butyl-2-(4-hydroxyphenyl)-4,5-dimethyl-imidazole 3-oxide

¹H NMR spectrum

Experimental spectrum data of 1-butyl-2-(4-hydroxyphenyl)-4,5-dimethyl-imidazole 3-oxide in DMSO is obtained at 300 MHz. B3LYP/GIAO was used to calculate the absolute isotropic chemical shielding of the compound.

Non linear optical property (NLO)

The first hyperpolarizability (β_0) of this novel molecular system is calculated using B3LYP/6-311++G (d,p) (5D,7F) method, based on the finite field approach. In the presence of an applied electric field, the energy of the system is a function of electric field. First hyperpolarizability is a third rank tensor that can be described by $3 \times 3 \times 3$ matrices. The 27 components of the 3D matrix can be reduced to 10 components due to the Kleinman symmetry. The calculated first hyperpolarizability of the compound is 3.61×10^{-30} esu, which is comparable with the reported values of similar derivatives and which is 27.76 times that of standard NLO material urea (0.13×10^{-30} esu).

The average hyperpolarizability has been calculated by the expression

$$\langle \gamma \rangle = (\gamma_{xxxx} + \gamma_{yyyy} + \gamma_{zzzz} + 2\gamma_{xxyy} + 2\gamma_{xxzz} + 2\gamma_{yyzz})/5 .$$

The theoretical second order hyperpolarizability was calculated using the Gaussian software and is equal to $1.30020041 \times 10^{-36}$ esu .We conclude that the title compound is an attractive object for future studies of non linear optical property .

Compound	First hyperpolarizability ($\times 10^{-30}$ esu)	Second hyperpolarizability ($\times 10^{-36}$ esu)
NIOI	3.61	1.30

Natural Bond Orbital analysis (NBO)

NBO calculations was performed using NBO 3.1 program as implemented in the Gaussian09 package at the DFT/B3LYP level in order to understand various second-order interactions between the filled orbital of one system and vacant orbital of another system ,which is a measure of the intra-molecular delocalization or hyper conjugation and the important interactions .

Molecular Docking

High resolution crystal structure of CDK inhibitor was downloaded from the RSCB protein data bank website (PDB ID : 2XMY) . All molecular docking calculations were performed on auto Dock-vina software . The 3D crystal structure of CDK inhibitor was obtained from the protein data bank . The protein was prepared for docking by removing the co-crystallized ligands ,water and co-factor .The Auto Docking Tools (ADT) graphical user interface was used to calculate kollman charges and polar hydrogens. The ligand was prepared for docking by minimizing its energy at B3LYP/6-311++G(d,p) (5D,7F) level of theory . Particle charges were calculated by Geistenger method . Docking protocol was tested by extracting co-crystallized inhibitor from the protien and then docking the same . The docking protocol predict the same conformation as was present in the crystal structure with RMSD value well within the reliable range of 2\AA .Amongst the docked conformations , one which binds well at the active site was analyzed for detailed interactions in Discover studio visualize 4.0 software .

The global reactivity description

COMPOUND	I(ev)	χ (ev)	η (ev)	μ (ev)	ω (ev)
1-butyl-2-(4-hydroxyphenyl)-4,5-dimethyl-imidazole-3-oxide	6.43	3.21	3.201	-3.21	1.60

CONCLUSION

The vibrational spectroscopic studies of 2-(4-methoxyphenyl)-4,5-dimethyl-1H-imidazole 3-oxide in the ground state were exported experimentally and theoretically. Potential energy distribution of normal modes of vibration was done using GAR2PED program. The ring stretching modes in IR and Raman spectra are the evidence for charge transfer interaction between the donor and the acceptor group through the π system. This along with the lowering of HOMO-LUMO band gap supports for the bioactivity of the molecule. MEP predicts the most reactive part in the molecule. The calculated first hyperpolarizability is compared with the reported values of similar derivatives and in an attractive object in the future studies in nonlinear optics. The calculated $^1\text{H-NMR}$ result is in good agreement with experimental data. From the molecular docking study, the title compound formed three hydrogen bonds with residue, Thr-306, Ile-363 and Gln-357 and the results indicated that the said compound bound in the pocket include the residues construct the active pocket of CYP2B4.

CHAPTER 3

Conformational analysis and quantum descriptors of 1-[2-(2-hydroxy-3-methoxy-5-(4-methoxyphenylazo)benzaldehydeamino)ethyl]-3-methyl-3H-imidazole

This compound is a derivative of imidazole derivative. Spectroscopic, DFT, molecular dynamics and molecular docking of the derivative can be studied

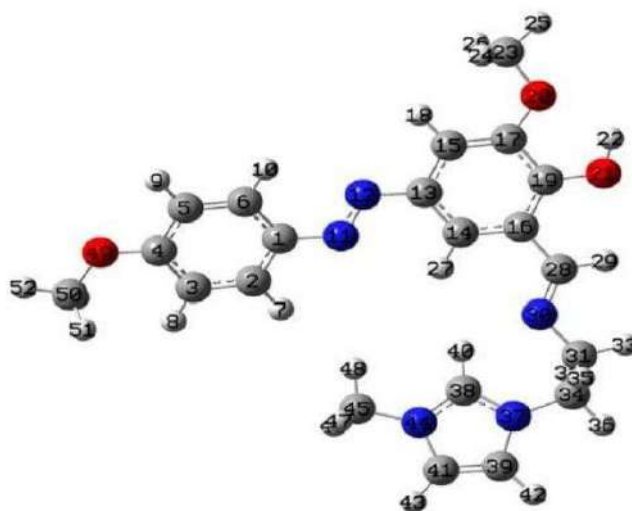


Figure 3.1. structure of 1-[2-(2-hydroxy-3-methoxy-5-(4-methoxyphenylazo)benzaldehydeamino)ethyl]-3-methyl-3H-imidazole

- The compound was synthesized and characterized using spectral analysis.
- Using potential energy scan for different rotatable bonds to the conformational analysis for obtaining the lowest energy conformer.
- Conformer with minimum energy is obtained along with the dihedral angles $N_{30}-C_{31}-C_{34}-N_{37}$.
- The nature and strength of the hydrogen bonding interaction is given by QTAIM analysis.
- The interaction of the compound with graphene is analysed in terms of SERS activity.
- For graphene drug system the chemical reactivity descriptors were investigated.
- NLO activity of parent drug and graphene drug shows good complexes.
- The compound exhibits inhibitory activity against cytochrome is peptidase.
- Interaction with graphene sheets are theoretically predicted.

EXPERIMENTAL DETAILS

All calculation related to the study of our given compound have been executed with the computational chemistry software package called Gaussian09 program. DFT theory with B3LYP with 6-311++G(d,p) basis have been taken to obtain the most accurate structural feature of the given compound. The most popular DFT functional is B3LYP and is widely used in density functional calculations. To compile percentage potential energy distribution and to correctly align vibrational wave numbers of the title compound GAR2PED and Gasview programs has been utilized. The nature of all bonds in the title compounds can be investigated by using QTAIM method. The QTAIM approach is useful in obtaining electron density values and bonding characteristics of the configuration. Using AIMALL program, the charge density ($\rho(r)$), Laplacian of charge density ($\Delta^2(r)$), ellipticity (λ^O) are calculated by AIMALL program. AIMALL is used to evaluate the nature of interaction. Based on QTAIM approach, every two interacting atoms were connected by the bond paths (BP), and one point on BP (saddle point) had maximum value of electron density named critical point (BCP). The compound prepared according to report of Mary et al. Perkin Elmer spectrometer was used for FT-IR spectrum and RAMAN spectrum of the compound was using Braker UTS 66V model interferometer using Nd:YAG laser source.

RESULTS

IR AND RAMAN Spectra

A sharp peak was observed at 3435, 3430 and 3447 experimentally and 3451cm^{-1} (DFT) are ν_{OH} . δ_{OH} was 1250 (DFT) and seen at 1251/1252 cm^{-1} (IR/RAMAN) are ν_{CH} mode and the DFT values are 3221-2850 cm^{-1} . The $\nu_{\text{C}=\text{CR}_3}$ is assigned at 1547 cm^{-1} and at 1549/1547 cm^{-1} (IR) spectrum for the compound.

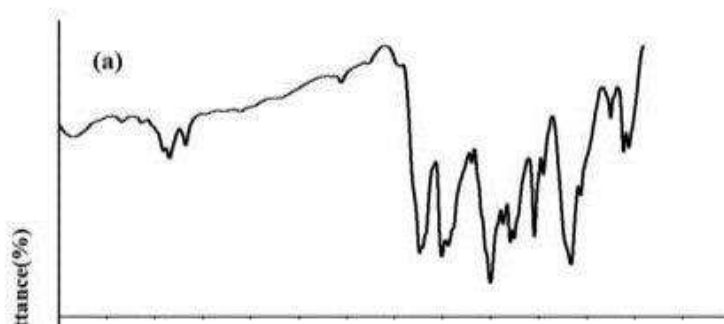


Figure 3.2(a)

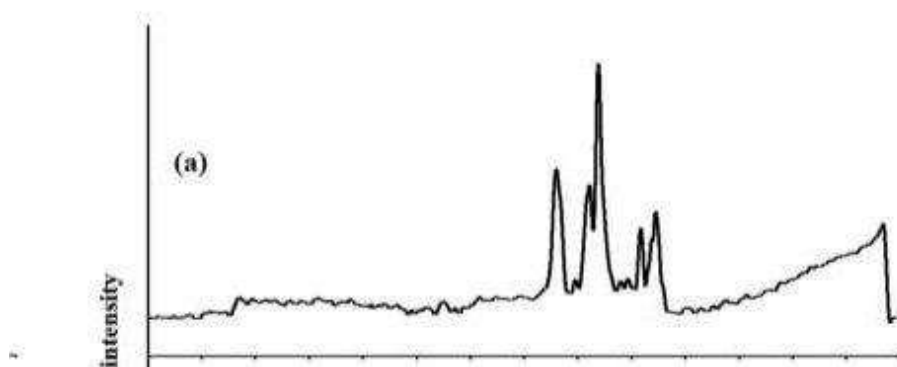


Figure3.3 (b)

figure 3.2(a) is the FT IR spectra and figure 3.3(b) is the FT Raman spectrum

Molecular Reactivity Analysis

The HOMO-LUMO gap is a basic parameter in deciding atomic transport effects. Such as chemical reactivity of the substances kinetic stability of a molecule since it is a measure of electron conductivity. The value of band gap (AK_{H-L}) of the given compound is 2.382. The HOMO and LUMO energies are -7.822 , -5.41 . The HOMO is over entire part of the compound except the ring R_3 , CH_2 groups. LUMO spread in the same region as in the HOMO of the reactivity descriptors indicates that the title compound is chemically reactive. PDOS spectra shows no much overlap is present in FMOS but overlap in the core orbital V_V-V_B spectra gives compound absorption/oscillation strength/LHE values as 350.78,341.67/1.092,0,9950/91.92 and 89.98% for the compound.

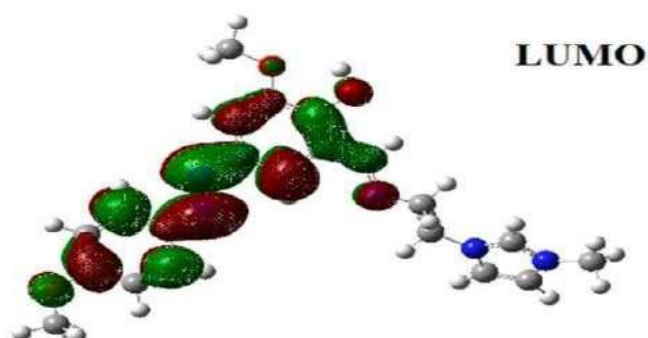


Figure 3.4 LUMO structure

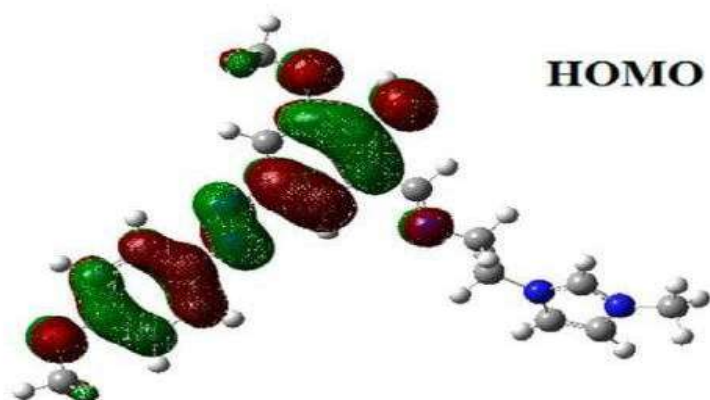


Figure 3.5 Homo structure

Molecular Electrostatic Potential (MEP)

The distribution of charges in space charges to the electrostatic potential. The various colour coding on the molecular electrostatic potential is shown in which that indicates the sites feasible for the electrophilic and nucleophilic attraction. The yellow colour region around the oxygen atoms and the rings R_1 and R_2 in the compound is electrophilic region. Whereas the blue colour region across R_3 for the compound shows low electron density thus it is nucleophilic.

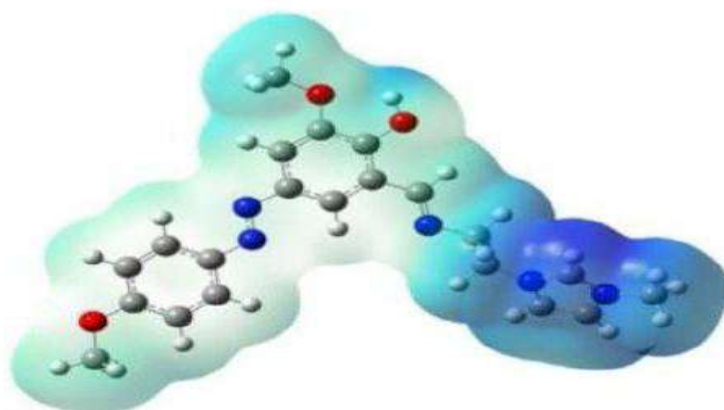


Figure 3.6 Colour coding on the molecular electrostatic potential

Non -Linear Optical Property (NLO)

The orientation of charge levels among the molecular site in the compound are usually measured in different order such as first and second order. Normally the first order is measured loosely bounded electron delocalization and they occupied with high pressure generated by interactive and repulsive forces among the molecular sites and leads static chemical potential for regulate drug activity. In the second order, The bounded electron with strong binding forces with nucleus delocalized with Frenkel pressure generates enformed asymmetrical polarization called hyperpolarization, causing inter atomic state potential which is the root cause for sensitive drug commotion. The first order hyperpolarizability (10^{-30} esu) of the compound is 40.147×10^{-30} esu, while next order value is -3.02×10^{-36} esu. Here the first order polarizability for both chain and ring was enabled and this causes strong drug hardness capability. Here, the second order polarizability of the compound was also enables strongly which showed stabilization of constituent drug potential in the compound.

NBO Analysis

The important NBO interactions are $049 \rightarrow \pi^*(C_3-C_{14}), N44 \rightarrow \pi^*(C_{39}-C_{41}), N44 \rightarrow \pi(N_{37}-C_{38}), 021 \rightarrow \pi^*(C_{16}-C_{19}), 120 \rightarrow \pi^*(C_{15}-C_{17})$ with energies 31.98, 29.08, 78.82, 29.30, 26.27 kcal/mol.

Molecular Docking

To explore the drug properties ligand-protein interaction is essential to be investigated to get more insights into the binding sites of biologically active molecules with amino acids of the protein and docking has been carried out by using Autodock software, using online PASS analysis, targets, chemo sensitizer APOAI expression enhances HMGCS2 expression enhancer and CYP₂C₁₉ induces as predicted using the PDB's, IQMQ, AJB4, 2WYA, 4KFO, HMY is docked for docking Lamerckion genetic algorithm included in Autodock software has been implemented. The maximum energy value is -9.8 Kcal/mol. These results suggests that the compound shows activity against these cytochrome c peroxidase.

The global reactivity description

COMPOUND	I (ev)	χ (ev)	η (ev)	μ (ev)	ω (ev)
1-[2-(2-hydroxy-3-methoxy-5-(4-methoxyphenylazo)benzaldehydeamino)ethyl]-3-methyl-3H-imidazole	7.822	6.63	1.191	-6.632	18.465

CONCLUSION

In these study, quantum chemical descriptors and viberational spectral studies of the compound is studied. Conformational analysis of the compound identifies the most stable conformers. The theoratically obtained data are in agreement with the experimental results. The FMO'S determined energy gaps shows the chemical stability. The NBO analysis results account for the natural charge accumulation in the investigated molecule. QTAIM study shows that ellipticity of OH bonds has values higher than the ellipticity of the other bonds which is due to the hydrogen interactions. Docking stimulating obtained shows good binding affinities with the receptors. This study could hopefully serve as a base for further drug research and devolopments.

CHAPTER 4

Experimental and theoretical Fourier transform infrared and Raman spectroscopy, density functional theory, antibacterial activity and molecular docking studies on 1-(4-methoxyphenyl)-1H-imidazole.

This compound is a derivative of imidazole derivative . Spectroscopic , DFT , molecular dynamics and molecular docking of the derivative can be studied

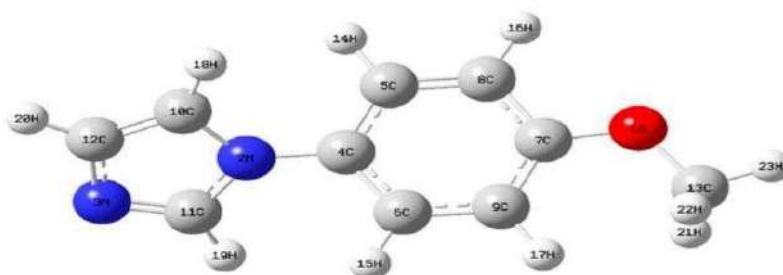


Figure 4.1 structure of 1-(4-methoxyphenyl)-1H-imidazole.

- Fourier transform infrared (FT-IR) and (FT-RAMAN) spectra of 1 (4 methoxyphenyl) 1H imidazole were recorded and analysed.
- Using the density functional theory(DFT),(B3LYP)/6-311++g(d,p) basic set,vibrational wavenumbers of the structure were computed.
- Computational analysis were performed using the Gaussian09 and Gauss view 5.09 molecular vibration package.
- ^1H and ^{13}C NMR analysis of the title molecule were performed by the DFT/B3LYP method using the 6-311+G(2d,p) basic set with the GIAO method.
- Using Autodock vina software and Autodock Tods graphical interface molecular docking investigation were performed.
- From the protein data bank the 3D dimensional crystal structure of protein was obtained.
- Using the discovery studio visualize the outputs from autodock vina were visualized.

- The binding sites were centered on the selected protein and molecule, and a grid box was centered with 40x40x40 points and 0.375 Å grid spacing.

EXPERIMENTAL DETAILS

1-(4-methoxyphenyl)-1H-imidazole was supplied from sigma-aldrich chemical company. This structure is solid at 98% purity and the cas and MDL numbers of the molecule are 10040-95-6 and MFCD00060492, respectively. The melting temperature of the title molecule is given in the range of 59–67 °C. The FT-IR and FT-Raman spectra were recorded in the regions between 4000 and 400 and 4000 and 100 cm⁻¹ without further purification. Bruker FT-IR spectrometer with ATR equipment was used to obtain the FT-IR spectrum, Jasco FT-Raman spectrometer with NRS400 confocal microscope was used for the FT-Raman spectrum. Chemical shifts of the title molecule for ¹H NMR and ¹³C NMR analysis were recorded in the range of 0–15 ppm and 100–200 ppm, respectively, in chloroform solvent at room temperature using the Bruker Ultrashield 300 MHz spectrometer. The UV–visible absorption spectrum was recorded in the range of 200–500 nm by using the Shimadzu UV-2101PC spectrophotometer.

The antibacterial activity of 1-(methoxyphenyl)-1H-imidazole was evaluated against thirteen different bacterial strains. The test stock (60 mg) of the compound was dissolved in 1 ml of dimethyl sulfoxide (% 10 DMSO). The test compound was dropped into the well (6 mm in diameter) at a concentration of 60 mg/mL, and the plates were incubated for 24 h at 37° C for all bacteria. Antibacterial activity was measured based on the diameter of the inhibition zone in mm. Ampicillin was used as a standard antibacterial drug for the comparison of activities. The anti-quorum activity of the compound was determined against *Chromobacterium violaceum* ATCC 12,472 in LB agar surface by a swap. Then, wells were drilled in LB agar using a cork borer, and the tested compound (5 mg/mL) was applied to the wells after dissolving in 10% DMSO (McLean et al. 1997). The plates were incubated at 30 °C for 24 h to determine inhibition of pigment production around the well. The formation of a clear halo around the disc and the formation of bacterial growth inhibition was evaluated as positive

Anti-bacterial activity by minimum inhibitory concentrations were determined in a sterile 96-well plate by using a broth micro-dilution technique. The compound was prepared at a concentration of 200mg/ml, its microtiter was also determined, and it was incubated at 37°c for 24h. The lowest concentration at which no visible bacterial growth could be found was taken as the MIC value.

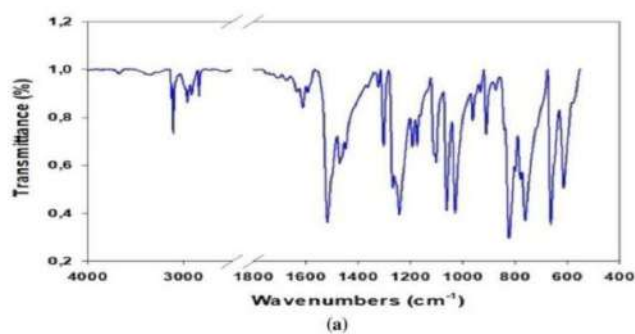


Figure 4.2

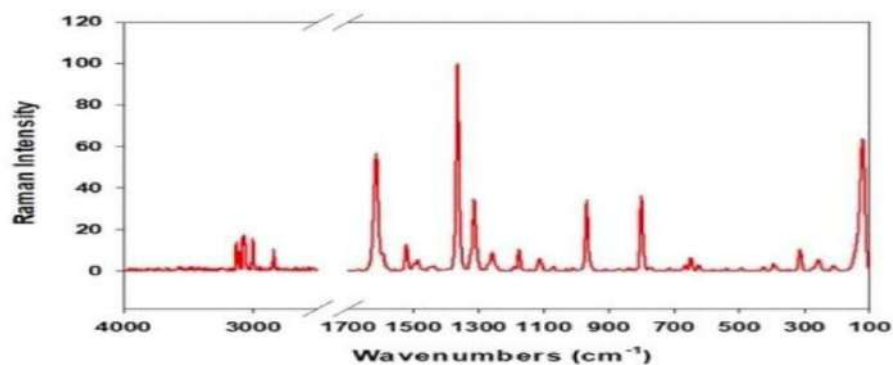


Figure 4.3

^1H and ^{13}C NMR analysis

^1H NMR analysis provides information on the amounts of a number of protons as well as the nature of the immediate environment of these protons. ^{13}C NMR analysis gives structural information about the different carbon atoms in the molecules. The experimental and computer calculation techniques for NMR analysis are widely used together for better understanding and interpret the structure of molecules. In the theoretical calculation for ^1H and ^{13}C NMR analysis of the title molecule the density functional theory (DFT/B3LYP) method using the 6-311+G(2d,p) basis set with the GIAO method has been selected as a computational method. According to the final results, the experimental and theoretical chemical shift values of ^1H and ^{13}C NMR for the compound are good agreement with each other.

HOMO-LUMO Analysis

The electron donation and acceptance abilities of a molecule are determined according to HOMO and LUMO molecular orbital energy values. HOMO is the highest energy molecular orbital occupied by electrons, LUMO is the lowest energy molecular orbital not occupied by electrons. Chemical reactions

take place by transferring electrons in the HOMO molecular orbital to the LUMO molecular orbital. Both HOMO and LUMO molecular orbitals have an important role in electronic and optical properties. Chemical properties of a molecule such as chemical hardness, chemical potential, reactivity, kinetic stability, chemical softness, electronegativity, electrophilicity, and optical polarizability can be explained by these molecular orbitals. According to HOMO and LUMO energy values of a molecule, the ionization potential, electron affinity, global hardness, chemical potential, electronegativity, and global electrophilicity can be calculated follows: $I = -E_{\text{HOMO}}$, $A = -E_{\text{LUMO}}$, $\eta = (-E_{\text{HOMO}} + E_{\text{LUMO}})/2$, $\mu_c = (E_{\text{HOMO}} + E_{\text{LUMO}})/2$, $\pi = -\mu_c$ and $\omega = \mu_c^2 / 2\eta$. The HOMO and LUMO energy values of the title molecule in the gas phase and in water solvent were calculated at the B3LYP/6-311++g (d,p) levels. The HOMO and LUMO molecular orbital energy values in the gas phase were obtained as -6.27 eV and -1 eV, these energy values in water were calculated as -6.32 eV and -0.90 eV, respectively. The HOMO energy decreases with the increase of dielectric constant, the LUMO energy is increased. The HOMO-LUMO energy gap in the gas phase and in water solvent are found to be 5.27 and 5.42 eV, respectively. The energy gap values of the title molecule increases with depending on the increase in the dielectric constant. Also the ionization potential values of the title molecule in the water is increased. This means that the transfer of electrons from HOMO to LUMO is easier in the gas phase. According to the energy gap value we can say that the molecule has hard structure. According to the HOMO distribution of the molecule it is seen that the electron density is determined over almost the entire molecule. LUMO is mostly distributed on the phenyl ring.

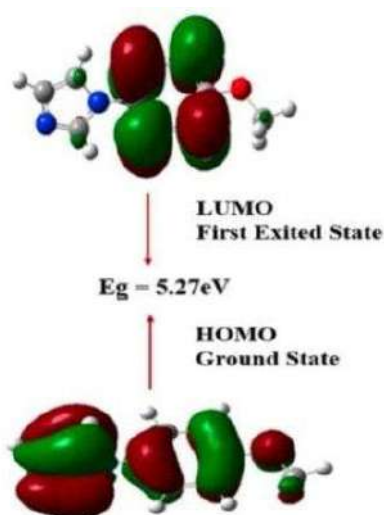


Figure 4.4

Molecular Electrostatic Potential (MEP)

The molecular electrostatic potential is a powerful electronic density tool used to determine electrophilic and nucleophilic reaction regions and understand hydrogen bond interactions. The MEP surface explains the neutral, negative and positive electrostatic potential with colour band that includes red, orange, yellow, green, and blue. Red color is used to determine the negative electrostatic potential region on the MEP surface, the dark blue represents the positive electrostatic potential region. The yellow color represents the less negative potential region than the red color. The green color represents the neutral regions compared to the red and dark blue regions, while the light blue region represents the less positive potential region than the blue region. The electrophilic region is localized in N₃ atom of the imidazole ring. Especially the C atom and the H atoms in the methoxy group and the other H atoms are located in the less positive potential region. In two-dimensional map, the all molecule is in the less negative potential region.

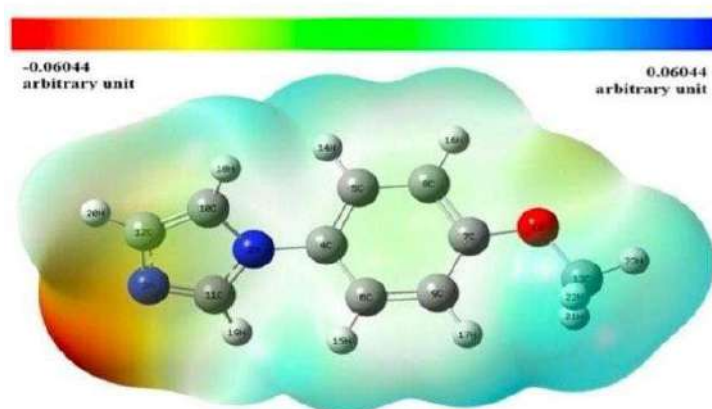


Figure 4.5 Molecular electrostatic potential

Non -Linear Optical Property

The optical property of a substance is expressed as the response of electrons in the structure express to an electric field .Hyper polarizability is defined as the quantity that effects the nonlinear optical properties of the material. The urea compound is used as a brink value in the NLO characteristics analysis and the other structure are compared with the brink value.The first hyperpolarizability value of urea is 0.3728×10^{-30} esu.This value obtained obtained for our compound is 1.75×10^{-30} esu and this is greater than that of urea.Therefore we can say that our title compound has non-linear optical properties.

NBO Analysis

The NBO analysis uses for examining molecular orbits which give information about the reactivity of molecules. It is an effective method to explain the electronic charges of the atoms and the binding potential of a molecule. Atomic charges effect molecular moment, molecular polarity, electronic structure, band type, bond structure and many more other properties In a molecular system. Charge distribution analysis was performed by using 6-311++g(d,p) basis set on the optimized structure of 1-(4-methoxyphenyl)-1H-imidazole. The magnitude of all H atom in the structure to be found as positive. According to the three charge analysis types, the O atom in methoxy group. The N₂ and N₃ atoms in the imidazole ring and the C₅, C₆, C₈ and C₉ atoms in the phenyl ring are electronegative. Carbon atoms have positive charge values were found as C₄, C₇ and C₁₁ atoms.

Molecular Docking

Molecular docking is one of the most common application used in structural molecular biology and computer assisted drug design. The ligand–protein interaction predicts the dominant binding modes of the ligand to a protein. The interaction of the compound with the 4URM, 4JCN, and 2RG7 proteins obtained from the protein data bank were performed in the molecular docking simulation using the Autodock program. The compound was docked into the reactive region of the 4URM, 4JCN, and 2RG7 proteins and the docking minimum binding affinity values were found to be -5.30 kcal/mol, -5.10 kcal/mol respectively. The ligand interaction of the 4URM protein, it was determined that the N₃ atoms of compound is located at a distance of 2.53 Å from the H of the THR173. In the ligand interaction of the 4JCN protein, the H atom of ASN274 was found to be at a distance of 1.95 Å from the N₃ atom of the ligand. For the 2RG7 protein, the hydrogen bond acceptor interaction was defined at a distance of 2.35 Å between the N₃ atom of the ligand and TRP87. According to this the title compound may exhibit biological activity and contribute to the synthesis and development of new drugs in the future.

The global reactivity description

COMPOUND	I (ev)	χ (ev)	η (ev)	μ (ev)	ω (ev)
1-(4-methoxyphenyl)-1H-imidazole	6.27(gas phase)	3.64(gas phase)	2.64(gas phase)	-3.64(gas phase)	2.51(gas phase)
	6.32(water phase)	2.71(water phase)	2.71(water phase)	-3.61(water phase)	2.41(water phase)

CONCLUSION

A complete vibrational analysis of 1-(4-methoxyphenyl)-1H-imidazole was performed using the density functional theory basis by Becke-3-Lee-Yang-Parr (B3LYP) functional using 6-311++G(d,p) basis set. The computational wavenumbers suggested which are in agreement with the observed wavenumbers from the FT-IR and FT-Raman spectra. To determine the electrophilic and nucleophilic reaction regions and to hydrogen bond interactions, molecular electrostatic potential, Fukui functions and charge analysis were used. The ^1H and ^{13}C NMR analyses were performed to better understand and interpret the structure of the title compound. The first hyperpolarizability values for the 1-(4-methoxyphenyl)-1H-imidazole is 1.75×10^{-30} esu and this value is found to be approximately 5 times greater than that of urea. Therefore this molecule has a high non-linear optic property. According to the molecular docking the compound may promising a strong new antibacterial effect.

CHAPTER 5

Spectroscopic Analysis and Molecular Docking of 2-Chloro-1-(4-methoxyphenyl-4-5-dimethyl – 1H-Imidazole [CLMPDI] & Investigation of its reactive properties by DFT and Molecular Dynamics Simulations

This compound is a derivative of imidazole derivative . Spectroscopic , DFT , molecular dynamics and molecular docking of the derivative can be studied

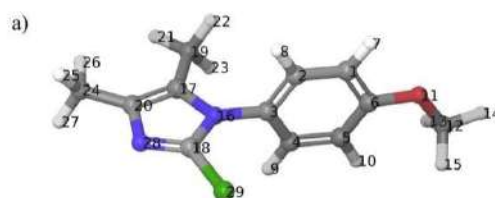


Figure:5.1. Optimized geometry of CLMPDI

The imidazole derivative compound has been reported using solvent free synthesis.

- Spectroscopic methods encompassed IR, FT-Raman and NMR techniques using the mutual comparison off experimentally and computationally obtained of DFT /B3LYP level of theory.
- Reactivity study based on the DFT calculations encompassed molecular orbitals analysis followed by calculations of Molecular Electrostatic Potential (MEP)and Average Local Ionization Energy (ALIE), Fukui functions and Bond Dissociation Energy (BDE).
- Using molecular dynamics (MD) simulations of the stability of the title molecules in under has been investigated.
- Using molecular docking procedure interactivity with aspulvinone dimethylallyltransferase protein has been evaluated.

- The Compound showed activity against all focus bacterial stain both gram positive and gram negative bacteria
- All possible combinations of compound have been obtained by application of macro model program and OPLS3 force field.
- All conformations have been optimized with Jaguar 9.7 program using a B3LYP exchange correlation functional and 6-31G (d, p) of theory in the order to identify the lowest energy conformations.
- True ground state of the lowest energy states have been confirmed by vibrational analysis at the same level of theory at which molecules were optimized, which yield only positive frequencies.
- Molecular orbitals, hyperpolarizabilities and NBO analysis have been obtained by program.
- The input and output fields for the GAUSSIAN09 were prepared, analyzed and visualized with Gaussian view 5 GUI and wavenumbers are assigned with the help of potential energy distribution by using the GAR2PED software.
- MD simulations have been done with the help of Desmond program and OPLS3 force field.

EXPERIMENTAL DETAILS

In continuation of the process of developing a mild greener and synthetic pathway for the preparation of compound under solvent free and room temperature condition for the conversion good excellent yields. The compound Imidazole-N-oxide is easily prepared. In the process allyl chloride as a chlorination agent and Imidazole-N-Oxide (2:1) is used are grinded in a mortar and pestle in the presence of a under the solvent free condition.

For the preparation of Imidazole-N-oxide, 1 mmole of the mono oxide, 1 mmole of the aldehyde and 385 mg (5mmole) of ammonium acetate was ground into a miniature in a mortar and pestle. The miniature was then heated to 115⁰ C -120⁰ C in an oil bath with constant shaking under solvent free condition. A black solution resulted which was coded when a black sticky precipitate formed. The black precipitate was then added a small volume of diethyl ether when a brown precipitate separated. The precipitate was then thoroughly washed using Ethyl acetate dissolved in Ethanol and crystallized by the addition of water to yield pure products that was isolated by spectral investigation.

For the preparation of chlorination at C-2 position of the substituted imidazole the compound was synthesized via a mild and solvent free condition with Imidazole -N-Oxide(1mmol), alkyl chloride (2 mmole) and tetraethyl amine (1.5mmole) was ground into an intimate miniature in an agate mortar and pestle. The miniature was then stirred at a rate of 10min under solvent-less condition. Then the reaction mixture was then dissolved in dichloromethane, washed with over Magnesium sulphate . Filterate was

subjected to chromatography on Silica gel and petroleum, ether/ ethyl acetate. Finally pure product was isolated by spectral investigation.

RESULT

IR & Raman Spectra

The wavenumber (theoretical, IR and Raman) and vibrational assignments of the compounds are obtained. The phenyl and imidazole rings are designated as PhI and PhII respectively. DFT calculations given the uPH (phenyl ring stretching modes) at 1585, 1551, 1494, 1396, 1286 cm^{-1} . For compound and corresponding experimental bands observed at 1584, 1280 cm^{-1} (IR) 1587, 1545, 1282 cm^{-1} (Raman). For 1-4-substituted phenyl rings, the ring breathing mode is expected in the interval 1005-1100 cm^{-1} bands at 1102 cm^{-1} (Raman), 1096 cm^{-1} (DFT) and 1039 cm^{-1} (IR) 1044 cm^{-1} (DFT) are assigned as the modes of CLMPDI. The in-plane and out-plane CH bending Modes are assigned theoretically at 1301, 1161, 1096, 1006 cm^{-1} and at 966, 997, 838, 815 cm^{-1} for the compound. DFT calculations gives and C=C & C=N stretching modes at 1570, 1410 cm^{-1} for the compound.

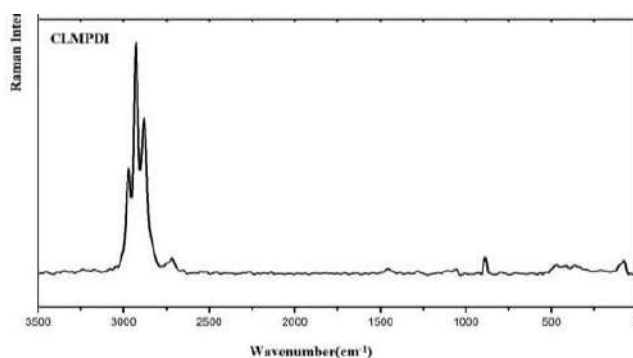


Figure:5.2. FT-Raman spectra of CLMPDI

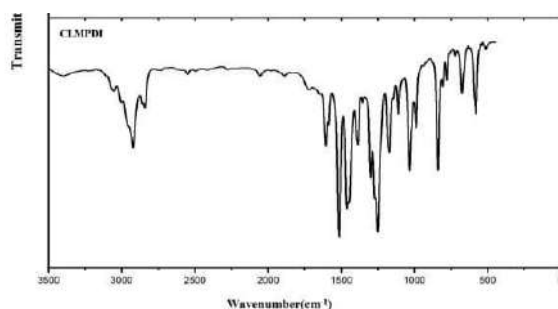


Figure:5.3. FT-IR Spectra of CLMPDI

Frontier Molecular Orbital analysis

The HOMO and LUMO of the given compound is given. In the given compound, HOMO is delocalized over the imidazole ring and CH₃ groups . plot of CLMPDI and chlorine atom with the imidazole ring while LOMO is delocalized over the HOMO and LOMO energies, the chemical descripts are given as ionization potential (I) = -E_{HOMO}, Electron affinity (A) = - E_{LUMO} , Hardness , $\eta = (I - A) / 2$, Electronegativity $X = 1 + A$, chemical potential $\mu = - (I + A) / 2$ and electrophilicity $\omega = \mu^2 / 2\eta$. The energies of the HOMO ,LUMO orbital and energy gap for the compound is E_{HOMO} = -7.546 eV , E_{LUMO} = -4.577 eV and energy gap = 2.971 eV.

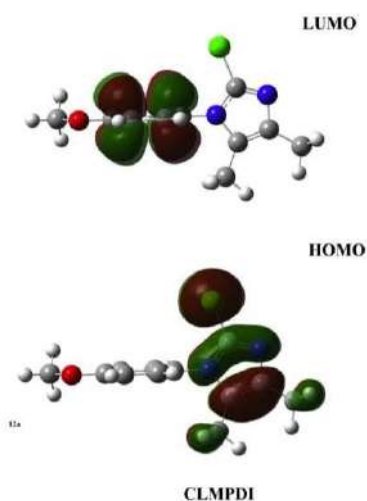


Figure: 5.4 HOMO & LUMO

Non -Linear Optical Property

The non-linear optical effect of organic material determined by the molecular polarizabilities which depend on Polarizability of the π bonding the orbitals and electrons in charge transfer takes place with electron accepting and electron denoting particles in the molecules and enhancing non-linearity. The calculated dipole moment and Polarizability of compound is 5.746 Debye and 5.991×10^{23} esu. The first order Polarizability is 2.999×10^{-30} esu. The second Hyperpolarizability is -1.5479×10^{-36} esu.

Molecular Electrostatic Potential &ALIE Surface

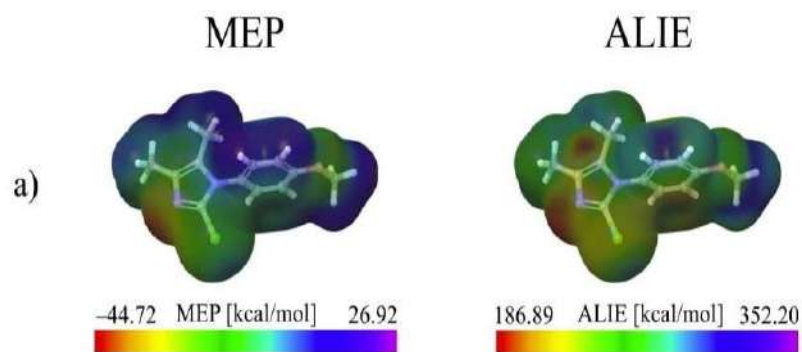


Figure: 5.5 - Representative MEP&ALIE Surfaces Of CLMPDI

MEP and ALIE surfaces are very frequently employed quantum molecular descriptors for identification of reactive molecular sites, especially when it comes to nucleophilic and electrophilic attacks. These descriptors are conveniently visualized by the mapping of their values to electron density surface, the latter ones are the better choice for the identification of molecular sites prone to electrophilic attacks. By analyzing the maximal and minimal MEP and ALIE values of the molecular parts with the same structure, a conclusion can be drawn that the compound is more reactive. Additionally, ALIE surface predicts one more location possibly sensitive towards attacks, above electrophilic the imidazole ring.

Natural Bond Orbital Analysis

The Natural Bond Orbital Analysis was performed using the NBO 3.1 program and the results of various interactions.

For the compound, the strong intramolecular hyper conjugate interactions are: C₅-C₆ from O₁₁ of n₁(O₁₁)/π*(C₅-C₆), C₁₈-N₂₈ from N₁₆ of n₁(N₁₆)/π*(C₁₈-N₂₈), N₁₆-C₁₈ from N₂₈ of n₁(N₂₈)/σ*(N₁₆-C₁₈), N₁₆-C₁₈ from Cl₂₉ of n₂(Cl₂₉)/σ*(N₁₆-C₁₈), C₁₈-N₂₈ from Cl₂₉ of n₃(Cl₂₉)/π*(C₁₈-N₂₈) with electron energies 28.89, 49.44, 9.94, 6.54 and 13.54 KJ/Mol. The natural hybrid orbitals with higher energies and low occupation numbers are n₂(O₁₁) and n₂(Cl₂₉) with energies -0.309, -0.312.

Molecular Docking

PASS analysis of the compound predicts aspirulvinone dimethylallyltransferase inhibitor activity with probability to the active value of 0.808. Imidazoles and benzimidazoles are privileged heterocyclic

bioactive compounds used with success in the clinical practice of innumerable diseases. This compound is designed as the anti-cancerous drugs and high resolution crystal structure of the dimethylallyltransferase inhibitor was downloaded from the protein data. All calculations were performed on the Autodock vina software. Amino acids TRP 291 forms H bonds with the imidazole ring; Leu 291 shows π -sigma interaction with the phenyl ring. Leu 105 forms allyl interaction and TRP 291 forms π -allyl interaction with methyl group. The docked ligands form stable complexes with dehydrogenase inhibitor which gives binding affinity values of 5.84 Cal/Mol for the compound.

Geometric Parameter

The C-C bond lengths of the phenyl ring lie in the range 1.4018-1.3896 Å. The C-O bond lengths $C_6-O_{11} = 1.3896\text{Å}$, $C_{12}-C_{11} = 1.4547\text{ Å}^0$. The bonds $C_{18}=N_{28}=1.3071\text{ Å}^0$, $C_{13}=N_{23}=1.3068\text{ Å}^0$ have typical double bond nature. The CCl bond lengths are 1.7888 and 1.7879 Å⁰ for compound, but $C_{18}-N_{16}=1.3786\text{Å}$, $C_{20}-N_{28}=1.4082\text{Å}$, $C_{17}-N_{16} = 1.4162\text{ Å}$, are less than single C-N bond length and this shows some resonance in this region of the molecules.

The global reactivity description

COMPOUND	I(ev)	χ (ev)	η (ev)	μ (ev)	ω (ev)
2-chloro-1-(4-methoxyphenyl-4,5-dimethyl-1H-imidazole	7.546	6.061	1.486	-6.061	12.36

CONCLUSION

Using the Density Functional Method, the FT Raman and FT IR spectra of the compound was reported experimentally and theoretically. The vibrational assignments were done on the analysis of the potential energy distribution. The phenyl ring and the imidazole ring are tilted from each other for the compound. The ring breathing mode of phenyl rings are assigned at the 1096 cm⁻¹ theoretically. MEP and ALIE surfaces and RDFs show that the nitrogen atoms N₂₃ for the compound. Frontier Molecular Orbital Analysis reveals that all the chemical descriptors are not different and the chemical descriptors are not different and the substitution change in the title compounds does not affect these values.

CHAPTER 6

Spectroscopic analysis , Molecular Docking and DFT calculation on 1-Hydroxy-2-(4-hydroxyphenyl)-4,5-dimethyl-imidazol 3 oxide

This compound is a derivative of imidazole derivative . Spectroscopic , DFT , molecular dynamics and molecular docking of the derivative can be studied

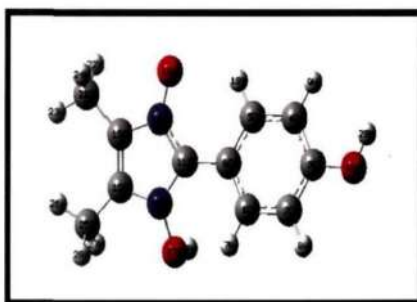


Figure 6.1 structure of 1-hydroxy-2-(4-hydroxyphenyl)-4,5-dimethyl-imidazol 3 oxide

- The spectroscopic and reactive properties of newly synthesized 1-hydroxy-2-(4-hydroxyphenyl)-4,5-dimethyl-imidazol 3 oxide was investigated.
- Using potential energy distribution calculation FT-IR and NMR spectra were measured and using chemical shift the theoretically obtained data was compared.
- By analyzing the frontiers molecular orbitals global reactivity properties has been obtained.
- By analyzing the charge distribution ,ionization energies and fukui functions the local reactivity properties have been investigated.
- To understand the stability of molecular NBO analysis was employed.
- Hyperpolarizability has been calculated in order to assess the nonlinear optical properties of title molecules.
- The calculation of bond dissociation energies and radial distribution functions gives the sensitivity towards autoxidation and hydrolysis mechanisms of the compound respectively.
- In order to determine the pharmaceutical potential of the investigated molecule, molecular docking study was performed.
 - Calculation of the title compound were carried out with Gaussian09 program B3LYP/6-31++G(d) (6D, 7F) basis set to predict the molecular structure and vibrational frequencies.

- Molecular geometry of compound was fully optimized by Berny's optimization algorithm using redundant internal coordinates.
- Using the analytic second derivatives harmonic vibrational frequencies are calculated to confirm the convergence to minima on the potential surface.
- The ¹H-NMR data were obtained from the DFT method using basis set B3LYP/6-31++G(d) (6D,7F) .
- The HOMO-LUMO energy is calculated by B3LYP/6-31++G(d)(6D,7F) method.

EXPERIMENTAL DETAILS

1-hydroxy-2-(4-hydroxyphenyl)-4, 5-dimethyl-imidazole 3-oxide was synthesized through a solvent free procedure. 2 mmole (0.202g) of 3-(hydroxyimino) butan-2-one was mixed with 2 mmole(0.272g) of 4-hydroxybenzaldehyde and thoroughly ground with 10 mmole (0.695g) of hydroxylamine hydrochloride in anagate mortar and pestle for a period of ca.3 minutes during which it melts and then getshardened slowly .The mixture was then transferred to a test tube and heated in an oil bath maintained at 110-120°C when it started to melt . Constant shaking for another 7 minutes yielded the product which remained in the melt form even at room temperature. On completion of the reaction, checked by thin layer chromatography (TLC) using 0.25 mm Merck Aluminium silica gel 60-F254 precoated plates, additional of 5 ml of diethyl ether precipitated the product. The water insoluble product was then washed with water and ethyl acetate to get the pure products.

The FT-IR spectrum was record using KBr pellets on a DR/Jasco FT-IR 6300 spectrometer. The FT-Raman spectrum was obtained on a Bruker RFS100/s, Germany .For excitation of the spectrum the emission of Nd:YAG laser was used ,excitation wavelength 1064 nm ,maximal power 150mW , measurement on solid sample . The ¹H NMR was recorded in dmsO-d₆ on a brukeravance 300 spectrometer .The electrospray mass spectrum was recorded on a MICROMASS QUATTRO II triple quadruple mass spectrometer .The ESI capillary was set at 3.5 kV and cone voltage was 40 V .ESI m/z found for C₁₁H₁₂N₂O₃ : C,59.99; H,5.49; N,12.72 ; O,21.80; Found : C,59.52; N,12.54; O,21.99.

RESULT

IR and Raman spectra

IR and Raman band and calculated frequencies and assignments are observed. The phenyl ring and imidazole ring are designed as ph I and ringII and the experimentally observed IR, Raman bands are compared with the values given by B3LYP/6-31++G (d) (6D,7F) values .

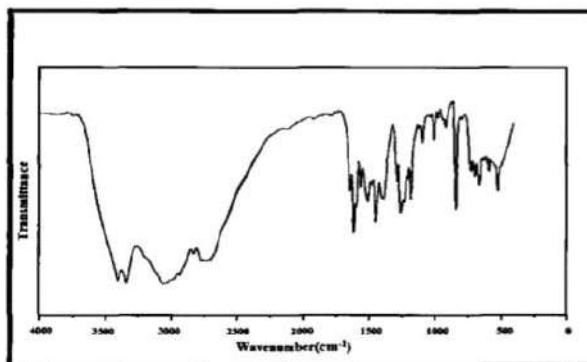


Figure 6.2 FT-IR Spectra of 1-hydroxy-2-(4-hydroxyphenyl)-4,5-dimethyl-imidazol 3 oxide

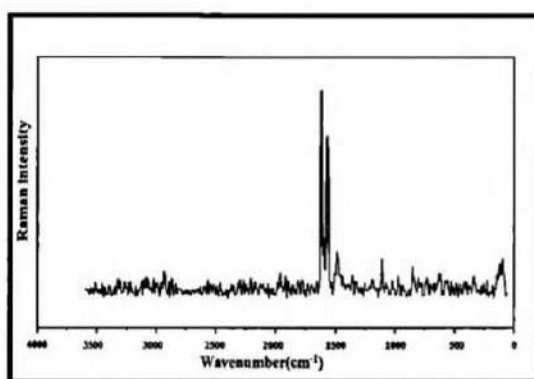


Figure 6.3 FT Raman spectrum of 1-hydroxy-2-(4-hydroxyphenyl)-4,5-dimethyl-imidazol 3 oxide

Geometric Parameter

The optimized molecular structure of the compound was determined by using Gaussian09 program. The c-c bond length of C₆-C₁₁ (1.453 Å) is greater than that of C₅-C₆ (1.411 Å) and C₁-C₆ (1.4138 Å) because of delocalization of electron density of C₆-C₁₁ with the ring in which N-O is substituted. Also the slight difference in the bond length of C₂-C₃ (1.3994 Å) C₃-C₄ (1.3986 Å) is due to the presence of -OH group in the neighbourhood. The C-N bond lengths C₁₁-N₁₄ (1.356 Å), C₁₁-N₁₅ (1.3841 Å), N₁₂-N₁₅ (1.3833 Å) and C₁₃-N₁₄ (1.4032 Å) are different because of the difference in their environment and assume a double bond character in C₁₁-N₁₄. The bond angle between C₆-C₁₁-N₁₄ (127.5 Å) indicates the better delocalization in the former. Also N₁₁-N₁₄-C₁₃ (110 Å) and C₁₁-N₁₅-C₁₂ (111.4 Å) indicates slightly electronegative property of oxygen atom.

Frontier Molecular Orbital analysis

HOMO (highest occupied molecular orbital) and LUMO (lowest occupied molecular orbital) are very important parameters. The eigen values of HOMO and LUMO and their energy gap are -7.91, -5.11 and 2.80 respectively, they reflect the biological activities of the molecule. A molecule having a small frontier gap is more polarizable and is generally associated with a high chemical reactivity and the low kinetic stability. HOMO which can be thought as the outer orbit containing electron tends to give these electron as an electron donor and hence the ionization potential is directly related to energy of HOMO. LUMO can accept electrons and LUMO energy is directly related to electron affinity. The chemical potential, global hardness and electrophilicity will pave the way to understand the structure and reactivity of the molecule.

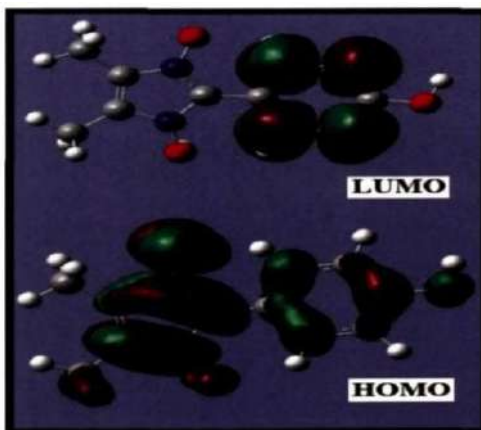


Figure 6.4 HOMO and LUMO plot of 1-hydroxy-2-(4-hydroxyphenyl)-4,5-dimethyl-imidazol 3 oxide

Molecular Electrostatic Potential (MEP)

MEP is very useful descriptor in understanding sites for electrophilic attack and nucleophilic reactions and for the study of biological recognition process. It is useful in the investigation in the molecular structure with its physicochemical property relationship. To predict reactive sites of electrophilic and nucleophilic attacks for the investigated molecule, MEP at the B3LYP/6-3++G (d) (6D,7F) optimized geometry s calculated.



Figure 6.5 Molecular electrostatic potential of 1-hydroxy-2-(4-hydroxyphenyl)-4,5-dimethylimidazol 3 oxide

¹H NMR Spectrum

Experimental spectrum data of compound in DMSO is obtained at 300MHz . B32YP/GIAO was used to calculate the absolute isotropic chemical shielding of the compound.

Non -Linear Optical Property

Nonlinear optics deals with the interaction of applied electromagnetic field in various material to generate new electromagnetic fields , altered in frequencies , phase or other physical properties . Organic molecules are able to manipulate photonic signals efficiently are of importance in technologies e in technologies such as optical communication, optical computing and dynamic image processing [Kolinsky 1992; Eaton 1991]. In this context, the dynamic first hyperpolarizability of the title compound is also calculated in the present study. The first hyperpolarizability (β_0) of this novel molecular system is calculated using B3LYP/6-31++G (d) (6D, 7F) method, based on the finite field approach. The calculated first hyperpolarizability of the title compound is 4.39×10^{-30} esu, which is 33.76 times that of standard NLO material urea (0.13×10^{-30} esu) . The reported value of hyperpolarizability of similar derivative is 4.51×10^{-30} esu and the title compound is an attractive object for further studies of nonlinear optical properties. The average second hyperpolarizability has been calculated by using the following expression,

$$\gamma = 1/5 (\gamma_{xxxx} + \gamma_{yyyy} + \gamma_{zzzz} + 2\gamma_{xxyy} + 2\gamma_{xxzz} + 2\gamma_{yyzz})$$

The amount of charge transfer for the molecule depends on the nature of the end group of the molecule. Increase of π -conjugated chain length in organic molecules, in general, enhances the magnitude of hyperpolarizability. The calculated value of Y_{av} for the title compound is $-0.903634 \times 10^{-36}$ esu , The larger component of second hyperpolarizability is associated with the larger ground state polarization which leads to strong electronic coupling between the ground and the low lying excited state. Thus the present investigation provides a new route to design high performance NLO material .

Molecular Spectrum

High resolution crystal structure of CDK inhibitors was downloaded from the RSCB protein bank website with PDB: ID 2XMY .All docking calculations were performed using Auto Dock –Vina software .the 3D crystal structure of CDK inhibitor was obtained from protein data bank. The Auto Dock Tool (ADT) graphical user interface was used to calculate kollaman charges. Partial charges was calculated by Geistenger method . .The docking protocol predicted the same conformation as was present in the crystal structure . Amongst the docked conformations ,one which binds well at the active site was analysed for detailed interactions in Discover Studio Visualizer 4.0 software .

Compound	1 st hyperpolarizability ($\times 10^{-30}$ esu)	2 nd hyperpolarizability ($\times 10^{-36}$ esu)
HIO1	4.39	-0.90

The Global Reactive Description

COMPOUND	I(ev)	χ (ev)	η (ev)	μ (ev)	ω (ev)
1-hydroxy-2-(4-hydroxyphenyl)-4,5-dimethyl-imidazole-3-oxide	6.91	3.46	6.91	-3.46	1.73

CONCLUSION

The vibrational spectroscopic studies of 1-hydroxy-2-(4-hydroxyphenyl)-4,5-dimethyl-imidazole 3-oxide were reported experimentally and theoretically. Potential energy distribution of normal modes of vibration was done using GAR2PED program. The ring stretching mode in IR and Raman are evidence for charge transfer interaction between the donor and the acceptor group through the π system. This along with lowering of HOMO-LUMO band gap supports for the bioactivity of the molecule. NBO analysis predict a strong intra-molecular hyper conjugative interaction of (C₁₁-N₁₄) from N₁₅ of n₁(N₁₅), (C₁₁-N₁₄) from O₁₆ of n₁(O₁₆), (C₁₃-N₁₄) from O₁₆ of n₂(O₁₆), (C₁₁-N₁₄) from O₁₆ of n₃(O₁₆), (C₁₁-N₁₅) from O₁₇ of n₁(O₁₇), (C₁₂-N₁₅) from O₁₇ of n₂(O₁₇), (C₃-C₄) from O₁₉ of n₁(O₁₉), (C₃-C₄) from O₁₉ of n₂(O₁₉). MEP predicts the most reactive part in the molecule. The calculated first hyperpolarizability is comparable with the reported values of similar derivatives and is an attractive object for fixture studies in nonlinear optics. In addition the calculated NMR results are in good agreement with experimental data. From the molecular docking, the title compound might exhibit inhibitory activity against CDK inhibitor.

CHAPTER 7

COMPARITIVE STUDY AND CONCLUSION

This chapter gives the comparative study and the conclusion of the given compound.

COMPARISION

Comparision of Non Linear Optical Properties (NLO)

The orientation of charge levels among the molecules site in the compound are usually measured as different orders such as first and second order. Here the five given compounds have good non-linear optical properties. The values of first and second hyperpolarizability of the compounds are calculated using Gaussian09 software. The first and second hyperpolarizability of the compound can be measured and compared with each other. Here the compound 1-[2-(2-hydroxy-3-methoxy-5-(4-methoxyphenylazo)benzaldeneamino)ethyl]-3-methyl-3H-imidazole having highest value and 1-(4-methoxyphenyl)-1H-imidazole having least value for the first hyperpolarizability. The change in the hyperpolarizability of the compound shows the difference in their non-linear optic properties. The compound 1-butyl-2-(4-hydroxyphenyl)-4,5-dimethyl-imidazole-3-oxide has high second polarizability. The hyperpolarizability values of the compounds are given below.

COMPOUND	FIRST HYPERPOLARIZABI LITY ($\times 10^{-30}$)esu	SECOND HYPERPOLARIZABI LITY ($\times 10^{-36}$)esu
1-butyl-2-(4-hydroxyphenyl)-4,5-dimethyl-imidazole-3-oxide	3.61	1.30
1-hydroxy-2-(4-hydroxyphenyl)-4,5-dimethyl-imidazole-3-oxide	4.39	-0.90
1-[2-(2-hydroxy-3-methoxy-5-(4-methoxyphenylazo)benzaldeneamino)ethyl]-3-methyl-3H-imidazole	40.14	-3.02
2-chloro-1-(4-methoxyphenyl)-4,5-dimethyl-1H-imidazole	2.99	-1.54
1-(4-methoxyphenyl)-1H-imidazole	1.75	-

Comparison of HOMO LUMO Gap

HOMO-LUMO band gap is a basic parameter in deciding the atomic transport effect such as chemical reactivity of a substance and kinetic stability of a molecule, since it is a measure of electron conductivity. The frontier orbital energies and energy gaps between HOMO and LUMO were calculated for the given compound. Frontier orbital theory tells us that the HOMO (highest occupied molecular orbit) and the LUMO(lowest occupied molecular orbit) play a dominant role in chemical reaction. The gap between HOMO and LUMO and frontier orbital energy gap shows the interaction of that molecule with other species. This orbital energy gap helps to differentiate chemical stability of the molecule. The larger HOMO-LUMO gaps always refers to the highest kinetic stability and lower chemical reactivity. The compound 1-(4-methoxyphenyl)-1H-imidazole has always has higher kinetic stability and lower chemical reactivity, because it has higher energy gap.

HOMO-LUMO Energy Values

COMPOUND	HOMO(ev)	LUMO(ev)	ENERGY GAP(ev)
1-butyl-2-(4-hydroxyphenyl)-4,5-dimethyl-imidazole-3-oxide	-7.99	-5.11	2.88
1-hydroxy-2-(4-hydroxyphenyl)-4,5-dimethyl-imidazole-3-oxide	-7.91	-5.11	2.80
1-[2-(2-hydroxy-3-methoxy-5-(4-methoxyphenylazo)benzaldehydeamino)ethyl]-3-methyl-3H-imidazole	-7.822	-5.441	2.381
2-chloro-1-(4-methoxyphenyl)-4,5-dimethyl-1H-imidazole	-7.546	-4.577	2.971
1-(4-methoxyphenyl)-1H-imidazole	-6.27(gas phase) -6.32(water phase)	-1(gas phase) -0.90(water phase)	5.21(gas phase) 5.42(water-phase)

Comparison of Global Reactivity Description

Global reactivity descriptors of imidazole derivative compounds are calculated. The chemical reactivity descriptors like ionization potential (I), Electronegativity(χ), global hardness(η), chemical potential(μ), global electrophilicity(ω) have been proposed for understanding various aspects of pharmacological compounds. Since these are used we can compare the reactivity of the compounds. The low ionization of the compounds show high inhibition efficiency. The ionization energy of 1-(4-methoxyphenyl)-1H-imidazole indicates high inhibition efficiency. The chemical hardness is less in 1-[2-(2-hydroxy-3-methoxy-5-(4-methoxyphenylazo)benzaldehydeamino)ethyl]-3-methyl-3H-imidazole .

Global Reactive Description

COMPOUND	I(ev)	χ (ev)	η (ev)	μ (ev)	ω (ev)
1-butyl-2-(4-hydroxyphenyl)-4,5-dimethyl-imidazole-3-oxide	6.43	3.21	3.201	-3.21	1.60
1-hydroxy-2-(4-hydroxyphenyl)-4,5-dimethyl-imidazole-3-oxide	6.91	3.46	6.91	-3.46	1.73
1-[2-(2-hydroxy-3-methoxy-5-(4-methoxyphenylazo)benzaldehydeamino)ethyl]-3-methyl-3H-imidazole	7.822	6.63	1.191	-6.632	18.465
2-chloro-1-(4-methoxyphenyl)-4,5-dimethyl-1H-imidazole	7.546	6.061	1.486	-6.061	12.36
1-(4-methoxyphenyl)-1H-imidazole	6.27(gas phase) 6.32(water phase)	3.64(gas phase) 2.71(water phase)	2.64(gas phase) 2.71(water phase)	-3.64(gas phase) -3.61(water phase)	2.51(gas phase) 2.41(water phase)

Thus 1-butyl-2-(4-hydroxyphenyl)-4,5-dimethyl-imidazole-3-oxide is found to be most reactive among us all whereas 1-[2-(2-hydroxy-3-methoxy-5-(4-methoxyphenylazo)benzaldehydeamino)ethyl]-3-methyl-3H-imidazole .

IR AND RAMAN Spectra

The IR and Raman spectrum of 1-butyl-2-(4-hydroxyphenyl)-4,5-dimethyl-imidazole-3-oxide, 1-hydroxy-2-(4-hydroxyphenyl)-4,5-dimethyl-imidazole-3-oxide, 1-[2-(2-hydroxy-3-methoxy-5-(4-methoxyphenylazo)benzaldehydeamino)ethyl]-3-methyl-3H-imidazole, 2-chloro-1-(4-methoxyphenyl)-4,5-dimethyl-1H-imidazole were studied. The experimental values are in good agreement with the observed value.

Molecular Electrostatic Potential

MEP is a very useful descriptor in understanding the sites for electrophilic attack and nucleophilic region and for the study of biological recognition processes. The negative region of MEP related to the electrophilic reactivity and positive region to nucleophilic reactivity. For the compound 1-butyl-2-(4-hydroxyphenyl)-4,5-dimethyl-imidazole-3-oxide the negative charge covers the N₁₄-O₂₄. The positive region is over the OH group. For 1-hydroxy-2-(4-hydroxyphenyl)-4,5-dimethyl-imidazole-3-oxide, the negative charge covers the N₁₄-O₁₆ and phenyl ring. The positive region is over the OH group. For 1-[2-(2-hydroxy-3-methoxy-5-(4-methoxyphenylazo)benzaldehydeamino)ethyl]-3-methyl-3H-imidazole, the electrophilic region covers the rings R₁, R₂ and oxygen atoms. For nucleophilic region covers ring R₃. For 2-chloro-1-(4-methoxyphenyl)-4,5-dimethyl-1H-imidazole, the hydrogen atom belongs to the methyl groups and benzene rings have the highest MEP values. For 1-(4-methoxyphenyl)-1H-imidazole, the electrophilic region is localized on the N₃ atom in the imidazole ring. Especially in C atom and H atoms in the methoxy group and the other H atoms are localized in the less positive potential region. The atom in the methoxy group and the carbon atom in the imidazole and phenyl ring are in the less electronegative region.

CONCLUSION

The vibrational frequencies of various bonded atoms and functional groups of compounds were studied from the recorded FT-IR and FT-Raman spectra. For 1-hydroxy-2-(4-hydroxyphenyl)-4,5-dimethyl-imidazole 3-oxide, the suitable set is 6-31++G(d) (6D,7F). For 1-butyl-2-(4-hydroxyphenyl)-4,5-dimethyl-imidazole 3-oxide the suitable set is 6-311++G(d,p) (5D,7F). For 1-[2-(2-hydroxy-3-methoxy-5-(4-methoxyphenylazo)benzaldehydeamino)ethyl]-3-methyl-3H-imidazole the suitable set is B3LYP with 6-311++G(d,p). For 2-chloro-1-(4-methoxyphenyl)-4,5-dimethyl-1H-imidazole then

suitable set is 6-31G(d,p). For 1-(4-methoxyphenyl)-1H imidazole the suitable set is 6-311++G(d,p). These computationally obtained wave number agrees with that of the experiment result. The global reactivity descriptors ionization potential, electronegativity, chemical potential and global hardness of the molecule were also investigated. The first high polarizability values is observed to be high for 1-(2-(2-hydroxy-3-methoxy-5-(4-methoxyphenylazo)benzaldehydeamino)ethyl)-3-methyl-3H-imidazole, which is also evident from the global hardness (η) as it being a measure of how difficult the molecule is polarizable as all the molecule posses non-centro srymmetry, they are exhibit good non-linear response. The NBO analysis predicted the intra molecular hyperconjugative interaction and stabilization energy associated with the donor-acceptor interactions with each molecules. The molecular electrostatic potential plot predict the negative electrostatic potential and positive electro static potential. The molecular docking studies performed using Auto Dock Vina on 1-hydroxy-2-(4-hydroxyphenyl)-4,5-dimethyl-imidazole 3-oxide and 1-butyl-2-(4-hydroxyphenyl)-4,5-dimethyl-imidazole 3-oxide and 1-(2-(2-hydroxyphenylazo)benzaldehydeamino)ethyl)-3-methyl-3H-imidazole and 1-(4-methoxyphenyl)-1H-imidazole had shown that they have activity against CDK inhibitor. The compound (2-chloro-1-(4-methoxyphenyl)-4,5-dimethyl-1H-imidazole) which exhibit inhibitory activity against dimethylallyl transferase inhibitor.

REFERENCE

1. Spectroscopic,DFT,molecular dynamics and molecular docking study of 1-butyl-2-(hydroxyphenyl)-4,5-dimethyl-imidazole3-oxide
2. KB Benzon,YS Mary,HT Varghese,CY Panicker,S Armakovic,Christian Van Alsenoy,Kiran Pradhan,Ashis Kumar Nandha , spectrochemical alkha part A
3. Spectroscopic and theoretical characterization of 2-(4-methoxyphenyl)-4,5-dimethyl-1H-imidazole 3-oxide
4. K B Benzon , Hema Theresa Varghese,C.Yohannan Panicker,Kiran Pradhan,Biprash Kumar Tiwary,Ashis Kumar Nanda,C.Van Alsenoy
5. Spectroscopic analysis and molecular docking of imidazole derivatives and investigation of its reactive properties by DFT and molecular dynamics simulations.
6. (Mossaraf Hossain,Renjith Thomas,Y.Sheena,Resmi K.s.)
7. Conformational analysis and quantum descriptors of two new imidazole derivatives by experimental, DFT, AIM, molecular docking studies and adsorption activity on graphene Veena (S. Kumar,Y. Sheena Mary,Kiran Pradhan , Dhiraj Brahman , Y. Shyma Mary, Goncagül Serdaroglu Ali Shokuhi Rad , M.S. Roxy)
8. M Smitha , Y S Mary , M . Hossain , K S . Resmi , S. Armakovic , S J Armacovic , R. Pavithran , A.K Nanda , C. Van Alsenoy , Two novel imidazole derivatives Combined experimental and computational study , J Mol . Struct . 1173 (2018) 221–239
9. V S Kumar , Y. S. Mary, K Pradan , D. Brahman , Y .S Mary , R. Thomas , M.S.Roxy , C .Van Alsenoy , Synthesis, spectral properties, chemical descriptors and light harvesting studies of a new bioactive azo imidazole compound , J .Mol.Struct. 1199 (2020) 127035 .
10. C T Lee , W.T.Yang , R .G .Paar , Development of the Colle –Salvetti correlation energy formula into a functional of the electron density , phys.Rev .37B (1988) 785 –789 .
11. R.G.Parr , Y.Yang ,Density Functional Theory of Atoms and Molecules , 1989 . Oxford , New York
12. A.D.Becke , Density functional thermochemistry .||| . The role of exact exchange , J.Chem . Phys 98 (1993) 5648 –5652

13. P. Pulay, G.H. Fogarasi, F. Pang, J.E. Boggs, Systematic ab initio gradient calculation of molecular geometries, force constants and dipole moment derivatives, *J. Am. Chem. Soc.* 101 (1979) 2550–256
14. J. M. L. Martin, C. Van Alsenoy, GAR2PED, University of Antwerp, Antwerp, 1995.
15. A. Lagunin, A. Stepanchikova, D. Filimonov, V. Poroikov, PASS: prediction of activity spectra for biologically active substances, *Bioinformatics* 16 (2000) 747-748.
16. F.C. Torres, M.E. García-Rubiño, C. Lozano-López, D.F. Kawano, V.L. Eifler-Lima, G.L. von Poser, J.M. Campos, Imidazoles and benzimidazoles as tubulin- modulators for anti-cancer therapy. *Curr. Med. Chem.* 22 (11) (2015) 1312-1323.
17. F. Bellina, N. Guazzelli, M. Lessi, C. Manzini, Imidazole analogues of resveratrol: synthesis and cancer cell growth evaluation, *Tetrahedron* 71 (2015) 2298-2305.
18. D. Pechalrieu, C. Etievant, P.B. Arimondo, DNA methyltransferase inhibitors in cancer: from pharmacology to translational studies, *Biochem. Pharmacol.* 129 (2017) 1-13.
19. V. Singh, P. Sharma, N. Capalash, DNA methyltransferase-1 inhibitors as epigenetic therapy for cancer, *Curr. Cancer Drug Targets* 13 (2013) 379-399.
20. O. Trott, A.J. Olson, AutoDock Vina: improving the speed and accuracy of docking with a new scoring function, efficient optimization and multi- threading. *J. Comput. Chem.* 31 (2010) 455-461.
21. N.G. Haress, F. Al-Omary, A.A. El-Emam, Y.S. Mary, C.Y. Panicker, A.A. Al-Saadi, J.A. War, C. Van Alsenoy, Spectroscopic investigation (FT-IR and FT-Raman), vibrational assignments, HOMO-LUMO analysis and molecular docking study of 2-(Adamanan-1-yl)-5-(4-nitrophenyl)-1,3,4-oxadiazole, *Spectrochim. Acta* 135 (2015) 973-983.
22. B. Kramer, M. Rarey, T. Lengauer, Evaluation of the FlexX incremental construction algorithm for protein ligand docking, *Proteins Struct. Funct. Genet.* 37 (1999) 228-241.
23. Celik S, Alp M, Yurdakul S (2020) A combined experimental and theoretical study on vibrational spectra of 3-pyridyl methyl ketone. *Spectrosc Lett* 53(4):234-248. <https://doi.org/10.1080/00387010.2020.1734840>
24. Gunduz SK, Bicak B, Celik S, Akyuz S, Ozel AE (2017) Structural and spectroscopic investigation on antioxidant dipeptide, L-Methionyl-L-Serine: A combined experimental and DFT study. *J Mol Struct.* <https://doi.org/10.1016/j.molstruc.2017.02.075>
25. Kumar S, Radha A, Kour M, Kumar R, Chouaih A, Pandey SK (2019) DFT studies of disubstituted diphenyldithiophosphates of nickel(II): Structural and some spectral parameters. *J Mol Struct* 1185:212-218. <https://doi.org/10.1016/j.molstruc.2019.02.105>

26. T. Zhang, X. Wei, Y. Zuo, J. Chao, An efficient measure to improve the NLO performance by point charge electric field, *Optik* 182 (2019) 295-302.
27. R.I. Al-Wabli, K.S. Resmi, Y.S. Mary, C.Y. Panicker, M.I. Attia, A.A. El-Emam, C. Van Alsenoy, Vibrational spectroscopic studies, Fukui functions, HOMO-LUMO, NLO, NBO analysis and molecular docking study of (E)-1-(1,3-benzodioxol-5-yl)-4,4-dimethylpent-1-en-3-one, a potential precursor to bioactive agents, *J. Mol. Struct.* 1123 (2016) 375-383.
28. A.E. Reed, P.V.R. Schleye, The anomeric effect with central atoms other than carbon. 2. Strong interactions between nonbonded substituents in mono- and polyfluorinated first- and second-row amines, *FnAHmNH₂*, *Inorg. Chem.* 27 (1988) 3969-3987.
29. G.M. Morris, R. Huey, W. Lindstrom, M.F. Sanner, R.K. Belew, D.S. Goodsell, A.J. Olson, Autodock4 and AutoDock Tools 4: automated docking with selective receptor flexibility, *J. Comput. Chem.* 16 (2009) 2785-2791.
30. A. Lagunin, A. Stepanchikova, D. Filimonov, V. Poroikov, PASS: prediction of activity spectra for biologically active substances, *Bioinformatics* 16 (2000) 747-748.
31. P.W. Rose, B. Beran, C. Bi, W.F. Bluhm, D. Dimitropoulos, D.S. Goodsell, A. Prlic, M. Quesada, G.B. Quinn, J.D. Westbrook, J. Young, The RCSB protein data bank: redesigned web site and web services, *Nucleic Acids Res.* 39 (2010) D392-D401. [89] Discovery Studio 4.5 Guide, Accelrys Inc., San Diego, 2009. <http://www.accelrys.com>.
32. G.M. Morris, D.S. Goodsell, R.S. Halliday, R. Huey, W.E. Hart, R. Belew, A.J. Olson, Automated docking using a Lamarckian genetic algorithm and an empirical binding free energy function, *J. Comput. Chem.* 19 (1998) 1639-1662.
33. S. Armaković, S.J. Armaković, J.P. Setrajčić, IJ. Setrajčić, Active components of frequently used β -blockers from the aspect of computational study. *J. Mol. Model.* 18 (2012) 4491-4501.
34. K. Pradhan, B.K. Tiwary, M. Hossain, R. Chakraborty, A.K. Nanda, A mechanistic study of carbonyl activation under solvent free conditions, evidence drawn from the synthesis of imidazoles, *RSC Adv.* 6 (2016) 10743-10749. 56.
35. Schrodinger Release 2017-4: MacroModel, Schrödinger, LLC, New York, NY, 2017, p. 2017.
36. E. Harder, W. Damm, J. Maple, C. Wu, M. Reboul, J.Y. Xiang, L. Wang, D. Lupyan, M.K. Dahlgren, J.L. Knight. OPLS3: a force field providing broad coverage of drug-like small molecules and proteins, *J. Chem. Theor. Comput.* 12 (2015) 281-296.
37. D. Shivakumar, J. Williams, Y. Wu, W. Damm, J. Shelley, W. Sherman, Prediction of absolute solvation free energies using molecular dynamics free energy perturbation and the OPLS force field, *J. Chem. Theor. Comput.* 6 (2010) 1509-1519.
38. W.L. Jorgensen, D.S. Maxwell, J. Tirado-Rives, Development and testing of the OPLS all-atom force field on conformational energetics and properties of organic liquids, *J. Am. Chem. Soc.* 118 (1996) 11225-11236 0] W.L. Jorgensen, J. Tirado-Rives, The OPLS [optimized potentials for liquid.simulations potential functions for proteins, energy minimizations for crystals of cyclic peptides and crambin, *J. Am. Chem. Soc.* 110 (1988) 1657-1666.

39. A.D. Bochevarov, E. Harder, T.F. Hughes, J.R. Greenwood, DA. Braden, D.M. Philipp, D. Rinaldo, M.D. Halls, J. Zhang, R.A. Friesner, Jaguar: a high- performance quantum chemistry software program with strengths in life and materials sciences, *Int. J. Quant. Chem.* 113 (2013) 2110-2142. 42) Schrödinger Release 2017-4: Jaguar, Schrödinger, LLC, New York, NY, 2017,p. 2017.
40. A.D. Becke, Density-functional thermochemistry. III. The role of exact ex- change, *J. Chem. Phys.* 98 (1993) 5648-5652.
41. M.J. Frisch, G.W. Trucks, H.B. Schlegel. G.E J.R. Cheeseman, G. Scalmani, V. Barone, B. Mennucci, G.A. Petersson, H. Nakatsuji, M. Caricato, X. LL. H.P. Hratchian, A.F. Izmaylov, J Bloino, G. Zheng. JL. Sonnenberg, M. Hada, M. Ehara, K. Toyota, R. Fukuda, J. Hasegawa, M. Ishida, T. Nakajima, Y. Honda, O. Kitao, H. Nakai, T. Vreven, J.A. Montgomery Jr. J.E. Peralta, F. Ogliaro, M. Bearpark, JJ. Heyd, E. Brothers, K.N. Kudin, V.N. Staroverov, T. Keith, R. Kobayashi, J. Normand, K. Raghavachari, A. Rendell, J.C. Burant, S.S. Iyengar. J. Tomasi, M. Cossi, N. Rega, J.M. Millam, M. Klene, J.E. Knox, J.B. Cross, V. Bakken, C. Adamo, J. Jaramillo, R. Gomperts, R.E. Stratmann, O. Yazyev, AJ. Austin, R. Cammi, C. Pomelli, J.W. Ochterski, R.L. Martin, K. Morokuma, V.G. Zakrzewski, G.A. Voth, P. Salvador. J.J. Dannenberg. S. Dapprich, A.D. Daniels, O. Farkas, JB. Foresman, J.V. Ortiz, J. Cioslowski, D.J. Fox, Gaussian 09, Revision 8.01. Gaussian, Inc., Wallingford CT, 2010,
42. HJ. Berendsen, J.P. Postma, W.F. van Gunsteren, J. Hermans, Interaction models for water in relation to protein hydration, in: *Intermolecular Forces*, Springer, 1981, pp. 331-342.
43. Schrödinger Release 2017-4: Maestro, Schrödinger, LLC. New York, NY, 20
44. K.B. Benzon, H.T. Varghese, C.Y Panicker, K. Pradhan, B K. Tiwary, A, K Nandha, C. Van Alsenoy, Spectroscopic investigation (FT-IR and FT-Raman), vibrational assignments, HOMO-LUMO, NBO, MEP analysis and molecular docking study of 2-(4-hydroxyphenyl)-4,5-dimethyl-1H-imidazole 3-oxide, *Spectrochim, Acta* 146 (2015) 307-322.
45. A. Chandran, H.T. Varghese, YS. Mary, C.Y. Panicker, T.K. Manojkumar, C. Van Alsenoy, G. Rajendran, Vibrational spectroscopic and quantum chemical calculations of (E)-N-carbamimidoyl-4-((naphthalene-1-yl)amino)benzene fonamide, *Spectrochim. Acta* 87 (2012) 29-39.
46. N.P.G. Roeges, *A Guide to the Complete Interpretation of Infrared Spectra of Organic Structures*, John Wiley and Sons Inc., New York, 1994.
47. CY. Panicker, H.T. Varghese, K.C. Mariamma, K. John, S. Mathew, J. Vinsova, C. Van Alsenoy, Y.S. Mary, Spectroscopic investigations and Computational study of 2-[Acetyl (4-bromophenyl) carbamoyl]-4-chlorophenyl acetate, *J. Raman Spectrosc.* 41 (2010) 707-716.
48. N.B. Colthup, LH. Daly, S.E. Wiberly, *Introduction of Infrared and Raman Spectroscopy*, Academic Press, New York, 1975.
49. R.M. Silverstein, G.C. Bassler, T.C. Morrill, *Spectrometric Identification of Organic Compounds*, fifth ed., John Wiley and Sons Inc.. Singapore. 1991.
50. AS, El-Azab, YS. Mary, C.Y. Panicker, A.A.M. Abdel-Aziz, M.A. El-Sherbeny, C. Van alsenoy. DFT and experimental (FT-IT and FT-Raman) investigation of

51. <https://www.sciencedirect.com/topics/chemistry/imidazole>
52. <https://www.sciencedirect.com/science/article>
53. <https://study.com/learn/lesson/spectroscopy-typesandtechniques>
54. <https://www.google.com/wikipedia/spectroscopy&usq>
55. <https://en.m.wikipedia.org/wiki/spectroscopy>

ST.JOHNS COLLEGE

ANCHAL

Project report

Submitted to the University of Kerala for requirement of the degree of

Bachelor of Science in Physics



“Determination of refractive index of different liquids using Newton`s ring method”

Submitted by

Group members

Name:	Reg. No.
Aliya Fathma	23021138005
Ganesh H Nair	23021138007
Haridarshan R	23021138008

Under the supervision of

Dr. Benzon K B

Assistant professor

Department of physics

St Johns College,

Anchal

2021-24

CERTIFICATE

Dr Benzon K B
Assistant Professor & Head
Project Guide
Faculty of Physics
St. John's College
Anchal, Kollam

This is to certify that our project report of **“Determination of refractive index of different liquids using Newton's ring method”** submitted by **Aliya Fathma (23021138005), Ganesh H Nair (23021138007), Haridarshan R (23021138008)** in partial fulfillment of the requirement for the award of Degree of Bachelor of Science in Physics is based on their original work under my guidance. It is further certified

Anchal, Kollam

Signature:

Date:

DECLARATION

We hereby declare that this project entitled “Determination of refractive Index of different liquids using the Newton`s Ring method” is a group work carried out by us under the supervision and the guidance of **Dr Benzou K B**, Assistant Professor, Department of Physics, St Johns College, Anchal. It has not been included in any other project submitted previously for the award of any degree.

Anchal

Date:

Aliya Fathma (23021138005)

Ganesh H Nair (23021138007)

Haridarshan R (23021138008)

AKNOWLEDGEMENT

Our project would have not been a success without the grace of the almighty God. On the successful completion of the project work, we would like to share our sincere gratitude to all those who assisted us directly and indirectly.

We take this opportunity to express our deepest sense of attitude to our guide **Dr Benzon KB**, Assistant professor and Head of Department of Physics, St John's College Anchal, Kollam, for this valuable guidance throughout this project work.

We sincerely acknowledge our gratitude to our principal **Dr Nisha Thomas, St John's College Anchal, Kollam** for having provided the facilities to complete this work. We sincerely thank the authorities of St John's College Anchal, Kollam for allowing us to carryout our project work in their prestigious organization. We also extend our thanks to all our faculty members and fellow students for their valuable assistance during the entire period of this project.

Aliya Fathma (23021138005)

Ganesh H Nair (23021138007)

Haridarshan R (23021138008)

Anchal

Date:

CONTENTS

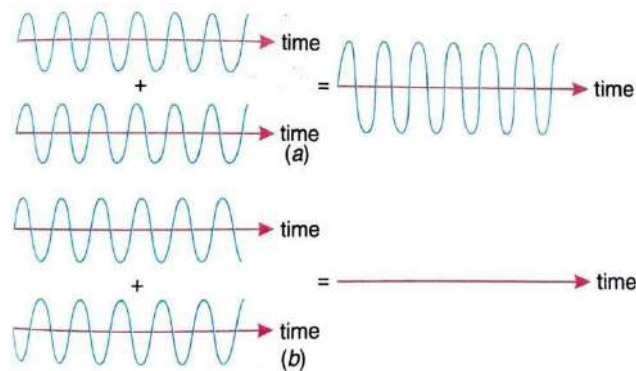
Heading	Page No.
1. INTRODUCTION	
1.1 INTERFERENCE	8
1.2 YOUNG'S DOUBLE SLIT EXPERIMENT	10
1.3 OPTICAL PATH DIFFERENCE	11
1.4 BRIGHT FRINGES	12
1.5 DARK FRINGES	13
1.6 CONDITIONS FOR INTERFERENCE (a) CONDITION FOR SUSTAINED INTERFERENCE (b) CONDITION FOR FORMATION OF DISTINCT FRINGE PATTERN	14
1.7 INTERFERENCE BY A PLANE PARALLEL FILM WHEN ILLUMINATED BY A POINT SOURCE	15
1.8 TECHNIQUES OF OBTAINING INTERFERENCE	18
1.9 SEPERATION BETWEEN NEIGHBOURING BRIGHT FRINGES	19
1.10 COHERENCE	20
2. NEWTON'S RING	
2.1 THEORY	22
2.2 CONSTRUCTIVE INTERFERENCE	23
2.3 DESTRUCTIVE INTERFERENCE	23
2.4 DIAMETER OF DARK AND BRIGHT RING	23
2.5 CIRCULAR FRINGES	27
2.6 DETERMINATION OF WAVELENGTH OF LIGHT	27
2.7 APPLICATIONS OF NEWTON'S RINGS	28
3.EXPERIMENT TO DETERMINE WAVELENGTH	
3.1 EXPERIMENTAL ARRANGEMENT	31

3.2 PROCEDURE	31
3.3 EXPERIMENT TO DETERMINE REFRACTIVE INDEX OF A LIQUID	32
4.DATA AND ANALYSIS	35
5.CONCLUSION	40
6.REFERENCE	41

CHAPTER 1
INTRODUCTION

1.1 INTERFERENCE

Interference occurs when two waves combine to create a resultant wave with either a greater, lesser, or equal amplitude. When multiple light waves of identical frequency intersect, the resulting outcome is influenced by both their amplitudes and phases. The principle of superposition dictates that the resultant wave at any given point and time is determined by the combination of these waves. Algebraically adding the amplitudes of the individual waves yields the combined effect at each point within the overlapping region, assuming equal amplitudes for the component waves.



At specific locations, the two waves might synchronize in phase.

In such instances, the resultant wave's amplitude equals the combined sum of the two waves' amplitudes, as illustrated in the figure. Consequently, the amplitude of the resultant wave

$$A_R = A + A = 2A$$

Hence, the intensity of the resultant wave is

$$I_R \propto A_R^2 = 2^2 A^2 = 2^2 I$$

Clearly, the resultant intensity surpasses the combined intensity of the individual waves.

$$I_R > I + I = 2I$$

Hence, the interference occurring at these points is termed constructive interference. A stationary bright band of light is visible at locations experiencing constructive interference.

At specific alternate locations, the two waves may be in opposite phase. Consequently, the resultant wave's amplitude equals the combined sum of the amplitudes of the two waves, thus determining the amplitude of the resultant wave.

$$A_R = A - A = 0$$

Hence, the intensity of the resultant wave is

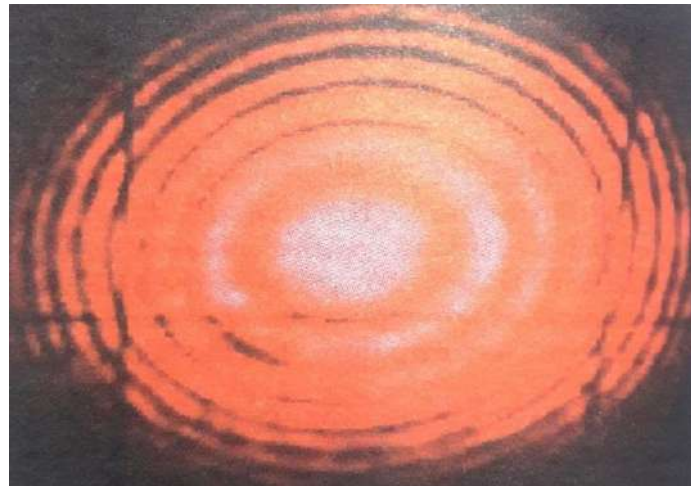
$$I_R \propto 0^2 = 0$$

It's evident that the resulting intensity is lower than the combined intensity of the individual waves.

$$I_R < 2I$$

Hence, the interference occurring at these locations is termed destructive interference. A stationary dark band of light is noticed at points experiencing destructive interference. Thus, it's evident that there is a redistribution of energy within the region.

Therefore, when two or more coherent light waves overlap, it leads to bright areas in some regions and dark areas in others. These bright and dark regions alternate and can form straight bands, circular rings, or other intricate shapes. The alternating bright and dark bands are referred to as interference fringes. This redistribution of light energy resulting from the overlap of light waves from two or more coherent sources is termed interference.



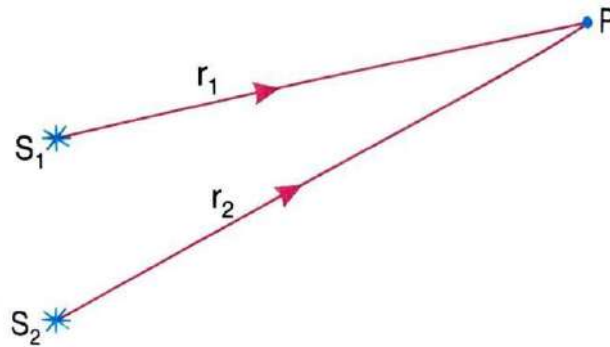
In the central bright spot, constructive interference occurs, followed by a ring of destructive interference, then another constructive region, and so forth

Let's examine two light sources, S_1 and S_2 , depicted in the figure. Assuming these sources are identical and emit harmonic waves of the same wavelength, with the waves in phase at both S_1 and S_2 . Light emitted from these sources travels along distinct paths, S_1P and S_2P , before converging at point P . Now, our inquiry revolves around determining whether the superposition of these waves results in brightness or darkness at point P .

We observe that the waves follow distinct geometric paths, $S_1P = r_1$ and $S_2P = r_2$, which vary in length. Additionally, the mediums through which the waves propagate may differ, leading to discrepancies in optical path lengths. If μ_1 represents the refractive index of the medium traversed by the ray S_1P , then the corresponding optical path length is $\mu_1 r_1$.

Similarly, for the ray S_2P traveling through a medium with refractive index μ_2 , the optical path length becomes $\mu_2 r_2$. These optical paths accommodate a different number of wave cycles along their

lengths. Consequently, the optical path difference between the waves at point P is $(\mu_2 r_2 - \mu_1 r_1)$, which may correspond to a few complete waves or a mixed fraction of waves. This implies that despite commencing with the same phase, the waves may arrive at point P with different phases due to their traversal along distinct optical path lengths.



When the optical path difference $\Delta = (\mu_2 r_2 - \mu_1 r_1)$ equals zero or an integer multiple of wavelength λ , the waves converge in phase at point P, aligning their crests correspondingly.

That is, if $\Delta = m\lambda$

When m , an integer, assumes values such as $m = 0, 1, 2, 3, 4, 5, \dots$, the waves synchronize in phase, resulting in constructive interference or brightness upon overlapping at point P.

Conversely, when the optical path difference $\Delta = (\mu_2 r_2 - \mu_1 r_1)$ equals an odd integer multiple of half-wavelength, $\lambda/2$, the waves reach point P out of phase, aligning with crest-to-trough correspondence. This occurs if

$$\Delta = (2m+1) \lambda/2$$

When m , an integer, ranges from $m = 0, 1, 2, 3, 4, 5, \dots$, the waves are reversed relative to each other, resulting in their overlapping at point P causing destructive interference or darkness.

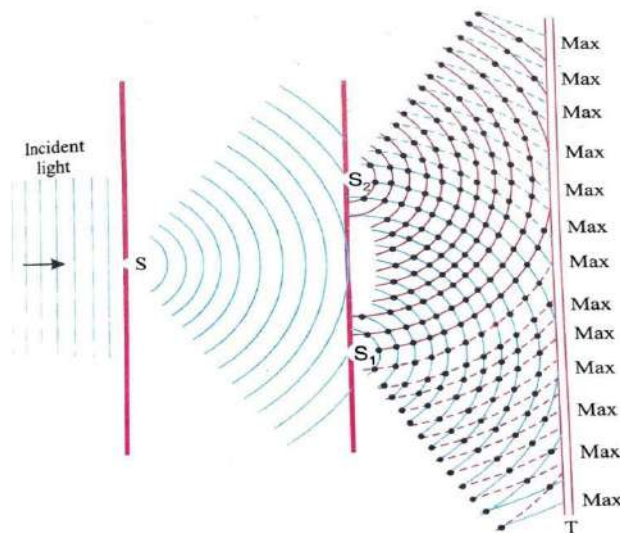
The areas of brightness and darkness are alternatively referred to as regions of maxima and minima.

1.2 YOUNG'S DOUBLE SLIT EXPERIMENT

As early as 1665, Grimaldi attempted to induce interference between two light beams. He passed sunlight into a dimly lit room through two pinholes in a screen, anticipating the emergence of bright and dark bands where the beams intersected. However, he observed uniform illumination instead. Approximately 136 years later, in 1801, Thomas Young conducted the first demonstration of light wave interference. Young allowed sunlight to pass through a single pinhole and then directed the emerging light toward two additional pinholes, ultimately projecting it onto a screen. The spherical waves emanating from the pinhole interacted with each other, resulting in a few coloured fringes appearing on

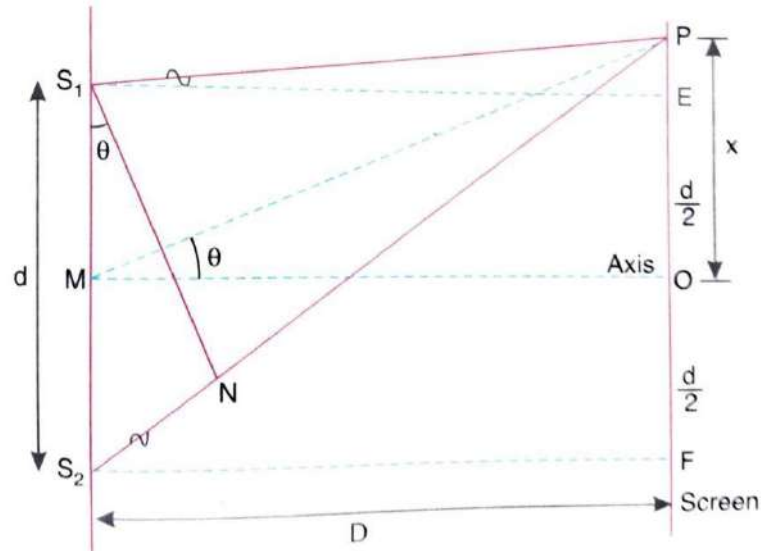
the screen. Due to the minimal amount of light passing through the pinhole, the fringes were faint and challenging to discern. Subsequently, the pinholes were replaced with narrow slits that permitted a greater amount of light to pass through. Additionally, sunlight was substituted with monochromatic light. Young's experiment became known as the double-slit experiment.

The basic setup of the double-slit experiment is depicted in the figure. The primary light source used is typically a monochromatic source, often a sodium lamp emitting yellow light with a wavelength of approximately 5893 angstroms. This light isn't conducive to causing interference since emissions from different parts of a typical source lack coherence. Consequently, the monochromatic light is directed through a narrow slit, S , allowing only light from a small region of the source to pass through, behaving more akin to an ideal light source. From slit S , cylindrical wavefronts are generated, which then fall onto the two closely spaced narrow slits, S_1 and S_2 , as shown in the figure. These slits are exceptionally narrow. The cylindrical waves emerging from S_1 and S_2 overlap. If the slits are equidistant from S , the phase of the wave at S_1 aligns with the phase of the wave at S_2 . Consequently, the waves leaving S_1 and S_2 are consistently in phase, turning S_1 and S_2 into secondary coherent sources. The waves emitted from S_1 and S_2 interfere with each other, resulting in the formation of alternating dark and bright fringes on the screen at T .



1.3 OPTICAL PATH DIFFERENCE BETWEEN THE WAVES AT P

Consider an arbitrary point, P , located on the screen T , positioned at a distance D from the double slits. Let θ represent the angle between the line MP and the horizontal line MO . Let S_1N denote a normal line extending from point S_2P . The distances



PS_1 and PN are equal. The waves initially emitted from the slits, labeled S_1 and S_2 , are in phase with each other. The discrepancy in the distances these waves travel is denoted as S_2N . Assuming the experiment takes place in air, the optical paths mirror the geometric paths. The manner in which the two waves interfere at point P hinges solely on the number of wavelengths encompassed in the path difference S_2N . If S_2N encompasses a whole number of wavelengths, the waves combine constructively, resulting in a peak intensity of light on the screen at point P . Conversely, if it includes an odd number of half-wavelengths, the waves interfere destructively, leading to a minimal intensity at point P .

Let the point P be at a distance x from O . Then

$$PE = x - \frac{d}{2} \text{ and } PF = x + \frac{d}{2}$$

$$(S_2P)^2 - (S_1P)^2 = [D^2 + (x + \frac{d}{2})^2] - [D^2 + (x - \frac{d}{2})^2]$$

$$(S_2P)^2 - (S_1P)^2 = 2xd$$

$$S_2P - S_1P = \frac{2xd}{(S_2P + S_1P)}$$

We can approximate that $S_2P \cong S_1P \cong D$

$$\text{So path difference} = S_2P - S_1P = \frac{xd}{D}$$

Now, we determine the prerequisites for witnessing both illuminated and shadowed bands on the screen.

1.4 BRIGHT FRINGES

Bright fringes emerge when the waves originating from S_1 and S_2 combine constructively. This phenomenon first manifests at O , known as the axial point, where both waves travel an identical optical path length and synchronize upon arrival. Subsequent bright fringes occur as the wave from S_2 traverses

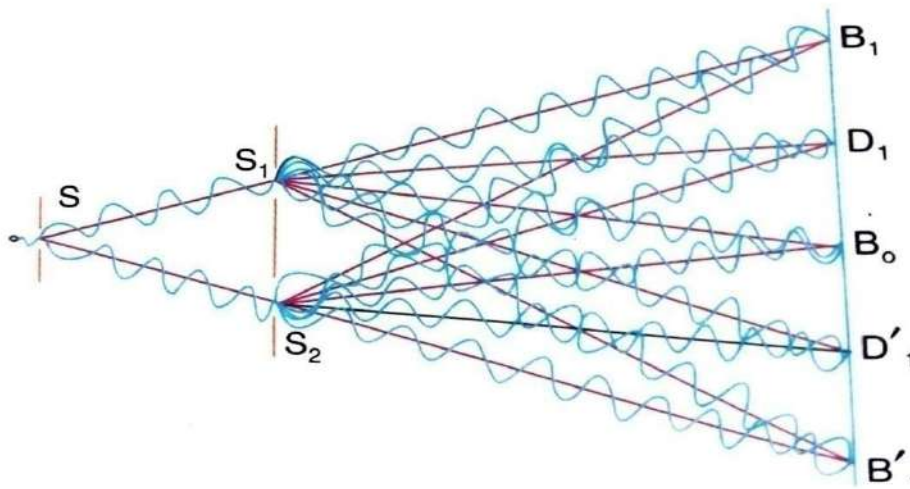
one complete wavelength farther than the wave from S_1 . In essence, constructive interference prevails if the disparities between S_1P and S_2P encompass a whole number of wavelengths.

The condition for finding a bright fringe at P is that

$$S_2P - S_1P = m\lambda$$

That is $xd/D = m\lambda$

Where m is called order of the fringe



The bright fringe B_0 , positioned at O and labeled with $m=0$, is termed the zero-order fringe. This indicates that the disparity in the paths of the two waves reaching O is nonexistent. The fringe at B_1 denotes the first-order bright fringe from the axis, designated as $m=1$; the gap between the two waves reaching B_1 is one wavelength. Similarly, the second-order bright fringe ($m=2$) will be situated where the path difference is 2λ , and so forth.

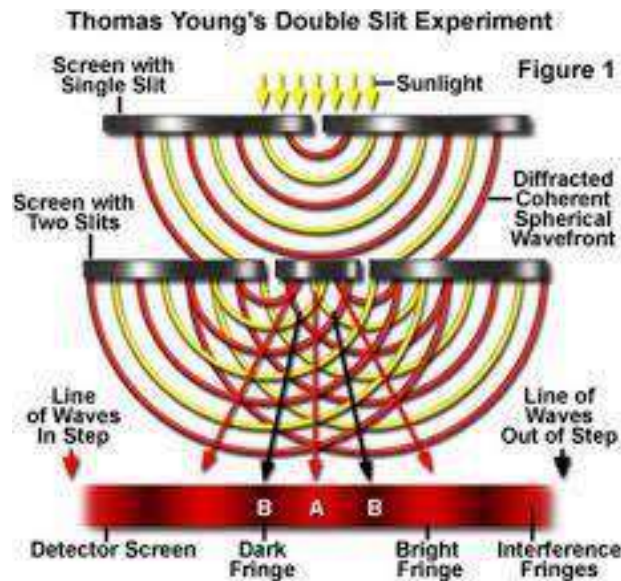
1.5 DARK FRINGES

The initial occurrence of a dark fringe arises when the disparity between $(S_2P - S_1P)$ equals half a wavelength, $\lambda/2$. This results in the waves being out of phase at point P . Subsequently, the second dark fringe emerges when $(S_2P - S_1P)$ equals three halves of a wavelength, $3\lambda/2$. The m th dark fringe arises when

$$(S_2P - S_1P) = (2m+1)\lambda/2$$

The condition for finding a dark fringe is $xd/D = (2m+1)\lambda/2$

The initial occurrence of a dark fringe, denoted as D_1 from the axis with $m=0$, happens when the difference in path between the two waves amounts to half a wavelength, $\lambda/2$. The subsequent occurrence, labeled as the second order dark fringe ($m=1$), appears when the path difference extends to three halves of a wavelength, $3\lambda/2$, and so forth.



1.6 CONDITION FOR INTERFERENCE

(a) CONDITION FOR SUSTAINED INTERFERENCE

- (1) For steady interference to occur, it's essential that the waves from both sources possess identical frequencies. Any discrepancy in the frequencies of the light waves leads to irregular fluctuations in the phase difference over time. Consequently, the intensity at any given point also fluctuates over time, preventing the observation of consistent interference patterns.
- (2) For an observable interference pattern, it's necessary for the two light waves to exhibit coherence. Coherent light waves retain a constant phase difference across both time and space. Consequently, this stability results in the formation of a stationary interference pattern.
- (3) The difference in paths between the overlapping waves should be within the coherence length of the waves. As we've previously understood, light is emitted as wave trains, each with a finite coherence length.
- (4) If both sets of waves are plane polarized, their planes of polarization need to align. Interference effects cannot occur if the waves are polarized in planes that are perpendicular to each other.

(b) CONDITION FOR FORMATION OF DISTINCT FRINGE PATTERN:

- (1) To distinguish the fringe pattern, it's essential for the two coherent sources to be positioned closely together. When the sources are widely separated, the fringe width becomes extremely narrow, making it difficult to perceive individual fringes distinctly. The screen needs to be positioned at a considerable distance from the two sources.

(2) In order to achieve clear bright and dark fringes, it's crucial that the combined electric field vectors cancel each other out in the dark regions. This cancellation occurs only when the vectors are antiparallel and of equal magnitude.

1.7 INTERFERENCE BY A PLANE PARALLEL FILM WHEN ILLUMINATED BY A POINT SOURCE

We explored the effect of a parallel light beam striking a thin film and examined the interference resulting from the reflection of waves off its upper and lower surfaces. Now, we'll investigate how the film is illuminated by a point source of light. To observe the film without blocking the incident beam, we'll utilize a partially reflecting plate G , as depicted in Figure A. However, for analyzing the interference pattern, we'll position the point source S directly above the film, as shown in Figure B. In this arrangement, the distances SK (in Figure B) are equivalent to $SA + AK$ (in Figure A), and KS (in Figure B) is perpendicular to the film. Consequently, the waves reflected from the upper surface of the film will appear to originate from the point S' . Where

$$KS' = KS \quad (1)$$

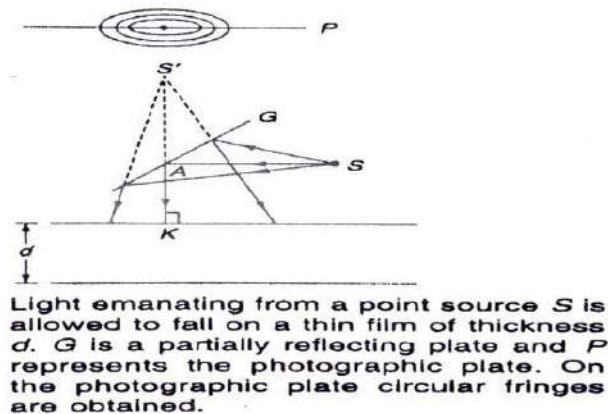


Fig 1.7

Additionally, basic geometric analysis will demonstrate that the waves bouncing off the underside seem to originate from a point marked as S'' .

$$KS'' = KS + 2d/n_2 \quad (2)$$

Equation (2) holds true only for incidences that are nearly perpendicular; this is due to the imperfection in the image formed by a plane refractive surface when it comes to a point source. Consequently, for near-normal incidences, the interference pattern in region I will closely resemble that created by two coherent point sources, S' and S'' . However, this pattern deviates from Young's pattern because S'' does not perfectly replicate point S . For larger angles of incidence, the waves reflected from the lower surface will appear to originate from a point that is shifted from S'' . Therefore, when employing a photographic plate P (as shown in Fig 1.7), interference fringes will generally be captured. The intensity at any arbitrary point Q (in Fig 1.8) will be determined by the following relationships.

$$\Delta = (m + 1/2)\lambda \quad \text{maxima} \quad (3a)$$

$$\Delta = m\lambda \quad \text{minima} \quad (3b)$$

$$\text{Where } \Delta = [n_1 SF + n_2(FG + GH) + n_1 HQ] - [n_1(SA + AQ)] \quad (4)$$

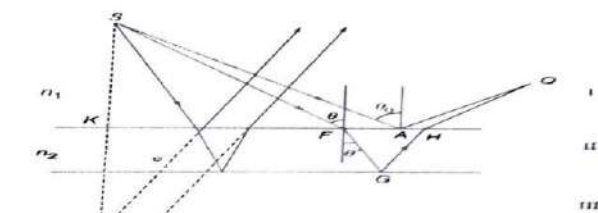
The statement denotes the optical path discrepancy, with an assumption that a sudden phase shift of 3.14 takes place in one of the reflections. Here, n_1 and n_2 represent the refractive indices of media I and II, respectively. These conditions are accurately applicable, even for significant angles of incidence. Moreover, it can be demonstrated that they hold true for near-normal incidences as well.

$$\Delta \approx 2n_2 d \cos\theta \quad (5)$$

A more rigorous calculation shows

$$\Delta \approx 2n_2 d \cos\theta \left[1 - \frac{n_1^2 \sin\theta \cos\theta}{n_2^2 - n_1^2 \sin^2\theta} \left(\frac{\theta_0 + \theta}{2} \right) \right] \quad (6)$$

Where the angles θ , θ_0 and θ' are defined



If light emanating from a point source S is incident on a thin film then the interference pattern produced in the region I is approximately the same as would have been produced by two coherent point sources S' and S'' (separated by a distance $2d/n_2$) where d represents the thickness of the film and n_2 represents the refractive index of the film.

Fig 1.8

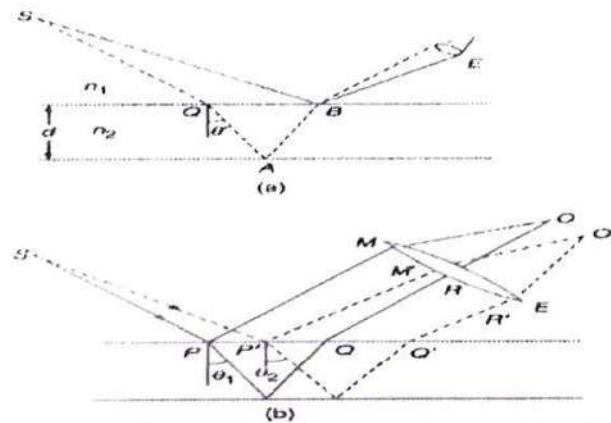
If a photographic plate is placed parallel to the film's surface (refer to Fig. 1.8), it will capture concentric rings alternating between dark and bright. Conversely, when viewing the film with the naked eye from a fixed position, only a limited area of the film will be visible. For instance, from the perspective of the eye positioned at E and the point source S, only a fraction of the film near point B will be observable, and the brightness or darkness of this point will be determined by the optical path difference.

$$\Delta = n_1 SQ + n_2(QA + AB) - n_1 SB$$

Is m. Further, using a method similar to the one described, we obtain

$$\Delta \approx 2n_2 d \cos \theta \quad (7)$$

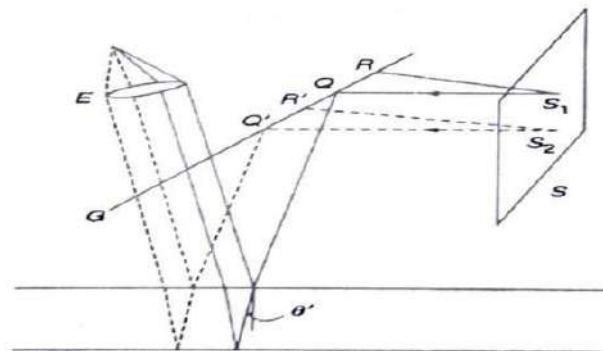
If the observer's focus shifts to infinity rather than directly viewing the film, interference occurs between rays originating from a single incident ray, reflected from both the upper and lower surfaces of the film (refer to Fig 1.9). For instance, rays PM and QR, converging at point O on the retina, stem from the single ray SP, while rays P'M' and Q'R', converging at a distinct point θ on the retina, originate from ray SP'. Due to differing angles of refraction for these ray sets, points O and O' typically exhibit varying intensities.



Light emanating from a point source S is incident on a thin film; (a) if the film is viewed by the naked eye E then the point B will appear to be dark if the optical path $[(n_1 SQ + n_2 (QA + AB)) - n_1 SB]$ is $m\lambda$, and bright if the optical path is $(m + \frac{1}{2})\lambda$. (b) If the eye is focused for infinity then it receives parallel rays from different directions corresponding to different values of the angles of refraction θ' (and hence different values of the optical path difference).

Fig 1.9

Now, we turn our attention to the illumination provided by an extended light source, denoted as S (refer to Fig 1.10). This extended source can be generated, for instance, using a sodium lamp and a ground glass plate. Each individual point on this extended source generates its own interference pattern on the photographic plate p, which will be displaced in relation to one another. As a result, a distinct fringe pattern does not emerge on the photographic plate. However, when observing the film with the naked eye, rays from all points on the film reach the eye. If the eye focuses at infinity, parallel light arriving from a specific direction at the eye originates from nearby points on the extended source. The intensity perceived on the retina is determined by the value of $2nd \cos \theta'$, which remains consistent for all parallel rays like S_1Q , S_2Q' , and so forth (refer to Fig 1.10). Rays traveling in different directions (e.g., S_1R , S_2R') correspond to varying values of θ' and focus on distinct points on the retina. Since θ' remains constant across the circumference of a cone (with its axis perpendicular to the film and its vertex at the eye), the eye perceives alternating dark and bright patterns



13.16 Light emanating from an extended source illuminates a thin film. *G* represents the partially reflecting plate and *P* represents the photographic plate. The eye *E* is focussed at infinity.

Fig 1.10

concentric rings, with the centre lying along the direction $\theta' = 0$.

These fringes, resulting from a film with consistent thickness, are termed Haidinger fringes. They are also referred to as fringes of equal inclination because variations in the optical path stem from alterations in the angle of incidence, thus affecting the value of θ' .

1.8 TECHNIQUES OF OBTAINING INTERFERENCE

The relationship between the waves produced by two separate light sources changes quickly over time, preventing coherence despite their identical nature. However, if two sources originate from a single one through a device, any phase alteration in one is mirrored in the other, maintaining a constant phase difference between their emitted waves, resulting in coherence. Techniques for generating coherent light sources can be categorized into two main classes.

- (a) Wavefront splitting : One approach involves splitting a light wavefront from a narrow aperture into two closely spaced slits. These divided parts traverse separate paths and then converge on a screen, creating a fringe pattern—a phenomenon termed interference due to wavefront division. This technique is applicable primarily to narrow sources. Examples employing this method include Young's double slit, Fresnel's double mirror, Fresnel's biprism, Lloyd's mirror, among others.
- (b) Amplitude splitting: Alternatively, the intensity of a light wave, known as its amplitude, is split into two components—reflected and transmitted—through partial reflection at a surface. These components follow distinct paths before merging again, resulting in interference fringes. This phenomenon is termed interference due to amplitude division. Optical tools like beam splitters and mirrors are employed to achieve this division. Interferometers such as those involving interference in thin films (like wedges and Newton's rings) and Michelson's interferometer utilize this technique. This method necessitates an extended light source.

1.9 SEPERATION BETWEEN NEIGHBOURING BRIGHT FRINGES

The m^{th} order fringe happens when $x_m = m\lambda D/d$

And for the $(m+1)^{\text{th}}$ order fringe when $x_{m+1} = (m+1)\lambda D/d$

The fringe width is given as $\beta = x_{m+1} - x_m = \lambda D/d$

The same outcome is achieved for both dark and bright fringes. Consequently, the distance between any consecutive bright or dark fringes, termed fringe width, remains consistent across the screen. Additionally, the width of bright fringes matches that of dark fringes, rendering the alternating bright and dark fringes parallel. From equation, the following observations are deduced:

- 1 . The fringe width (β) remains constant regardless of the fringe order and is directly proportional to the wavelength of light ($\beta \propto \lambda$). Consequently, fringes produced by red light are spaced farther apart compared to those produced by blue light.
2. The fringe width is directly proportional to the distance between the screen and the two slits (BD). Therefore, increasing the screen distance results in wider fringe separation.
3. The fringe width is inversely proportional to the distance between the two slits. Thus, bringing the slits closer together results in wider fringe.

1.10 COHERENCE

Interference fringes were absent on the screen in Grimaldi's experiment because he did not position the slit S in front of the double-slit arrangement. Consequently, only uniform illumination was observed. This occurred because the beams reaching the screen lacked coherence, with their phase difference fluctuating randomly over time. The absence of coherence stems from the light emission process itself. In typical sources of visible light, individual atoms emit light when transitioning from an excited state, releasing excess energy in the form of a burst of light or photon and goes to lower normal state.

This transition process from an upper state to a lower state occurs briefly, typically lasting around 10^{-8} seconds. Consequently, the light emitted by an atom isn't a continuous harmonic wave extending infinitely, but rather a wave train with a finite length containing a limited number of oscillations. Predicting the exact timing of light emission from an atom is impossible since the emission process is entirely random.

Other atoms within the source exhibit similar behaviour but with varying emission times. Combining the wave trains generated by all atoms in the light source results in a series of wave trains with randomly distributed phases. As one wave train transitions to the z correlate the phase of one wave train with another. The phase of a wave train from one atom remains constant in relation to another atom's wave train for only about 10^{-8} seconds, indicating that the two wave trains can be coherent for a maximum duration of approximately 10^{-8} seconds. Thus, light from conventional sources is characterized by two significant parameters: coherence time and coherence length.

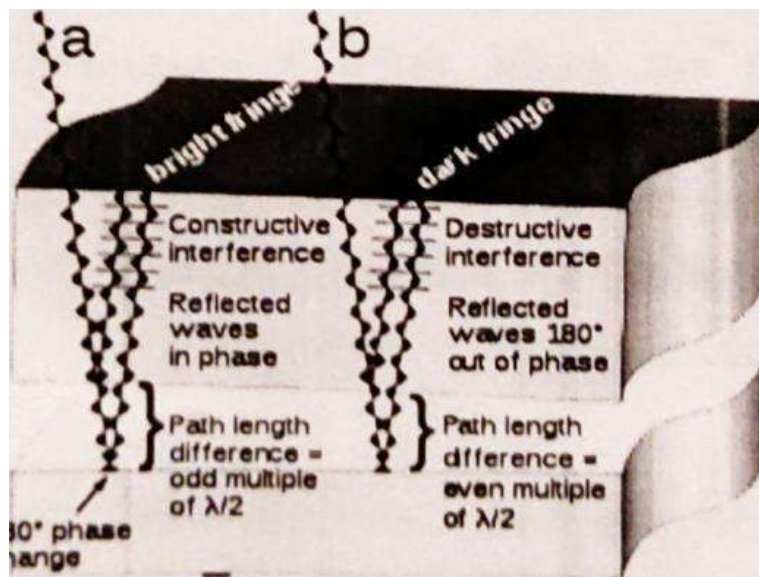
Coherence time refers to the average duration during which the wave remains sinusoidal and its phase can be reliably predicted. Coherence length, on the other hand, represents the length of the wave packet over which it can be assumed to be sinusoidal with a predictable phase. For instance, light emitted from a sodium discharge lamp typically has a coherence length of about 2 to 3 cm, while the coherence length of white light is typically a fraction of a cm. In the double-slit experiment, the presence of slit S ensures that the same group of wave trains is incident on slits S_1 and S_2 . When the phase of the wave changes at S, this change is instantly communicated to both S_1 and S_2 . Consequently, the waves emerging from S_1 and S_2 are coherent with each other, leading to the formation of a stationary interference pattern on the screen.

CHAPTER 2
NEWTON'S RING

NEWTON'S RING

Newton's rings in optics refer to a sequence of concentric bands, alternately light and dark in colour, observed between two glass pieces where one is convex and rests convex side down on another piece with a flat surface, thus creating a thin layer of air between them. This phenomenon arises from the interference of light waves, wherein the superposition of wave trains leads to brightening when their crests align and dimming when their crests and troughs coincide. Both top and bottom surfaces of the air film between the glass pieces reflect light waves that interfere, resulting in the formation of these rings. They are named after the 17th-century English physicist Sir Isaac Newton, who extensively studied them. When observed under monochromatic light, Newton's rings manifest as a set of concentric bright and dark rings, centered at the point of contact between the two surfaces. With white light, they exhibit a rainbow-colored concentric ring pattern, as the various wavelengths of light interfere differently at different thicknesses of the air layer between the surfaces.

2.1 THEORY



It displays a magnified view of a portion of the upper glass surface on the optical flat, demonstrating the formation of interference fringes. In areas where the variance in path length equals an odd multiple $(2n+1)$ of half a wavelength (λ) , the reflected waves amplify, producing a bright spot. Conversely, in regions where the variance in path length equals an even multiple $(2n)$ of half a wavelength $(\lambda/2)$, the reflected waves cancel, resulting in a dark spot. This leads to a sequence of circular bands alternating between brightness and darkness, known as interference fringes. Newton's rings are formed by positioning two plano-convex lenses with their flat sides touching, one of which has a slightly convex surface, causing the ring formation. When illuminated with white light, the rings exhibit a rainbow spectrum because the various wavelengths of each colour interfere at distinct points

The arrangement involves placing a gently curved glass atop a flat optical glass. They touch only at the centre, with a slight space between elsewhere, expanding as you move outward. Light of a single colour passes through the upper glass, reflects off both its underside and the optical flat's top, merging the reflections. However, the lower reflection travels a longer route due to the gap, equal to twice the separation. Additionally, the lower reflection undergoes a 180-degree phase shift, whereas the internal reflection from the upper glass's underside does not. The intensity of the reflected light relies on the path length discrepancy between the two reflections.

2.2 CONSTRUCTIVE INTERFERENCE

In regions where the path length gap between the two rays equals an odd number of half-wavelengths ($\lambda/2$) of the light waves, the reflected waves will synchronize, aligning the troughs and peaks. Consequently, they'll combine, enhancing the reflected light intensity, resulting in a bright spot being noticeable in that location.

2.3 DESTRUCTIVE INTERFERENCE

In different positions, where the path length variation corresponds to an even number of half-wavelengths, the reflected waves will be 180 degrees out of phase, aligning a trough of one wave with a peak of the other. Consequently, they will counteract each other, resulting in diminished or zero light intensity. Thus, a dark zone will be evident in such areas. Due to the 180-degree phase reversal caused by the reflection of the lower ray, the centre where the two pieces meet appears dark.

This interference leads to the emergence of a pattern of alternating bright and dark lines or bands known as "interference fringes" on the surface. These fringes resemble contour lines found on maps, indicating variations in the thickness of the air gap. The distance between the surfaces remains constant within each fringe. The disparity in the air gap between two neighbouring bright or dark fringes corresponds to one wavelength (λ) of the light, resulting in a half-wavelength discrepancy. Because the wavelength of light is incredibly small, this method enables the measurement of minute deviations from flatness. For instance, the wavelength of red light is approximately 700 nm, meaning that using red light, the height difference between two fringes is halved to about 350 nm, roughly 1/100th the diameter of a human hair. As the gap between the glasses widens outward from the centre, the interference fringes take the form of concentric rings. For non-spherical glass surfaces, the fringes deviate from circular shapes. When illuminated from above, featuring a dark centre, the radius of the Nth bright ring is determined by

$r_n = \left(\lambda R N^{\frac{1}{2}}\right)^{\frac{-1}{2}}$ where N is the bright-ring number, R is the radius of curvature of the glass lens the light is passing through, and A is the wavelength of the light

The above mentioned equation is also valid for the dark rings observed in the ring pattern produced by transmitted light

Let's consider light directed onto the flat surface of a convex lens positioned atop the optically flat glass surface below. As the light traverses the glass lens, it encounters the glass-air boundary, transitioning from a higher refractive index (n) to a lower value of n. This transition entails no alteration in phase for the transmitted light. The reflected light, which constitutes about 4% of the total, likewise undergoes no phase shift. The light that enters the air travels a distance, denoted as 't', before being reflected at the flat surface beneath. This reflection at the air-glass boundary causes a half-cycle phase shift due to the lower refractive index of air compared to glass. Upon reflection at the lower surface, the reflected light retraces its path over a distance of 't' and re-enters the lens. The interference between these two reflected rays is determined by the overall phase change induced by the additional path length of 2t and the half-cycle phase shift incurred during reflection at the lower surface. When the distance 2t is shorter than a wavelength, the waves interfere destructively, resulting in the central region of the pattern appearing dark.

Applying a comparable examination to illuminate the device from beneath, as opposed to above, reveals that in this scenario, the central segment of the pattern appears bright rather than dark. (A comparison of the provided example images illustrates this distinction.) When considering the radial distance of a bright ring, denoted as 'r', and the lens's radius of curvature, 'R', the air gap between the glass surfaces can be accurately approximated by the formula: $t = (r^2)/2R$

Disregarding the impact of observing the pattern at an angle other than perpendicular to the incident rays, an air film of fluctuating thickness can be achieved by positioning either a Plano-convex lens or a biconvex lens with a considerable focal length on a flat glass plate. At the point of contact, the air film has zero thickness, gradually thickening as it extends outward.

When light strikes the air film, a portion is reflected from the film's upper surface, while another part is reflected from its lower surface (the upper surface of the glass plate). These reflected rays overlap, leading to the formation of constructive and destructive interference patterns. If the incident light rays fall perpendicularly onto the film, the discrepancy in the paths of the rays reflected from the upper and lower surfaces of the film is solely determined by the thickness 't' of the film. As the points across the air film with identical thickness form concentric circles, with the point of contact as the centre, concentric circular patterns emerge. These patterns are known as Newton's rings.

When observing the rings under white light, the fringes exhibit vivid colours. When monochromatic light is used, both dark and bright fringes are visible. In either scenario, the centre of the fringe pattern appears dark (a dark spot) due to the path difference at the point of contact and a half-wavelength ($\lambda/2$) path difference caused by reflection from the denser medium's surface (the glass plate). The fringes can be observed using a long, focused microscope.

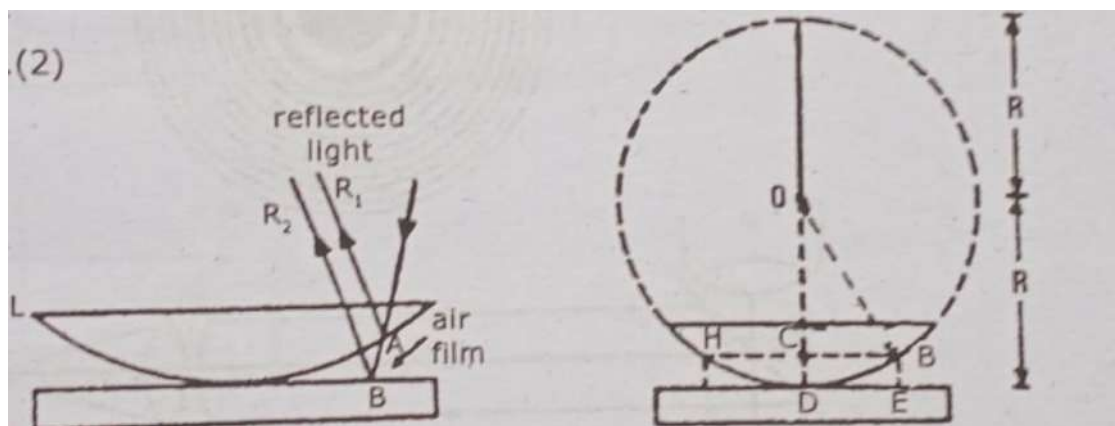
Newton's rings can form on a liquid film by positioning the liquid film between the convex lens and glass plate. Similarly, Newton's rings can also be detected in transmitted light. In this scenario, the centre of the fringe pattern appears bright since there is no phase change due to reflection at the denser medium's surface. This observation illustrates that the reflected and transmitted systems complement each other.

2.4 DIAMETER OF DARK AND BRIGHT RING

Consider R as the radius of curvature of the lens's surface touching the glass plate, D as the point of contact, and r as the radius of the n th ring formed on the air film at point P , where the film's thickness is t . The discrepancy in path between the rays reflected at the upper and lower surfaces of the air film at P is expressed as

$$\delta = 2pt \cos r = 2t \quad (1)$$

Since for air $p = 1$ and for normal incidence $r = 0$



From the fig 2.2

$$t(2R - t) = r_n^2$$

Since $t \ll R$, t^2 can be neglected

$$2Rt = r_n^2$$

$$2t = r_n^2/R \quad (2)$$

From equation 1 & 2

$$\delta = r_n^2/R \quad (3)$$

Because one of the interfering rays reflects from the denser medium's surface, the glass plate, there is an extra phase shift, denoted as π , which equates to a path difference of $\lambda/2$. Consequently, for the n th dark ring

The equation $\delta = n\lambda$ holds true, where n equals 1, 2, 3..., and λ represents the wavelength of the monochromatic light utilized.

$$r_n^2/R = n\lambda \quad (4)$$

$$r_n = \sqrt{nR\lambda}$$

For the n th bright fringe

$$\delta = (2n+1)\lambda/2 \quad \text{where } n=0,1,2,3$$

$$r_n^2 = (2n+1)R\lambda/2 \quad (5)$$

If D_n is the diameter of the n th ring, then from equation 4 we get

$$D_n^2 = 4nR\lambda \quad (6)$$

$$D_n = \sqrt{4nR\lambda} \quad (7)$$

$$D_n \propto \sqrt{n}$$

When n equals 0, the diameter of the dark ring diminishes to zero, marking the central dark ring. However, in enumerating the order of the dark rings, we exclude the central ring from the count, beginning with $n = 1, 2, 3...$ for the first, second, and subsequent dark rings.

$$D_1:D_2:D_3:\dots = \sqrt{1}:\sqrt{2}:\sqrt{3}:\dots$$

For the n th bright ring

$$D_n^2 = 4(2n+1)R\lambda/2 \quad (8)$$

From the first bright ring, $n=0$

$$D_1 = \sqrt{4R\lambda/2}$$

For the second bright ring, $n = 1$

$$D_n^2 = 4(2(n-1) + 1)R\lambda/2 = 4(2n-1)R\lambda/2 \quad (9)$$

$$D_n = \sqrt{4(2n-1)R\lambda/2}$$

Substituting $n = 1, 2, 3, \dots$ (number of rings), the diameters of the first, second, third etc... bright rings can be obtained.

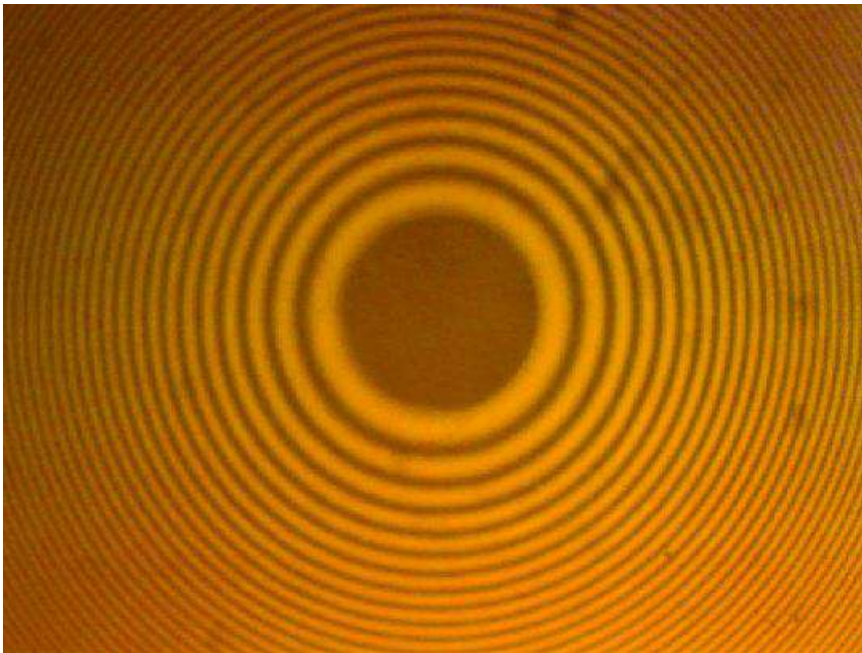
If a liquid film of refractive index μ is obtained between the lens and plate,

(a) For the n th dark rings, $D_n^2 = 4nR\lambda/\mu$ and

(b) For the n th bright ring $D_n^2 = 4(2n - 1)R\lambda/2$

2.5 CIRCULAR FRINGES

In the setup of Newton's rings, there's a thin layer of air between a plano-convex lens and a glass plate. At the contact point, the air film's thickness is zero, and it increases outward. Points with the same air film thickness form a circle, centered at the contact point. Consequently, the air film maintains a consistent thickness along any circle centered at the contact point between the lens and the glass plate, resulting in circular fringes.



2.6 DETERMINATION OF WAVELENGTH OF LIGHT

A large plano-convex lens with a radius of curvature around 100 cm and a flat glass plate are cleaned and placed together with a metal ring holding them in place. Positioned before a sodium vapor lamp, the system is aligned so that yellow light at a 45° angle falls onto the glass plate. The light is then redirected to shine directly onto the lens-plate system. Using a low power traveling microscope, the circular rings are brought into focus, aligning the cross-wire with the center of the dark spot at the center

of the ring system. The microscope is then slowly moved to one side until the 22nd dark ring is reached, and then in the opposite direction until the 20th or 19th dark ring is reached.

The vertical crosswire aligns tangentially with the 19th ring, and the reading is recorded using the graduated scale on the carriage. Moving from the 19th ring, the positions of the 18th, 17th, 16th, and 15th dark rings are noted. Next, the microscope swiftly moves to the left side of the ring system, halting at the 5th dark ring. The crosswire is once again aligned tangentially with the 5th dark ring, and its position is recorded. The difference between the readings on the right and left sides of the 5th dark ring yields its diameter value. This process continues until the 19th ring, and its reading is noted. The squares of the diameters are calculated from these values, and a graph is plotted correlating D_m with the ring number 'm', resulting in a straight line.

We have

$$D_m^2 = 4m\lambda R$$

For $(m+p)^{\text{th}}$ ring

$$D_{m+p}^2 = 4(m+p)\lambda R$$

$$D_{m+p}^2 - D_m^2 = 4p\lambda R$$

$$\lambda = (D_{m+p}^2 - D_m^2) / 4pR$$

The slope of the straight line gives the value of $4\lambda R$. Thus

$$\lambda = \text{Slope} / 4R$$

The lens's radius of curvature, R , can be assessed using a spherometer, and λ is calculated utilizing the provided equation.

2.7 APPLICATIONS OF NEWTON'S RINGS

It has several practical applications because interference pattern is formed by the reflection of light between two surfaces

Surface Flatness Testing: Newton's rings are commonly used in optics for testing the flatness of surfaces, such as lenses, mirrors, and other optical components. Variations in the spacing of the rings indicate deviations from flatness.

Thin Film Thickness Measurement: By analyzing the interference pattern of Newton's rings, one can determine the thickness of thin films deposited on a substrate. This is crucial in industries like semiconductor manufacturing, where precise control of film thickness is necessary.

Quality Control in Manufacturing: Newton's rings can be used to inspect the quality of manufactured optical components. Variations in the pattern can reveal imperfections or defects in the surface of the material.

Material Analysis: Newton's ring can help analyse the optical properties of materials. For instance, studying the interference patterns formed by placing different materials in contact can provide insights into their refractive indices and other optical characteristics

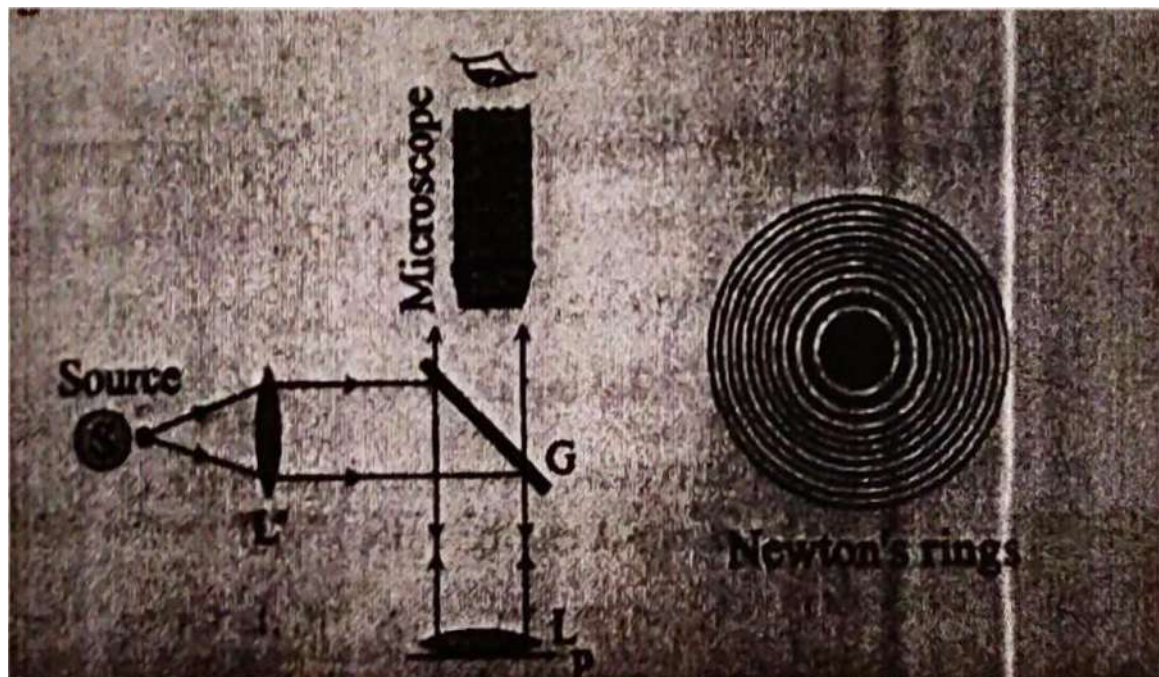
Microscopy: In microscopy, Newton's ring can be used to examine the flatness and quality of microscope slides or other transparent specimens this can aid researchers in obtaining clear and accurate images under the microscope.

CHAPTER 3

EXPERIMENT TO DETERMINE WAVELENGTH OF MONOCHROMATIC LIGHT- NEWTON'S RINGS METHOD

3.1 EXPERIMENTAL ARRANGEMENT

Light emitted from a single-color source, after being made parallel by a convex lens L' , is directed onto a glass plate at a right angle, where it is then split into two paths: some is reflected by the curved surface of the lens, and some passes through the glass plate. These two reflected beams interact, creating circular interference patterns known as fringes. These fringes appear within the air layer and require a long-focus microscope to be clearly observed.



3.2 PROCEDURE

The setup is configured to generate Newton's rings, and the microscope is adjusted for observing them. The microscope is precisely positioned such that the point where the cross wires intersect aligns with the centre of the ring pattern, and one of the cross wires is perpendicular to the microscope's movement direction. Beginning with a clearly visible dark ring at the center labeled as the "nth" ring, the microscope is then shifted to the $(n+20)$ th dark ring, ensuring the cross wire aligns tangentially with the ring. The microscope's reading is recorded, and then it is slowly moved back using a screw mechanism, noting readings for every alternate dark ring until reaching the nth dark ring. This process is repeated on the other side of the center, and observations are continued up to the same number of rings. Subsequently, the diameters of the rings are computed.

3.3 EXPERIMENT TO DETERMINE THE REFRACTIVE INDEX OF A LIQUID

The setup for this experiment mirrors that of the previous one. It involves positioning an air film between a convex lens and a flat glass plate. Using a traveling microscope, the diameters of the n th and $(n+m)$ th dark rings are measured. $(D_{n+m}^2 - D_n^2)$ is calculated. The value of m , which can be assumed to be 10 as in the previous experiment, is used in the calculations.

$$D_{n+m}^2 - D_n^2 = 4mR\lambda \quad (1)$$

The convex lens is taken off the glass plate, and a droplet of the specified liquid with a known refractive index is deposited onto the plate. Then, the lens is positioned over the liquid droplet, and the diameters of the n th and $(n+m)$ th rings are measured as D_n' and $D_{(n+m)}'$.

For the n^{th} dark ring,

$$2\mu t \cos r = n\lambda$$

$$2t = n\lambda/\mu \quad (r=0) \quad (2)$$

$$\text{But, } 2t = \frac{r_n'}{R} = \frac{(D_n')^2}{4R} \quad (3)$$

From equation (2) and (3) we get,

$$(D_n')^2 = \frac{4nR\lambda}{\mu} \quad (4)$$

$$\text{Similarly, } (D_{(n+m)}')^2 = \frac{4(n+m)R\lambda}{\mu} \quad (5)$$

$$(D_n')^2 - (D_{(n+m)}')^2 = \frac{4mR\lambda}{\mu} \quad (6)$$

Dividing equation (1) with equation (6) we get

$$\mu = \frac{(D_n')^2 - (D_{(n+m)}')^2}{(D_{(n+m)}')^2 - (D_n')^2}$$

With this equation

μ , one can determine the refractive index of the liquid.

To find the radius of curvature R of the lens

Focal length of the lens, $f = 100$ cm

Distance between the lens and the object when the image is formed by the side of the object $d = 50$ cm

$$R = \frac{f \times d}{f - d}$$

$$= (100 \times 50) / (100 - 50)$$

$$= 100 \text{ cm}$$

$$R = 1 \text{ m}$$

CHAPTER 4

DATA AND ANALYSIS

DATA AND ANALYSIS

The readings of the microscope to find the wave length of **monochromatic light** are tabulated as follows

Order of the ring	Reading of the microscope		Diameter D (cm)	D^2 (cm^2)	$D_{n+10}^2 - D_n^2$
	Right (cm)	Left (cm)			
2	2.397	2.565	0.168	0.028	0.253
4	2.305	2.610	0.305	0.093	0.247
6	2.270	2.695	0.425	0.181	0.187
8	2.239	2.675	0.436	0.190	0.230
10	2.220	2.701	0.481	0.231	0.248
12	2.195	2.725	0.530	0.281	
14	2.171	2.754	0.583	0.340	
16	2.155	2.762	0.607	0.368	
18	2.132	2.780	0.648	0.420	
20	2.113	2.805	0.692	0.479	

Mean $D_{n+10}^2 - D_n^2 = 0.233 \text{ cm}^2$

For nth dark ring

$$D_n^2 = 4Rn\lambda$$

If D_{n+m} is the diameter of the (n+m)th dark ring

$$D_{n+m}^2 = 4R(n+m)\lambda$$

$$D_{n+m}^2 - D_n^2 = 4mR\lambda$$

Taking $m = 10$,

$$\lambda = (D_{n+10})^2 - (D_n)^2 / 4mR$$

The radius of curvature R of the lower face of the lens is determined by

Boy's method.

From these readings λ can be calculated.

$$\lambda = 590.83 \text{ nm}$$

The readings of the microscope to find the refractive index of **water** are tabulated As follows

Order of the ring	Reading of the microscope		Diameter D (cm)	$D^2 (cm^2)$	$D_{n+10}^2 - D_n^2$
	Right(cm)	Left (cm)			
2	7.363	7.597	0.234	0.055	0.177
4	7.325	7.585	0.260	0.068	0.186
6	7.346	7.602	0.256	0.066	0.143
8	7.252	7.695	0.443	0.196	0.144
10	7.295	7.665	0.370	0.137	0.223
12	7.203	7.685	0.482	0.232	
14	7.201	7.705	0.504	0.254	
16	7.245	7.702	0.457	0.209	
18	7.152	7.735	0.583	0.340	
20	7.155	7.755	0.600	0.360	

Mean value of $D_{n+10}^2 - D_n^2 = 0.175 \text{ cm}^2$

Refractive index of liquid $\mu = (0.233 \times 10^{-4}) \div (0.175 \times 10^{-4})$

$= 1.331$

The readings of the microscope to find the refractive index of **oil** are Tabulated as follows

Order of the ring	Reading of the microscope		Diameter D (cm)	$D^2 (cm^2)$	$D_{n+10}^2 - D_n^2$
	Right(cm)	Left (cm)			
2	7.361	7.589	0.228	0.052	0.160
4	7.326	7.579	0.253	0.064	0.165
6	7.288	7.637	0.349	0.122	0.154
8	7.272	7.655	0.383	0.147	0.159
10	7.250	7.665	0.415	0.172	0.157
12	7.232	7.692	0.460	0.212	
14	7.219	7.698	0.479	0.229	
16	7.193	7.718	0.525	0.276	
18	7.188	7.741	0.553	0.306	
20	7.174	7.748	0.574	0.329	

Mean value of $D_{n+10}^2 - D_n^2 = 0.159 \text{ cm}^2$

Refractive index of liquid $\mu = (0.233 \times 10^{-4}) \div (0.159 \times 10^{-4})$

$= 1.465$

The readings of the microscope to find the refractive index of **kerosene** are Tabulated as follows

Order of the ring	Reading of the microscope		Diameter D (cm)	$D^2 (cm^2)$	$D_{n+10}^2 - D_n^2$
	Right(cm)	Left (cm)			
2	2.370	2.550	0.180	0.032	0.162
4	2.330	2.580	0.250	0.063	0.167
6	2.300	2.615	0.315	0.099	0.156
8	2.275	2.630	0.355	0.126	0.161
10	2.255	2.655	0.400	0.160	0.159
12	2.235	2.675	0.440	0.194	
14	2.220	2.700	0.480	0.230	
16	2.205	2.710	0.505	0.255	
18	2.190	2.726	0.536	0.287	
20	2.175	2.740	0.565	0.319	

Mean value of $D_{n+10}^2 - D_n^2 = 0.161$

Refractive index of liquid $\mu = (0.233 \times 10^{-4}) \div (0.161 \times 10^{-4})$

$$= 1.447$$

The readings of the microscope to find the refractive index of **honey** are Tabulated as follows

Order of the ring	Reading of the microscope		Diameter D (cm)	$D^2 (cm^2)$	$D_{n+10}^2 - D_n^2$
	Right(cm)	Left (cm)			
2	2.377	2.550	0.173	0.030	0.158
4	2.331	2.590	0.259	0.067	0.163
6	2.301	2.620	0.319	0.102	0.152
8	2.273	2.640	0.367	0.135	0.157
10	2.254	2.665	0.411	0.169	0.155
12	2.230	2.664	0.434	0.188	
14	2.215	2.695	0.480	0.230	
16	2.195	2.699	0.504	0.254	
18	2.180	2.720	0.540	0.292	
20	2.165	2.734	0.569	0.324	

Mean value of $D_{n+10}^2 - D_n^2 = 0.157 \text{ cm}^2$

Refractive index of liquid $\mu = (0.233 \times 10^{-4}) \div (0.157 \times 10^{-4})$

= 1.484

5. CONCLUSION

The primary goal of this research is to experimentally ascertain the refractive index of various liquids using the Newton's Ring technique. To conclude the refractive index of various liquids using Newton's rings, we would typically analyze the interference patterns formed when a plano convex is placed on a flat glass surface with a thin layer of liquid being tested in between. By measuring the diameter of the rings and applying the formula for the radius of curvature of the lens we can determine the refractive index of liquid. Repeat the process for different liquids to compare their refractive indices. This method provides a precise and accurate way to characterize the optical properties of different liquids.

We have used four kinds of liquids such as **water, oil, kerosene and honey**. These fluids are positioned between two glass plates. In every instance, we observed both dark and bright fringes, utilizing them to compute the refractive index. Additionally, any sources of error or uncertainties in the measurements should be discussed, along with potential improvements for future experiments

The refractive index of the liquids determined through experimentation aligns with the theoretical value.

Refractive index of the liquid	Experimental value	Theoretical value
Water	1.331	1.33
Oil	1.465	1.470
Kerosene	1.447	1.44
Honey	1.484	1.504

Therefore, it can be inferred that the refractive index of any liquid can be determined through Newton's Ring Experiment.

6. REFERENCES

1. Ghatak, Ajoy (1970) Optics
2. Subramaniam; Brijlal; M.N, Avadhanulu; (2006) Text Book of Optics 23rd edition
3. R, Murugesan (2003) Optics and spectroscopy
4. Airy, G.B. (1833). "VI.On the phænomena of Newton's rings when formed between two transparent substances of different refractive powers" Philosophical Magazine. Series 3.
5. Illueca, C.; Vazquez, C.; Hernandez, C.; Viqueira, V. (1998). "The use of Newton's rings for characterizing ophthalmic lenses". Ophthalmic and Physiological Optics.
6. Dobroiu, Adrian; Alexandrescu, Adrian; Apostol, Dan; Nascov,Victor; Damian, Victor S. (2000). "Improved method for processing Newton's rings fringe patterns"
7. Tolansky, S, (2009). "XIV. New contributions to interferometry. Part II— New interference phenomena with Newton's rings". The London, Edinburgh, and Dublin Philosophical Magazine and Journal of Science
8. Optics: Eugene Hecht, Addison-Wesley 2002
9. Fundamentals of Optics: Jenkins and White, MCH, 1976
- 10.Modern Classical Optics – Geometrical Physical and Quantum: Dr Khanna and HR Gulati, R Chand, 1984
- 11.Principle of Optics: Max Born and Emil Wolf, 1970
- 12.Introduction to Modern Optics: Grant R Fowles, 1989
- 13.Optics: Miles V. Klein and Thomas E.Furtak, 1991
- 14.Principle of Optics: BK Mathur, 1995
- 15.Introduction to Optics: Frank.L, Pedrotti, Leno M Pedrotti and Leno S Petrotti, 2007